

Origins of Gas Giant Compositions: The Role of Disk Location and Dynamics

A DISSERTATION PRESENTED
BY
ANA-MARIA A. PISO
TO
THE DEPARTMENT OF ASTRONOMY

IN PARTIAL FULFILLMENT OF THE REQUIREMENTS
FOR THE DEGREE OF
DOCTOR OF PHILOSOPHY
IN THE SUBJECT OF
ASTRONOMY AND ASTROPHYSICS

HARVARD UNIVERSITY
CAMBRIDGE, MASSACHUSETTS
MAY 2016

©2016 – ANA-MARIA A. PISO
ALL RIGHTS RESERVED.

Origins of Gas Giant Compositions: The Role of Disk Location and Dynamics

ABSTRACT

The composition of planets is determined by and tightly linked to the composition of the protoplanetary disk in which they form. In the first part of my thesis, I study giant planet formation through core accretion. I show how the minimum core mass required to form a giant planet during the lifetime of the protoplanetary disk depends on the location in the disk, the equation of state of the nebular gas and dust opacity. This minimum applies when planetesimal accretion does not substantially heat the core's atmosphere. The minimum core mass decreases with semimajor axis, and may be significantly lower than the typically quoted value of $10 M_{\oplus}$, thus challenging previous studies that core accretion cannot operate in the outer disk. In the second part, I explore how the composition and evolution of protoplanetary disks may affect the formation and chemical composition of giant planets. Volatile snowlines are highly important in the planet formation process. I thus show how the snowline locations of the main carbon, oxygen and nitrogen carriers, as well as the C/N/O ratios, are affected by disk dynamics and ice morphology. Compared to a static disk, disk dynamics and ice morphology combined may change the CO and N₂ snowline locations by a factor of 7. Moreover, the gas-phase N/O ratio is highly enhanced throughout most of the disk, meaning that wide-separation giants should have an excess of nitrogen in their atmospheres which may be used to trace their origins. The large range of possible CO and N₂ snowline locations, and hence of regions with highly enhanced N/O ratios, implies that snowline observations at various stages of planet formation are crucial in order to use C/N/O ratios as beacons for planet formation zones.

Contents

1	INTRODUCTION	1
1.1	Dynamics and Chemistry in Protoplanetary Disks	3
1.2	The Core Accretion Mechanism and Its Challenges	10
1.3	The Disk-Planet Connection	12
2	ON THE MINIMUM CORE MASS FOR GIANT PLANET FORMATION AT WIDE SEP- ARATIONS	13
2.1	Introduction	14
2.2	Atmospheric Accretion Model	16
2.3	Analytic Cooling Model	26
2.4	Quasi-Static Kelvin-Helmholtz Contraction	33
2.5	Results for Giant Planet Formation	40
2.6	Neglected Effects	48
2.7	Summary	51
3	MINIMUM CORE MASSES FOR GIANT PLANET FORMATION WITH REALISTIC EQUA- TIONS OF STATE AND OPACITIES	54
3.1	Introduction	55
3.2	Atmospheric Model Review	59
3.3	Adiabatic Gradient for the Tabulated Equation of State	63

3.4	Role of the Equation of State	68
3.5	Impact of Opacity on Atmosphere Evolution	75
3.6	Critical Core Mass	77
3.7	Effects of Planetesimal Accretion	81
3.8	Summary	87
4	C/O AND SNOWLINE LOCATIONS IN PROTOPLANETARY DISKS: THE EFFECT OF RADIAL DRIFT AND VISCOUS GAS ACCRETION	89
4.1	Introduction	90
4.2	Model Framework	93
4.3	Snowline Locations	102
4.4	C/O Ratio Estimates	108
4.5	Discussion	114
4.6	Summary	122
5	THE ROLE OF ICE COMPOSITIONS AND MORPHOLOGY FOR SNOWLINES AND THE C/N/O RATIOS IN ACTIVE DISKS	125
5.1	Introduction	126
5.2	Coupled Drift-Desorption Model	128
5.3	Results	132
5.4	Discussion	140
5.5	Summary	143
6	SUMMARY AND FUTURE DIRECTIONS	146
6.1	Minimum Core Masses for Giant Planet Formation	147

6.2	The Role of Disk Dynamics and Ice Morphology on Snowline Locations and the C/N/O Ratios	148
6.3	Future Directions	150
APPENDIX A DERIVATION OF THE GLOBAL ENERGY EQUATION		151
APPENDIX B ANALYTIC COOLING MODEL DETAILS		155
APPENDIX C EQUATION OF STATE TABLE EXTENSION		160
APPENDIX D ADIABATIC GRADIENT VARIATIONS		168
APPENDIX E GRAIN GROWTH OPACITY AND RADIATIVE WINDOWS		173
APPENDIX F STEADY-STATE ACTIVE DISK SOLUTION		177
APPENDIX G DESORPTION DISTANCE ANALYTIC SOLUTION		179
REFERENCES		181

Listing of figures

1.1	The standard picture of molecular cloud to protostar to protoplanetary disk to planet formation. Reprinted by permission from Karin Öberg.	4
1.2	ALMA detection of the CO snowline in TW Hya at 30 AU. Reprinted by permission from Karin Öberg.	6
1.3	The C/O ratio in gas (solid line) and dust (dashed line) as a function of semimajor axis in a static disk. The dotted line shows the stellar value of 0.54. Gas-phase C/O ratios of order unity can be achieved in the outer disk. Reprinted by permission from Karin Öberg.	7
1.4	Desorption rate as a function of temperature in a TPD experiment, for CO and N ₂ as pure ices (top panel), on a compact H ₂ O substrate (middle panel), and on porous H ₂ O substrate (bottom panel). The peaks in the desorption curves are at substantially higher temperatures for the water dominated ices. Reprinted by permission from Karin Öberg.	9
2.1	Radial profiles of atmospheric pressure, temperature and enclosed mass (core included) for a $5M_{\oplus}$ core at 60 AU. Solid, dotted, dashed and dot-dashed lines correspond to solutions with total mass (core and atmosphere) of $5.01M_{\oplus}$, $5.10M_{\oplus}$, $6.00M_{\oplus}$ and $8.99M_{\oplus}$, respectively (see text for significance of these masses). Circles and triangles mark the locations of the Bondi radii and of the radiative-convective boundaries, respectively. The radial profiles extend from the core to the Hill radius.	34

2.2	Evolution of the luminosity and elapsed time during atmospheric growth around a $5M_{\oplus}$ core at 60 AU. The luminosity is initially high, then decreases as the atmosphere grows in mass and the radiative zone becomes optically thicker. Due to the neglect of self-gravity, the analytic model (<i>dashed curve</i>) gives luminosities that are too low and evolution times that are too long.	36
2.3	The effect of dust abundance on atmospheric evolution. Reducing dust opacities by factors of 10 and 100 from standard Solar abundances gives higher luminosities and faster atmospheric growth. Plotted quantities are similar to Figure 2.2, but for a $5M_{\oplus}$ core at 10 AU.	37
2.4	Evolution of the atmospheric growth timescale with mass around a $5M_{\oplus}$ solid core located at 10, 30 or 60 AU, for standard Solar opacities. Growth is slowest for $M_{\text{atm}} \sim 1 - 3M_{\oplus}$, i.e. before the crossover mass at $M_{\text{atm}} = M_c$	38
2.5	Individual terms in the atmospheric cooling model of Equation (2.16), for a $5M_{\oplus}$ core at 10 AU. The dashed curve for accretion energy indicates a negative contribution. All quantities are evaluated at the RCB, except for L_{negl} , the extra luminosity that would have been generated in the radiative zone, but is neglected in our model. The neglected luminosity is a small correction to the model luminosity L for $M_{\text{atm}} \lesssim 3M_{\oplus}$. Since these low masses dominate growth times, our model is roughly accurate.	40
2.6	Time to grow an atmosphere of mass M_{atm} for cores with fixed masses between $5M_{\oplus}$ and $14M_{\oplus}$ (as labeled) at 10 AU in our fiducial disk. Circles mark the runaway growth time, t_{run} , which occurs at roughly the crossover mass, $M_{\text{atm}} = M_c$. Both the time to reach a fixed atmosphere mass and the runaway growth time are shorter for larger cores. For larger M_c , runaway growth commences at higher M_{atm}/M_c values.	41

2.7	Runaway growth time, t_{run} , vs. core mass at 10 AU, for two values of the mean molecular weight. Our numerical model (<i>solid curves</i>) is compared to our non-self-gravitating analytic model (<i>dashed curves</i> , from Equation 2.37a). A typical protoplanetary disk life time of 3 Myr is plotted for comparison. The runaway growth time is larger for a lower mean molecular weight.	43
2.8	Runaway growth time as a function of disk temperature (<i>left</i>) and pressure (<i>right</i>) around a $M_c = 5M_{\oplus}$ core. The disk pressure or temperature (<i>left</i> or <i>right</i> , respectively) are fixed at values for 10 AU in our disk model. The analytic scalings given by Equation (2.37a) are plotted for comparison, as described in the text. Gas accretion slows down significantly at higher temperatures, but only speeds up modestly as the disk pressure or density increase.	44
2.9	The critical core mass as a function of semimajor axis, for a disk lifetime of 3 Myrs and two values of the mean molecular weight ($\mu = 2.35$ is for Solar abundances). The decline in M_{crit} with distance is a robust result for standard disk models. The analytic model, which neglects self-gravity, over-predicts the steepness of the decline.	45
2.10	Critical core masses vs. distance for standard and reduced (by a factor of ten) dust opacities. Lower opacities give significantly lower M_{crit} values. Atmospheric opacity remains a large uncertainty in core accretion models.	46

3.1	Contour plot of the adiabatic gradient ∇_{ad} for a hydrogen-helium mixture in thermodynamic equilibrium as a function of gas temperature and pressure. The upper-right rectangle encloses the region described by the original Saumon et al. (1995) EOS tables, while the rest of the plot is our extension. The black curves represent constant entropy adiabats, with the labels $\log_{10}(S)$ [$\text{erg K}^{-1} \text{g}^{-1}$]. The regions in which the EOS is either invalid or not computed are masked in white. Further details about the masked regions can be found in Appendix C.o.5.	64
3.2	Elapsed time to grow a planet of total mass (core + atmosphere) for a variety of EOS combinations (see text), for a planet forming at 5 AU and with a fixed core mass $M_c = 10M_{\oplus}$. Both hydrogen dissociation at high temperatures deep in the atmosphere and fractional occupation of H_2 rotational states at low temperatures in the outer envelope result in slower gas accretion when compared to an ideal gas polytrope.	70
3.3	We explore atmosphere growth around a core of $M_c = 10M_{\oplus}$ forming at 5 AU in our fiducial disk, for the EOS choices in Figure 3.2. Left panels show radial profiles of pressure (upper), $-e\rho r^3$ (middle) and temperature (lower), for a total mass (core + atmosphere) of $12M_{\oplus}$. Right panels display evolution with total mass of L (upper), $-dE/dM$ (middle) and \dot{M} (lower). Upper-left and upper-right: The variable occupation of H_2 rotational states in the outer atmosphere results in a deeper RCB and a lower luminosity for the realistic EOS. Middle-left and middle-right: the (negative) total energy of the atmosphere is more concentrated at the bottom of the envelope when compared to an ideal gas polytrope due to H_2 dissociation. This increases the amount of energy per unit mass, $-dE/dM$, that needs to be radiated away to accrete the next parcel of gas. Lower-left: H_2 dissociation in the inner atmosphere decreases the temperature near the core. Lower-right: Dissociation and fractional occupation of rotational states reduce \dot{M} and thus slow down atmospheric growth.	71

- 3.4 As an illustrative numerical experiment, we explore atmosphere growth around a core with $M_c = 10M_\oplus$ forming at 5 AU, and with total mass (core + atmosphere) $\leq 12 M_\oplus$, for the EOS choice of Equation (3.9) and various $\nabla_{\text{ad},1}$ and $\nabla_{\text{ad},2}$. In each panel, the circles mark the RCB location. The horizontal dash-dotted lines show the temperature $T_{\text{switch}} = 500$ K at which the adiabatic gradient changes. We show radial profiles of temperature (upper panels) and pressure (lower panels). Upper-left: fixed $\nabla_{\text{ad},1}$, varying $\nabla_{\text{ad},2}$. A larger $\nabla_{\text{ad},2}$ yields a deeper radiative region. Upper-right: varying $\nabla_{\text{ad},1}$, fixed $\nabla_{\text{ad},2}$. A lower $\nabla_{\text{ad},1}$ yields a more shallow radiative region. In both upper panels, the analytic profile of Equation (3.10) is over-plotted for comparison (*dotted line*) in regions of agreement. Lower-left: fixed $\nabla_{\text{ad},1}$, varying $\nabla_{\text{ad},2}$. Lower-right: varying $\nabla_{\text{ad},1}$, fixed $\nabla_{\text{ad},2}$. In both lower panels, the dashed black line is the analytic prediction for the pressure profile in the radiative zone, which agrees with the numerical results. 74
- 3.5 Elapsed time as a function of atmosphere mass, for cores with fixed masses between $15M_\oplus$ and $25M_\oplus$ at $a = 10$ AU in our fiducial disk, for a realistic EOS with an equilibrium ortho-to-para ratio and standard ISM opacity. The circles mark the runaway growth time. The numbers label the core mass in Earth masses. A larger core mass results in a lower t_{run} 77

- 3.6 Top panel: The minimum core mass for an atmosphere to initiate runaway gas accretion within the lifetime of a typical protoplanetary disk $t \sim 3$ Myrs as a function of semimajor axis, for a realistic hydrogen-helium mixture and a standard ISM opacity. The results of Paper I for an ideal diatomic gas are plotted for comparison. The realistic EOS yields core masses larger by a factor of ~ 2 when compared to the polytrope, for an equilibrium ortho-to-para ratio. The critical core mass is ~ 2 – 4 times larger than the polytrope case for a fixed 3:1 ratio between the H_2 spin isomers. The increase is more pronounced at larger stellocentric distances. Bottom panel: Critical core mass as a function of semimajor axis for a disk gas surface density 10 times larger than that of our fiducial disk. A larger Σ_d reduces M_{crit} by $\sim 15 - 25\%$ 79
- 3.7 Critical core mass as a function of semimajor axis for a realistic EOS with an equilibrium ortho-to-para ratio and radiative opacities that account for grain growth (purple triangles, with $p = 3.5$ and $a_{\text{max}} = 1$ cm; see text for details). The critical core mass is lower than it would be if dust grains had an ISM-like size distribution (blue circles). 80
- 3.8 Runaway accretion times for a realistic EOS with an equilibrium ortho-to-para ratio and different grain size distributions, for an atmosphere forming around a core with $M_c = 4M_{\oplus}$. The lines marked by purple and orange triangles have grain growth opacities with $a_{\text{max}} = 1$ cm, and $p = 3.5$ and $p = 2.5$, respectively (see text for details). The blue circle line has an ISM power-law opacity. The runaway accretion time is more than one order of magnitude lower when coagulation is accounted for, i.e. $p = 2.5$ 81

- 3.9 Various accretion rates for a planet forming at 30 AU and with a core mass $M_c = 10M_\oplus$, using a polytropic EOS and ISM power-law opacity. For this choice of parameters, the runaway accretion time is $t_{\text{run}} \sim 1.4$ Myrs. The \dot{M}_{atm} (solid blue) curve represents the growth rate of the atmosphere as estimated by our model. The core accretion rate $\dot{M}_{c,\text{acc}}$ (dashed green) necessary to grow the core on the timescale t_{run} is larger than $\dot{M}_{c,\text{KH}}$ (dotted red), the maximum planetesimal accretion rate during KH contraction for which our regime is valid (see text). The frequently used planetesimal accretion rate $\dot{M}_{c,\text{Hill}}$ (dashed-dotted light blue) for which the random velocity of the planetesimals is given by the Hill velocity due to the core (see text), also exceeds $\dot{M}_{c,\text{KH}}$. This motivates our requirement that planetesimal accretion must have slowed down after core growth for our model to be valid. 84
- 3.10 Comparison between the critical core mass $M_{\text{crit,KH}}$ given significant planetesimal accretion and the critical core mass when gas contraction dominates, for a polytropic EOS and an ISM opacity reduced by a factor of 100. Our results yield lower core masses than in the fast planetesimal accretion case (e.g., Rafikov 2006). The critical core mass corresponding to $\dot{M}_{c,\text{Hill}}$ and $\dot{M}_{c,\text{acc}}$ from Figure 3.9 is plotted for comparison. 86

- 4.1 Relevant timescales for dynamical effects in the desorption process: t_{drift} (solid lines), t_{des} (dashed lines) and $t_{\text{gas,acc}}$ (dotted lines). The timescales are calculated at three representative locations, i.e. the H₂O, CO₂ and CO snowlines in the static disk. For our choice of parameters, the snowlines are located at ~ 0.7 AU (blue lines), ~ 8.6 AU (green lines) and ~ 59 AU (red lines), respectively. The horizontal dot-dashed line represents a typical disk lifetime of 3 Myr. The particle size ordering at the minimum t_{drift} is not monotonic in snowline distance due to different drag regimes for those particle sizes at the snowline locations (Epstein drag at the H₂O and CO₂ snowlines, and Stokes drag at the CO snowline). Similarly, the ordering of t_{des} is not monotonic in snowline distance due to the non-monotony in mean molecular weight between H₂O, CO₂ and CO ($18 m_p$, $44 m_p$ and $28 m_p$, respectively). Radial drift and gas accretion affect desorption in the regions where their respective timescales, i.e. t_{drift} and $t_{\text{gas,acc}}$, are comparable to the desorption timescale t_{des} 101
- 4.2 Desorption distance (if a grain fully desorbs; horizontal lines) or final distance (if a grain does not fully desorb; diagonal lines for particles that do not drift and non-horizontal, non-diagonal lines for particles that drift), as a function of a particle's initial location in the disk, for a range of particle sizes, and for both an irradiated disk (left panels) and an evolving disk (right panels). The desorption distance is calculated for particles composed of H₂O (top panels), CO₂ (middle panels) and CO (bottom panels). The desorption distance for a static disk is shown for comparison (dashed vertical and horizontal lines). The particle size increases from 10^{-3} cm to 10^8 cm as indicated by the color bar. For a particle of a given initial size that entirely desorbs during $t_d = 3$ Myr, the desorption distance is the same regardless of the particle's initial location. 105

- 4.3 Desorption distance estimated from analytic calculations (see text) as a function of the desorption distance calculated numerically, for the range of particle sizes that desorb at a fixed distance regardless of their initial location (see Figure 4.2 and text). The estimate is performed for an irradiated disk (left panels) and an evolving disk (right panels). The particles are composed of H_2O (top panels), CO_2 (middle panels) and CO (bottom panels). The analytic approximation is in good agreement with the numerical result for most cases, with the exception of larger particles, $s \gtrsim 10$ cm (see text). 106
- 4.4 Left panels: size of desorbing H_2O particles as a function of time, for different initial particle sizes and for three initial locations in an irradiated disk: 1 AU (top left), 10 AU (middle left) and 100 AU (bottom left). Particles desorb almost instantaneously. Right panel: fractional mass of the desorbing particles as a function of the particle's location as it drifts, for different initial particle sizes, and at the same initial locations presented in the left panel. Particles lose most of their mass very close to the distance at which they fully desorb. The static H_2O snowline is shown for reference (dashed vertical lines). 107
- 4.5 Estimated C/O ratio in gas (solid lines) and in dust (dashed lines) for an irradiated disk (top panel), an evolving disk (middle panel) and a viscous disk (bottom panel). The particle size increases from ~ 0.05 cm to ~ 700 cm as indicated by the color bar. The horizontal dotted line represents the stellar value of 0.54. The black lines represent the C/O ratio in gas (solid black line) and dust (dashed black line) for a static disk, with the temperature profile given by Equation (4.1b) for the top two panels and by Equation (4.8) for the bottom panel. For both the evolving and the viscous disk, the movement of desorbed CO_2 gas inside the CO_2 snowline, and of desorbed CO_2 and H_2O gas inside the H_2O snowline due to gas accretion will increase the amount of oxygen gas inside the respective snowlines and thus reduce the gas C/O ratio, as shown by the arrows. . . . 109

- 4.6 Desorption or final distance as a function of initial position in the disk for particles of initial size $s_0 = 1$ m (left panels) and $s_0 = 10$ cm (right panels), for grains composed of H_2O (top panels), CO_2 (middle panels) and CO (bottom panels). The evolution is shown at four representative timescales: 10^4 yr (cyan curve), 10^5 yr (purple curve), 1 Myr (blue curve), and 3 Myr, the disk lifetime (orange curve). For a given particle size, the desorption distance, and hence the H_2O , CO_2 and CO snowlines, have the same location regardless of the time at which the simulation is stopped. 115
- 4.7 Desorption or final distance as a function of initial position in the disk for H_2O particles of initial size of 1 m, for total disk masses $M = 0.1M_\odot$ (solid lines) and $M = 0.01M_\odot$ (dashed lines). The timescales at which we stop the simulations are 10^4 yr (cyan curve), 10^5 yr (red curve), 1 Myr (green curve) and 3 Myr (blue curve). A lower disk mass does not change the snowline location. 116
- 4.8 Desorption or final distance as a function of initial position in the disk for H_2O particles of initial size of 1 m, for our fiducial disk (solid lines) and for a transition disk with an inner cavity at $r_0 = 4$ AU (dashed lines). The timescales of the simulations and their color code are the same as in Figure 4.7. Particles that start inside the cavity drift towards the original snowline, while particles that start outside the gap stop shortly after crossing the gap edge, due to being trapped in a pressure maximum. 117
- 5.1 The total carbon, nitrogen and oxygen abundance in solids as a function of semimajor axis in a static disk, for CO and N_2 as pure ices (top panel) and water dominated ices (bottom panel). Relevant volatile snowlines are marked by the vertical dashed lines. The grain abundances are calculated as a function of the observed median CH_4 and NH_3 abundances in protostellar cores. The total grain abundance increases with semimajor axis as more and more species freeze out. 133

5.2	The C/O ratio in gas (solid lines) and dust (dashed lines) as a function of semimajor axis in a static disk, assuming no carbon is present in the form of CH ₄ (top panel), the median observed CH ₄ abundance is assumed (middle panel), and the maximum observed CH ₄ abundance is assumed (bottom panel). The C/O estimates are performed assuming that the CO ices are in pure form. The vertical dotted lines mark the snowline locations of the main C and O carriers. The horizontal dotted lines represent the stellar C/O value. The presence of methane only modestly increases the C/O ratio in gas between the CO ₂ and CH ₄ snowlines.	135
5.3	The N/O ratio in gas (solid lines) and dust (dashed lines) as a function of semimajor axis in a static disk, assuming no nitrogen is present in the form of NH ₃ (top panel), the median observed NH ₃ abundance is assumed (middle panel), and the maximum observed NH ₃ abundance is assumed (bottom panel). The N/O estimates are performed assuming that the CO and N ₂ ices are in pure form. The vertical dotted lines mark the snowline locations of the main C,O and N carriers. The horizontal dotted lines represent the average N/O value in the disk. The gas-phase N/O ratio is enhanced by a factor of two between the H ₂ O and CO ₂ snowlines compared to its average value, and by a factor of three between the CO ₂ and CO snowlines. The arrows mark a highly elevated N/O ratio in gas between the CO and N ₂ snowlines due to the depletion of oxygen gas in this region. The presence of NH ₃ moderately decreases the N/O ratio in gas between the NH ₃ and CO ₂ snowlines.	137

5.4 C/O ratio estimates in gas (solid lines) and dust (dashed lines) as function of semimajor axis in a viscous disk, for CO as pure ice (top panel) or as water dominated ices (bottom panel). The H₂O, CO₂ and CO snowlines are shown for particles with initial sizes $\sim 0.05 \text{ cm} \lesssim s \lesssim 7 \text{ m}$ as indicated by the color bar. The C/O ratio in a static disk (black lines) is shown for comparison. The arrows show that the C/O ratio in gas will decrease inside the H₂O and CO₂ snowlines in the viscous disk, as the relative fluxes of the desorbed icy particles and the overall nebular gas will cause an excess of oxygen gas inside these snowlines (see Paper I for details). The presence of CO in a water ice environment rather than as pure ice moves the CO snowline significantly inward by $\sim 70\%$. Taken together, disk dynamics and ice morphology move the CO snowline inward by a factor of ~ 7 138

5.5	N/O ratio estimates in gas (solid lines) and dust (dashed lines) as function of semimajor axis in a viscous disk, for CO and N ₂ as pure ices (top panel) or as water dominated ices (bottom panel). The H ₂ O, CO ₂ , CO and N ₂ snowlines are shown for particles with initial sizes $\sim 0.05 \text{ cm} \lesssim s \lesssim 7 \text{ m}$ as indicated by the color bar. The N/O ratio in a static disk (black lines) is shown for comparison. The arrows show that the N/O ratio in gas will decrease inside the H ₂ O and CO ₂ snowlines in the viscous disk, as the relative fluxes of the desorbed icy particles and the overall nebular gas will cause an excess of oxygen gas inside these snowlines (see Paper I for details). Radial drift and gas accretion move the N ₂ snowline inward by up to $\sim 50\%$ compared to a static disk. The presence of N ₂ in a water ice environment rather than as pure ice moves the N ₂ snowline significantly inward by $\sim 70\%$. Taken together, disk dynamics and ice morphology move the N ₂ snowline inward by a factor of ~ 7 . The results of an enhanced gas-phase N/O ratio between the H ₂ O and CO snowlines compared to its average value, and of highly elevated N/O ratios in gas between the CO and N ₂ snowlines (see Figure 5.3), are preserved.	140
5.6	Gas phase C/O (blue curve) and N/O (red curve) ratios divided by the average C/O and N/O ratio in a static disk, assuming CO and N ₂ are pure ices, and there is no CH ₄ or NH ₃ . The dashed vertical lines mark the H ₂ O, CO ₂ , CO and N ₂ snowlines. The arrow indicates that the N/O ratio is enhanced by orders of magnitude compared to its average value between the CO and N ₂ snowlines. The gaseous N/O ratio is enhanced throughout most of the disk, and more enhanced than the C/O ratio.	141

- C.1 Contour plot of the hydrogen adiabatic gradient ∇_{ad} as a function of gas temperature and pressure. The upper right rectangle encloses the region described by the original Saumon et al. (1995) EOS tables, while the rest of the plot is our extension to lower temperatures and pressures for an equilibrium mixture of ortho- and parahydrogen. The black curves represent constant entropy adiabats with labels $\log_{10}(S)$, where S [erg K⁻¹ g⁻¹] is the absolute entropy per unit mass. At high temperatures, hydrogen dissociates and ionizes, while at low temperatures the rotational states of the hydrogen molecule are only partially excited and it no longer behaves like an ideal diatomic gas. Regions in which the EOS is invalid or has not been computed are masked in white (see text). 166
- C.2 Same as Figure C.1 but for pure helium. Helium ionizes at $T \gtrsim 10,000$ K, but behaves as an ideal monatomic gas otherwise. We choose $T = 7,000$ K as a conservative temperature cutoff above which our extension is no longer valid (masked in white). The EOS has not been computed in the lower-right region of the plot (see text). 167
- D.1 Adiabatic gradient as a function of the hydrogen dissociation fraction x . The adiabatic gradient is $\nabla_{\text{ad}} = 2/7$ for pure molecular hydrogen ($x = 0$) and $\nabla_{\text{ad}} = 2/5$ for fully atomic hydrogen ($x = 1$), and drops to low values during partial dissociation. . 170
- D.2 Internal energy per unit mass and specific heat capacity associated with rotation for parahydrogen (dashed blue), orthohydrogen (dotted green), the equilibrium mixture (solid red) and a fixed 3:1 ortho-to-para ratio (dash-dotted light blue) as a function of temperature. After Farkas (1935), Figure 1. 171

D.3	Evolution of the luminosity and elapsed time during atmospheric growth around a $8M_{\oplus}$ core at 100 AU, for a realistic EOS with hydrogen spin isomers in thermal equilibrium (solid line), and with a fixed ortho-to-para ratio 3:1 (dashed line). The assumption of a fixed ortho-to-para ratio increases the runaway accretion time t_{run} by a factor of ~ 3 compared to the equilibrium mixture.	172
E.1	Rosseland mean opacity of dust grains as a function of temperature for different opacity assumptions. The dashed black curve shows the Bell & Lin (1994) analytic ISM opacity for $\rho = 10^{-8} \text{ g cm}^{-3}$. The solid black curve shows the tabulated opacity of Semenov et al. (2003) for a dust composition of 'normal' silicates. The dashed red curve shows the D'Alessio et al. (2001) opacity, which takes grain growth into account, for a maximum particle size of 1 μm and a standard collisional cascade grain size distribution ($p = 3.5$). The solid red curve is the same as the dashed red curve, but it accounts for coagulation ($p = 2.5$).	174
E.2	Snapshots of the radiative and adiabatic gradient as a function of the radial coordinate, for planets with different core masses forming at various locations in the disk. The nebular gas is described by a realistic EOS, with a standard collisional cascade size distribution ($p = 3.5$). The sharp drop in opacity due to dust sublimation may generate one or more radiative windows. Top panel: no radiative window for $a = 100 \text{ AU}$ and $M_c = 3M_{\oplus}$. Middle panel: the sharp opacity decrease produces one radiative window for $a = 50 \text{ AU}$ and $M_c = 5M_{\oplus}$. Bottom panel: the decrease in opacity results in two radiative windows for $a = 20 \text{ AU}$ and $M_c = 3M_{\oplus}$	175

THIS IS THE DEDICATION.

Acknowledgments

LOREM IPSUM DOLOR SIT AMET, consectetur adipiscing elit. Morbi commodo, ipsum sed pharetra gravida, orci magna rhoncus neque, id pulvinar odio lorem non turpis. Nullam sit amet enim. Suspendisse id velit vitae ligula volutpat condimentum. Aliquam erat volutpat. Sed quis velit. Nulla facilisi. Nulla libero. Vivamus pharetra posuere sapien. Nam consectetur. Sed aliquam, nunc eget euismod ullamcorper, lectus nunc ullamcorper orci, fermentum bibendum enim nibh eget ipsum. Donec porttitor ligula eu dolor. Maecenas vitae nulla consequat libero cursus venenatis. Nam magna enim, accumsan eu, blandit sed, blandit a, eros.

1

Introduction

In recent years, the field of giant planet formation has aimed to answer two fundamental questions:

1. Where in the protoplanetary disk can gas giants form?
2. What compositions will the formed giant planets have obtained?

We can start uncovering the answers to these questions through a combination of studying planet formation in protoplanetary disks, the end-results of planet formation (i.e., exoplanets), and through comparisons with the architecture and composition of our own Solar System. Within the last two decades, more than one thousand extrasolar planets (exoplanets) have been discovered [Batalha \(2014\)](#). Their diversity in terms of mass, radius, location and composition [Lissauer et al. \(2014\)](#) provides an exciting field of research, with the eventual goal of finding planets that are similar

to our own Earth and may sustain life. For this purpose, it is thus crucial to explore and understand how planets obtain their compositions. Observations of Earth-like planets that can provide useful insight about their composition are challenging — the solid interior structure of terrestrial planets cannot be detected, and their gaseous envelopes are small by comparison (both in mass and radius), which makes it difficult to obtain atmospheric spectra and find out what chemical compounds they are made of. We therefore turn to giant planets, which have provided a rich and intriguing research area for decades. Gas giants contain most of their mass in their atmosphere, hence their chemical composition is determined by that of their envelopes. The last few years have seen a substantial increase in the number of giant planets with observed atmospheric spectra (e.g., [Debes et al. 2013](#), [Kreidberg et al. 2015](#)), which has enhanced our understanding of these planets' chemical structure, and has provided us with quantitative information about the abundances of various compounds in their envelopes besides hydrogen and helium. Finally, gas giants shape the architecture of planetary systems and affect the delivery of volatile compounds to terrestrial planets, which has direct consequences for the habitability of worlds similar to our own. Thus testing theories of planet formation against gas giant compositions will help constrain planet formation theories more generally.

Both terrestrial and giant planets are born in protoplanetary disks, which implies that their compositions are determined by and tightly linked to the structure and composition of the disk. The chemical and dynamical evolution of disks, as well the formation of giant planets have both been previously investigated in isolation. However, the coupled chemo-dynamical disk evolution, planet compositions, and most importantly the disk-planet connection have not yet been considered in detail. In this thesis, we uncover some of the answers to this issue from two standpoints: (1) by looking at the role of disk location in setting the conditions for the formation of wide-separation gas giants, and (2) by investigating how the structure and chemical composition of the protoplanetary disk at different radii affects the composition of nascent giant planets.

1.1 DYNAMICS AND CHEMISTRY IN PROTOPLANETARY DISKS

Protoplanetary disks are the result of the collapse of a molecular cloud, and are structures composed of gas and dust that are rotationally supported and that represent the birth environment of planets (Figure 1.1). Disks are complex objects, whose structure and evolution are affected by a multitude of chemical and dynamical processes. The latter include transport of both dust through radial drift and gas through viscous gas accretion, as well as grain growth and dust settling to the disk midplane, which affect the disk structure. In terms of chemistry, the strongly irradiated disk surface is dominated by photochemical reactions, while the ionized lower layers have a rich ion-molecule chemistry. Finally, the cold disk midplane is mostly shielded from irradiation, and volatile compounds experience freeze-out. Many of these processes are summarized in [Henning & Semenov \(2013\)](#), and several of them are not yet fully understood. Moreover, the timescales for various disk chemical and dynamical processes may be comparable at least in some parts of the disk ([Semenov & Wiebe 2011](#)), which makes the coupling between chemistry and dynamics very challenging. As a first step it is thus easier to isolate the different dynamical and chemical processes that occur in the disk midplane where planets are born, and understand their role and relative importance in shaping disk and planet compositions. We explore some of these processes in Chapters 4 and 5, and investigate their consequences for the compositions of giant planets forming at different radii.

1.1.1 DISK TEMPERATURE AND DENSITY STRUCTURE

The midplane temperature in a protoplanetary disk is set both by the irradiation from the host star and by accretion heating (e.g., [Armitage 2010](#)). Accretion heating dominates in the inner disk (typically within a few AU) where the accretion flows are strongest, while the outer disk is dominated by stellar irradiation. While the irradiation component of the temperature simply follows a power-law in radius, the accretional component is determined by viscosity and the gas mass accretion rate,

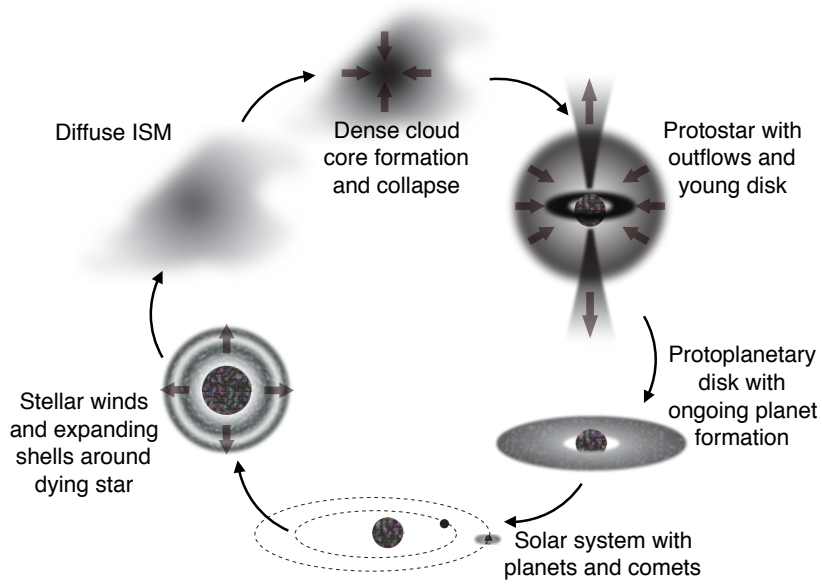


Figure 1.1: The standard picture of molecular cloud to protostar to protoplanetary disk to planet formation. Reprinted by permission from Karin Öberg.

which in turn depend on the temperature itself, as well as the gas surface density (for a more complete review see [Shakura & Sunyaev 1973](#)). As the gas surface density changes with time in an active disk, it follows that determining the midplane temperature in an active disk in which both stellar irradiation and accretion heating contribute to the thermal evolution of the disk is non-trivial. We simplify this problem in Chapters 4 and 5 by assuming a steady-state disk with a constant mass accretion flow, and by solving the thin disk Shakura-Sunyaev equations.

The gas surface density in a viscous disk follows the continuity equation, and is set by both the disk temperature and viscosity. Infall of material onto the disk or outflow may also contribute to the gas surface density evolution ([Birnstiel et al. 2010](#)). The dust surface density can be described by an advection-diffusion equation (e.g., [Birnstiel et al. 2012](#)), where both the radial movement of the dust and diffusion contribute to its evolution. The diffusion term is due to the fact that the dust is turbulently mixed by the gas, which causes a change in the dust-to-gas ratio and thus a radial gradient in

the ratio between solid and gas surface densities. In the case of small particles that are well coupled to the gas, the surface density follows that of the gas and a constant dust-to-gas ratio is maintained. The movement of larger particles, however, is affected both by radial drift, gas drag and diffusion, which cause the dust surface density to "decouple" from that of the gas. This results in depletion of solids in some disk regions and a pile-up in others, depending on a particle's radial drift velocity and the level of turbulent mixing. The dust surface density is further affected by grain growth and fragmentation. We do not address all these effects in Chapter 4 and 5, and instead assume a constant inflow of particles such that the dust surface density remains spatially and temporally constant. We note, however, that these effects have to be taken into account for a more realistic modeling of the dust surface density, and thus of the surface density evolution of volatiles, both in solid and gaseous form.

1.1.2 SNOWLINES AND DISK DYNAMICS

Volatile compounds, which have low sublimation temperatures, are of particular importance. Their relative abundance in gaseous and solid form determines their snowline location, i.e. the distance in the disk where a volatile transitions from gaseous to solid form. Snowlines are essential in the planet formation process (e.g., [Pontoppidan et al. 2014](#)): they can enhance the amount of solid material just outside the snowline, due to dust sublimation, and they can produce pressure traps where dust particles pile up just inside the snowline. Observational advancements in recent year have provided us with an increasing amount of information regarding volatiles in disks. Volatile compounds have been detected in disks (e.g., [Henning & Semenov 2013](#)), which gives us clues about their abundance in different disks and at different disk locations. Moreover, with the advent of ALMA volatile snowlines have also been observed. This is essential as it provides us with knowledge regarding volatile abundances in gas and dust throughout the disk, and thus the compositions of giant planets. Figure 1.2 shows the detection of the CO snowline in TW Hya at 30 AU ([Qi et al. 2013](#)). This snowline has

been detected indirectly through its tracer molecule N_2H^+ , which becomes highly abundant as CO freezes out. Moreover, the H_2O snowline has also been detected in Tw Hya (Zhang et al. 2013), as well as the CO snowline in HD 163296 (Qi et al. 2015).

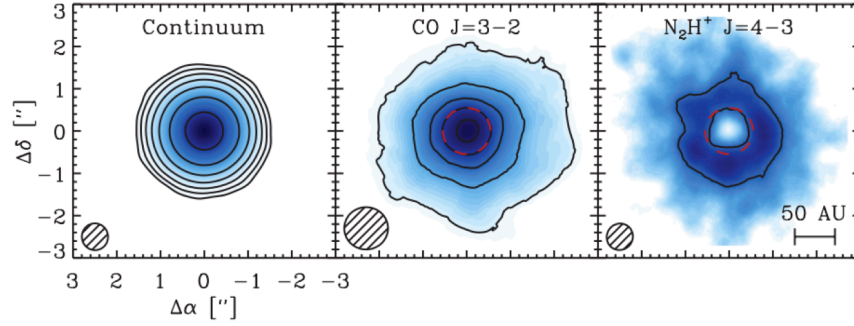


Figure 1.2: ALMA detection of the CO snowline in TW Hya at 30 AU. Reprinted by permission from Karin Öberg.

One important effect of the existence of snowlines is that disks are expected to contain different amounts of volatiles in gas and in dust at different locations. As the main carbon and oxygen carriers, i.e. H_2O , CO_2 and CO , are amongst the most abundant volatiles in comets and protostellar cores (Rodgers & Charnley 2002, Mumma & Charnley 2011, Henning & Semenov 2013), variations in the carbon-to-oxygen (C/O) ratio in gas and dust throughout a disk are particularly important. This issue was first addressed by Öberg et al. (2011b). Figure 1.3 shows the C/O ratio in gas and dust as a function of semimajor axis, assuming protostellar abundances for the volatiles. The C/O ratio in gas is enhanced compared to the stellar value, particularly between the CO_2 and CO snowlines where it reaches unity. The pioneering work of Öberg et al. (2011b) inspired Chapter 4 of this thesis. Öberg et al. (2011b) consider a static disk, and thus do not account for dynamical processes such as redistribution of solids due to radial drift, the radial movement of the nebular gas, and accretion heating. We thus expand this model by considering the processes outlined above and their effect on snowline locations. In particular, we focus on how radial drift of solids and viscous gas accretion onto the central star affect the H_2O , CO_2 and CO snowline locations for particles of different

sizes. We find that drift and accretion heating alone may move the snowlines inward by factors of ~ 2 compared to a static disk, thus substantially changing the disk regions with enhanced gas-phase C/O ratios.

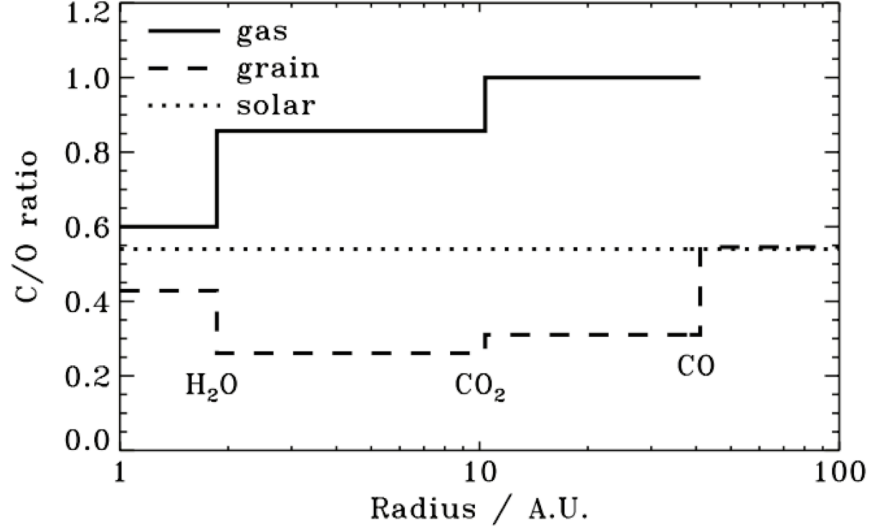


Figure 1.3: The C/O ratio in gas (solid line) and dust (dashed line) as a function of semimajor axis in a static disk. The dotted line shows the stellar value of 0.54. Gas-phase C/O ratios of order unity can be achieved in the outer disk. Reprinted by permission from Karin Öberg.

As we show above, the C/O ratio is highly important to study, but it only provides us with one piece of the puzzle that is constraining planet formation origins based on their compositions. In order to improve our theoretical models, we thus need to look at other molecules and volatile compounds. The first that comes to mind is nitrogen, as it is highly abundant in the Solar System (Lodders 2003), and primarily believed to exist as N_2 (e.g., Owen et al. 2001). Molecular nitrogen cannot be detected directly. However, an inventory of nitrogen cometary abundances shows that NH_3 is the most abundant observed nitrogen carrier, and yet its concentration is only a small fraction of the total nitrogen abundance, which leaves N_2 as the main nitrogen bearing species. In the context of planet compositions, N_2 is important due to its high volatility. The gas phase nitrogen-to-oxygen (N/O) ratio in the outer disk may thus be even more enhanced than the C/O ratio. We calculate the

N/O ratio in gas and dust in Chapter 5, and confirm that it is indeed highly enhanced compared to the stellar value throughout most of the disk.

1.1.3 ICE MORPHOLOGY

The snowline locations of volatiles, including carbon, oxygen and nitrogen carriers, are highly dependent on the morphology of the icy particles. These can either form on a dust mantle as pure ices, or have a layered structure with the more volatile species closer to the outer layers (e.g., [Pontoppidan et al. 2003](#)). As H_2O is the least volatile species with high abundance in disks, one can typically expect the more volatile molecules to form on a water substrate (but see [Bisschop et al. 2006](#) for other scenarios). The ice environment in which the molecules reside, i.e. pure or water dominated ices, will determine their binding energies. This, in turn, will change the temperatures at which the ices desorb, and thus their snowline locations. This effect is particularly important in the case of CO and N_2 , since their volatility is significantly higher than that of other carbon and nitrogen carriers, such as CO_2 or NH_3 . Laboratory experiments [Fayolle et al. \(2016\)](#) have determined new values for the CO and N_2 binding energies, both as pure ices and water dominated. Figure 1.4 shows the results of a temperature programmed desorption (TPD) experiment for the CO and N_2 desorption rate as a function of temperature, in water dominated and pure ice environments. The peak of the desorption curves shifts considerably between the different binding environments. This translates into a difference in binding energies by up to a factor of two between pure and water dominated CO or N_2 . We show in Chapter 5 that this large difference in binding energies changes the CO and N_2 snowline locations by factors of 3-4 depending on the ice environment. By taking into account also the effect of disk dynamics, we find that the CO and N_2 snowlines may span several tens of AU. This uncertainty in snowline locations suggests yet again that more observations are needed to constrain disk volatile compositions at different locations.

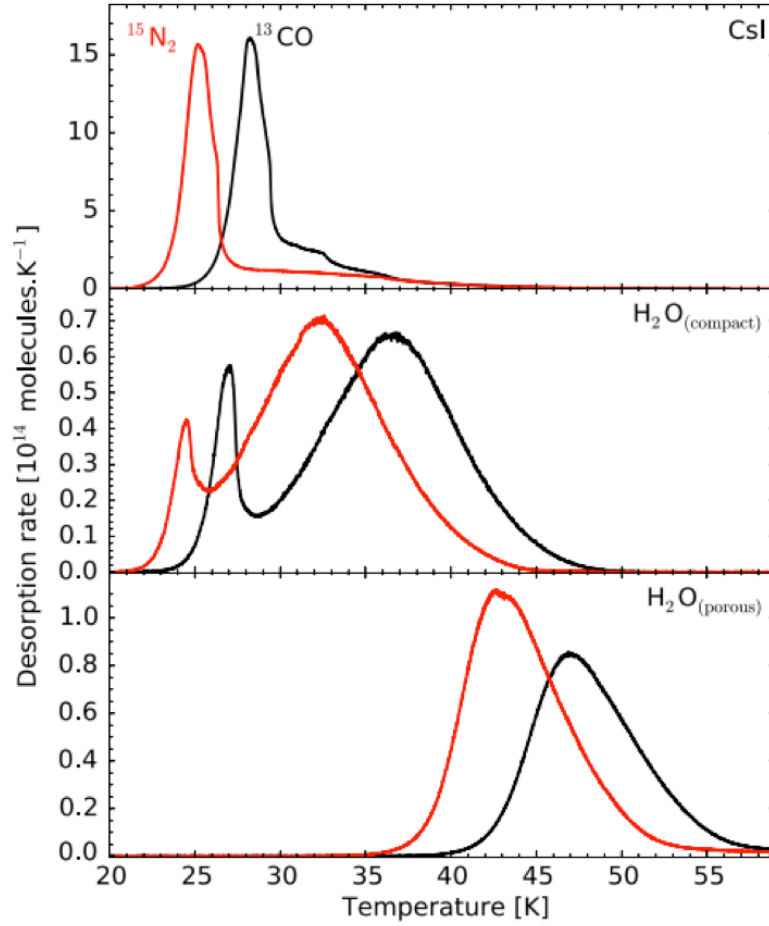


Figure 1.4: Desorption rate as a function of temperature in a TPD experiment, for CO and N₂ as pure ices (top panel), on a compact H₂O substrate (middle panel), and on porous H₂O substrate (bottom panel). The peaks in the desorption curves are at substantially higher temperatures for the water dominated ices. Reprinted by permission from Karin Öberg.

1.1.4 CONSEQUENCES FOR THE C/N/O RATIO IN PLANETARY ATMOSPHERES

Variations in the C/O ratio in gas and dust due to different volatile condensation temperatures have also been investigated in exoplanet atmospheres, both from a theoretical and observational standpoint. [Mollière et al. \(2015\)](#) show that varying the C/O ratio in a gas giant envelope by factors of ~ 3 changes the abundance of other volatiles, such as H₂O and CH₄, by several orders of magnitude.

From the observational perspective, an exciting potential discovery was that some planets, such as WASP-12 b, have a superstellar C/O ratio (Madhusudhan et al. 2011). While this particular detection has since been unequivocally refuted (e.g., Kreidberg et al. 2015), the advent of JWST in the near future will provide us with a significantly larger sample of atmospheric spectra which may be used to constrain C/O ratios in other giant planet atmospheres.

While observational constraints for the N/O ratio in planetary atmospheres do not currently exist, the high gas-phase N/O ratio enhancement at most disk radii suggests that giant planets that form at wide separations should have an excess of nitrogen in their atmospheres, which could be used to trace their formation origin. Theoretical and observational knowledge of both C/O and N/O ratios could further help back-track the planet formation location based on planet composition.

1.2 THE CORE ACCRETION MECHANISM AND ITS CHALLENGES

Gas giants are widely believed to form through core accretion (e.g., Pollack et al. 1996), a theory in which solid protoplanetary cores grow large enough to accumulate a massive atmosphere. In this model, planetesimals in a disk grow larger through collisions, eventually forming a planetary embryo, which continues to grow by attracting planetesimals in its neighborhood. Once an embryo becomes large enough so that its escape velocity exceeds the thermal velocity of the nebular gas in its vicinity, it starts accumulating a gaseous envelope. From this point on, the accretion of gas is regulated by the pressure support within the envelope — the amount of gas a core can accumulate is limited by the atmosphere’s ability to radiate away the energy due to the incoming planetesimals, as well as by envelope contraction.

Protoplanetary disks dissipate on relatively short timescales of a few Myr. This implies that cores must grow fast in order to become large enough to attract massive atmospheres, and thus they need high planetesimal accretion rates. Studies that consider such high and constant rates (e.g., Stevenson

1982, Bodenheimer & Pollack 1986, Wuchterl 1993, Rafikov 2006) find that the envelope accumulating around the planet is in steady state at all times, since all the energy due to the incoming planetesimals is radiated away by the atmosphere. It follows that the core and envelope grow simultaneously, and the mass of the atmosphere is a function of the core mass. Once the core and atmosphere have attained comparable masses, a rapid phase of runaway gas accretion starts and the gas giant can form. In this steady state scenario, there is therefore a uniquely determined core mass at which runaway accretion commences, called the critical core mass M_{crit} . High planetesimal accretion rates cause the core to grow quickly, but this poses an additional challenge: fast accretion heats up the core's atmosphere, increases pressure support and inhibits the ability of the envelope to cool and contract, thus eventually increasing M_{crit} . This is particularly challenging in the outer disk, where long dynamical times prevent large cores from forming before disk dissipation. Rafikov (2011) shows that core accretion cannot operate beyond 40-50 AU at the accretion rates required to form the core and the atmosphere on the same timescale.

All this seems to indicate that core accretion cannot work in the outer disk. This poses an intriguing question: could wide-separation gas giants, such as the HR 8799 system, have formed through core accretion? We can start answering this question by noting that planetesimal accretion does not need to be constant with time at a given location in the disk, which has been shown to be a viable scenario (e.g., Ikoma et al. 2000, Pollack et al. 1996). Figure 1 from Pollack et al. (1996) shows an example of this scenario. At early times, the core is in a high planetesimal accretion rate regime and grows fast, but the atmosphere remains small in comparison. As the planet depletes its feeding zone of solids, planetesimal accretion is reduced. From this point on, the core no longer grows significantly, and thus the energy due to planetesimals can no longer balance radiative losses by the atmosphere; now the envelope accumulates gas while undergoing Kelvin-Helmholtz contraction, until its mass approximately exceeds the core mass and runaway gas accretion begins. Since now the envelope grows with time, there is no longer a uniquely determined M_{crit} — in this scenario, the

critical core mass is that of a core than can accrete an atmosphere with a mass equal to its own on a timescale equal to the disk lifetime.

Such studies potentially provide a viable solution to the core accretion challenge at wide separations, but they are primarily focused on explaining the formation of Jupiter at 5.2 AU and thus do not explore a larger radii parameter space. Moreover, in order to truly understand whether core accretion can indeed work at stellocentric distances significantly larger than that of Jupiter, a more interesting question can be asked: what is the lowest possible core mass required to form a gas giant before disk dissipation? This minimum core mass is determined when planetesimal accretion has fully stopped, since additional accretion would actually increase this core mass (see above). Moreover, how does this minimum core mass depend on disk location, the properties of the nebular gas, and the opacity of the dust grains? We provide an answer to these questions in Chapters 2 and 3, where we find that the minimum core mass for giant planet formation is lower than the one typically quoted, $10 M_{\oplus}$ (Stevenson 1982, Rafikov 2006), and may be as low as $1 M_{\oplus}$. Our study thus reopens the case for in situ formation of wide-separation gas giants through core accretion.

1.3 THE DISK-PLANET CONNECTION

Our work in the two main parts of this thesis confirms that there is indeed a tight link between disks and planets. Our study on core accretion shows that the core mass required to form a gas giant is highly dependent on the disk properties and composition, while our chapters on snowline locations and C/N/O ratios also demonstrate that the disk structure and chemical composition has direct effects on the volatile composition of giant planets atmospheres. This thesis thus sets the stage to uncovering the role of disk volatile composition, dynamics and chemistry in shaping the compositions of nascent giant planets.

2

On the Minimum Core Mass For Giant Planet Formation at Wide Separations

ABSTRACT

In the core accretion hypothesis, giant planets form by gas accretion onto solid protoplanetary cores. The minimum (or critical) core mass to form a gas giant is typically quoted as $10M_{\oplus}$. The actual value depends on several factors: the location in the protoplanetary disk, atmospheric opacity, and the accretion rate of solids. Motivated by ongoing direct imaging searches for giant planets, this study investigates core mass requirements in the outer disk. To determine the fastest allowed rates of gas accretion, we consider solid cores that no longer accrete planetesimals, as this would heat the

gaseous envelope. Our spherical, two-layer atmospheric cooling model includes an inner convective region and an outer radiative zone that matches onto the disk. We determine the minimum core mass for a giant planet to form within a typical disk lifetime of 3 Myr. The minimum core mass declines with disk radius, from $\sim 8.5 M_{\oplus}$ at 5 AU to $\sim 3.5 M_{\oplus}$ at 100 AU, with standard interstellar grain opacities. Lower temperatures in the outer disk explain this trend, while variations in disk density are less influential. At all distances, a lower dust opacity or higher mean molecular weight reduces the critical core mass. Our non-self-gravitating, analytic cooling model reveals that self-gravity significantly affects early atmospheric evolution, starting when the atmosphere is only $\sim 10\%$ as massive as the core.

The contents of this chapter are published in *Piso, A.-M. & Youdin, A. N. 2014, ApJ, 786, 21*

2.1 INTRODUCTION

Models of giant planet formation fall in two categories: core accretion or gravitational instability (D’Angelo et al. 2011; Youdin & Kenyon 2013). In core accretion models, a solid core grows until it becomes massive enough to rapidly accrete gas (Perri & Cameron 1974; Mizuno et al. 1978). Gravitational instability (GI) theories investigate the fragmentation of the protoplanetary disk into bound clumps (Cameron 1978; Boss 1997).

Forming giant planets at wide separations in the protoplanetary disk poses theoretical challenges for both models. While disks cannot fragment close to their host star, GI is more promising in the outer disk (Matzner & Levin 2005; Rafikov 2005). However, for GI to form planetary mass objects versus brown dwarfs, both instantaneous disk conditions and the history of gas infall must be finely tuned (Kratter et al. 2010). The main concern for core accretion models, which are successful in the inner disk, is that they operate too slowly in the outer disk. The few Myr lifetime of gas disks sets the constraint (Williams & Cieza 2011). However, mechanisms for the rapid accretion of solids, even at large separations, exist (Dones & Tremaine 1993; Kenyon & Bromley 2009; Lambrechts & Johansen

2012). We thus consider the complementary problem of gas accretion timescales in the outer disk.

Core accretion models fall in several categories: static, quasi-static evolutionary and hydrodynamic. In static models, the accretion of planetesimals provides a steady luminosity that determines the structure and mass of the atmosphere (Stevenson 1982). For a given planetesimal accretion rate, static solutions only exist up to a maximum core mass, referred to as the “critical core mass”, M_{crit} . Above this mass, the atmosphere is assumed to collapse and rapidly accrete disk gas, a process known as the “core accretion instability.”

Many static studies reproduce a canonical $M_{\text{crit}} \sim 10M_{\oplus}$. However, Rafikov (2011, 2006, hereafter Ro6) finds a wide range of values, $0.1M_{\oplus} \lesssim M_{\text{crit}} \lesssim 100M_{\oplus}$, depending on the planetesimal accretion rate and disk parameters. Section 2.6.4 compares our results to Ro6. A general limitation of static models is the neglect of heat generated by atmospheric collapse, which can transform the core accretion instability into a slower process of Kelvin-Helmholtz (KH) contraction.

Quasi-static models include time-dependent atmospheric evolution due to KH contraction, and typically include a time-varying planetesimal accretion rate (Bodenheimer & Pollack 1986; Alibert et al. 2005). Successful quasi-static models describe three phases of giant planet formation (Pollack et al. 1996). In phase 1, rapid planetesimal accretion gives significant core growth, but prevents the accretion of a massive atmosphere. When planetesimal accretion abates, as the core’s feeding zone is depleted of solids, phase 2 begins. During phase 2, the atmosphere grows gradually, cooling by KH contraction. An ongoing trickle of planetesimal accretion can heat the atmosphere and slow this contraction. Eventually, the atmosphere reaches the “crossover mass”, when it equals the mass of the now slowly growing core. Phase 3, the runaway growth of the atmosphere, begins around the crossover mass. This runaway occurs quasi-statically, i.e. in hydrostatic balance, but very rapidly compared to disk lifetimes.

Dynamical models are needed to understand how runaway growth ends and final planet masses are determined. Relevant processes – including gap opening in disks and the transition of accretion

from spherical to planar – can be simulated and then added to atmospheric evolution calculations (Lissauer et al. 2009).

This work develops quasi-static models in which the core has a fixed mass and is no longer accreting solids. By isolating the process of KH contraction, we determine the minimum timescale for runaway atmospheric growth, and thus for giant planet formation by core accretion. Previous studies have considered this type of growth (Ikoma et al. 2000; Papaloizou & Nelson 2005, hereafter I00; PNo5, respectively), which is an end-member case of phases 2 and 3 in more detailed quasi-static models. Especially since phase 2 of atmospheric growth is often the slowest stage of core accretion, understanding the fastest allowed rates of gas accretion is of crucial importance. Our study develops simplified cooling models for the purposes of broadly exploring parameter space – especially in the outer disk – and developing a more detailed understanding of atmospheric accretion.

This paper is organized as follows. Section §4.2 describes our model of atmospheric growth. In Section §2.3, we develop a simplified analytic version of our atmospheric model. We describe the structure and evolution of our atmosphere solutions in Section §2.4. Section §2.5 gives our final results for growth timescales and critical core masses. We discuss some neglected effects in Section §2.6 and summarize our findings in Section §2.7. Some detailed derivations are presented in the appendices.

2.2 ATMOSPHERIC ACCRETION MODEL

To model the accretion of gas by a solid protoplanet, we develop a simplified two-layer model for time-dependent atmospheric growth via cooling, i.e. KH contraction. With a convective interior and radiative exterior, this model is motivated by similar models of hot Jupiters (Arras & Bildsten 2006; Youdin & Mitchell 2010).

Our model can treat atmospheric growth up to the early stages of runaway growth, around the crossover mass. At higher masses, our approximate treatment of the radiative zone (explained be-

low) breaks down. Since evolution after the onset of runaway growth contributes minimally to the total planet formation timescale, we can model growth times to good accuracy.

Our main assumptions are summarized as follows:

1. The atmosphere is spherically symmetric, remains in hydrostatic balance, and matches onto the disk’s midplane temperature and pressure at the planet’s Hill radius.
2. The core mass and radius are fixed in evolutionary calculations, neglecting ongoing planetesimal or dust accretion.
3. Gravitational contraction of the atmosphere is the only source of planetary luminosity.
4. Cooling of the atmosphere is dominated by the convective interior. Thus the luminosity in the radiative exterior is held spatially constant. We justify this assumption in §2.2.5 and confirm its validity in §2.4.3.
5. The atmosphere obeys a polytropic equation of state (EOS), with adiabatic index $\gamma = 7/5$ for an ideal diatomic gas. Corrections from a realistic EOS are discussed in §2.6.3 and deferred to future work.
6. Dust grains provide the opacity in the radiative zone. For the cool temperatures in the outer disk, the radiative layer remains cool enough to avoid dust sublimation. Other opacity choices are discussed in §2.6.2.

The first assumption of spherical accretion breaks down early in the inner disk, as explained below. However, our focus is on the outer disk, where this standard approximation is better justified.

2.2.1 DISK AND OPACITY MODEL

We adopt a minimum mass solar nebula (MMSN) model for a passively irradiated disk (Chiang & Youdin 2010). With the semimajor axis a normalized to the outer disk as $a_{10} = a/(10 \text{ AU})$, the gas

surface density and mid-plane temperature are

$$\Sigma_{\text{d}} = 70 F_{\Sigma} a_{10}^{-3/2} \text{ g cm}^{-2} \quad (2.1a)$$

$$T_{\text{d}} = 45 F_T a_{10}^{-3/7} \text{ K} . \quad (2.1b)$$

The normalization factors F_{Σ} and F_T adjust the model relative to the fiducial MMSN. We fix $F_{\Sigma} = F_T = 1$ unless noted otherwise. Some observations support a flatter surface density profile, $\Sigma_{\text{d}} \propto a^{-1}$ (Andrews et al. 2010). We find that gas density and pressure are weak corrections to atmospheric growth (see Section §2.5). However, a greater surface density of solids in the outer disk could favor the rapid growth of cores (Bromley & Kenyon 2011).

For a vertically isothermal disk in hydrostatic balance (with no self-gravity), the mid-plane pressure of disk gas is

$$P_{\text{d}} = 6.9 \times 10^{-3} F_{\Sigma} \sqrt{F_T} a_{10}^{-45/14} \text{ dyn cm}^{-2} \quad (2.2)$$

for a molecular weight of $\mu = 2.35$ proton masses and a Solar mass star.

The (thermodynamically isothermal) sound speed in the disk is

$$c_{\text{d}} = \sqrt{\mathcal{R} T_{\text{d}}} = 0.4 \sqrt{F_T} a_{10}^{3/14} \text{ km s}^{-1} , \quad (2.3)$$

in terms of the specific gas constant \mathcal{R} . The disk scale height is

$$H_{\text{d}} = c_{\text{d}} / \Omega = 0.42 \sqrt{F_T} a_{10}^{9/7} \text{ AU} , \quad (2.4)$$

in terms of the Keplerian frequency $\Omega = \sqrt{GM_*/a^3}$, with G the gravitational constant and M_* the stellar (in this work Solar) mass.

We assume a dust opacity characteristic of interstellar grains, following [Bell & Lin \(1994\)](#):

$$\kappa = 2F_\kappa \left(\frac{T}{100 \text{ K}} \right)^\beta \text{ cm}^2 \text{ g}^{-1}, \quad (2.5)$$

with a power-law index $\beta = 2$ and normalization $F_\kappa = 1$ unless noted otherwise. Grain growth tends to lower both F_κ and β , while dust abundance scales with F_κ . Section §2.6.2 discusses dust sublimation and more realistic opacity laws.

2.2.2 LENGTH SCALES

The characteristic length scales for protoplanetary atmospheres are crucial for choosing boundary conditions and for understanding the validity of spherical symmetry in a gas disk of scale height H_d .

The solid core has a radius

$$R_c \equiv \left(\frac{3M_c}{4\pi\rho_c} \right)^{1/3} \approx 10^{-4} m_{c10}^{1/3} \text{ AU}, \quad (2.6)$$

where the core mass, M_c , is normalized to 10 Earth masses as $m_{c10} \equiv M_c/(10 M_\oplus)$. The core density is held fixed at $\rho_c = 3.2 \text{ g cm}^{-3}$, representing a mixture of ice and rocky material ([Papaloizou & Terquem 1999](#)). We thus neglect the detailed EOS of the solid core ([Fortney et al. 2007](#)).

A planet can bind a dense atmosphere if its escape velocity exceeds the sound speed. This criterion is satisfied inside the Bondi radius

$$R_B \equiv \frac{GM_p}{c_d^2} \approx 0.17 \frac{m_{p10} a_{10}^{3/7}}{F_T} \text{ AU}, \quad (2.7)$$

where the enclosed planet mass, $M_p = M_c + M_{\text{atm}}$, includes the core and any atmosphere within the Bondi radius and $m_{p10} \equiv M_p/(10 M_\oplus)$. The contribution of the atmospheric mass is small in early evolutionary stages.

Stellar tides dominate the planet’s gravity beyond the Hill radius

$$R_H = \left(\frac{M_p}{3M_*} \right)^{1/3} a \approx 0.22 m_{p10}^{1/3} a_{10} \text{ AU}, \quad (2.8)$$

where spherical symmetry and hydrostatic balance break down. (Here we use the same symbol, M_p , to now mean the mass within R_H .)

The relevant length scales of the atmosphere and disk satisfy the relation $R_B H_d^2 = 3R_H^3$. The length scales are roughly equal at the “thermal mass” (e.g., [Menou & Goodman 2004](#))

$$M_{\text{th}} > \frac{c_d^3}{G\Omega} \approx 25 \frac{F_T^{3/2}}{\sqrt{m_*}} a_{10}^{6/7} M_{\oplus}. \quad (2.9)$$

In the low mass regime, $M_p < M_{\text{th}}/\sqrt{3}$, the length scales order as $R_B < R_H < H_d$. In this regime, many studies assume the atmosphere matches the disk conditions at R_B . We use R_H as the matching radius, i.e. outer boundary, in all regimes. We discuss this choice further below.

For a finite range of intermediate masses, $M_{\text{th}}/\sqrt{3} < M_p < 3M_{\text{th}}$, the Hill radius is the smallest scale, satisfying both $R_H < R_B$ and $R_H < H_d$. Spherical symmetry remains a good, if imperfect, approximation because the disk is only weakly vertically stratified on scales $\lesssim H_d$.

At higher planet masses where $M_p > 3M_{\text{th}}$ and $H_d < R_H < R_B$, spherical symmetry is no longer a good approximation, due to both the vertical stratification of the disk and gap opening. See §2.6.1 for further discussion of neglected hydrodynamic effects.

We quote planet masses as the enclosed mass within the smaller of R_B and R_H . Thus when $R_B < R_H$, our computational domain – which always ends at R_H – extends further than the location where we define atmosphere mass, within R_B . We emphasize that this mass definition does not affect the evolutionary calculation, which consistently includes the enclosed mass at all radii. We justify our mass convention as follows. First, we want to conservatively define planet mass in a way

that does not exaggerate atmospheric growth and is more consistent with previous works that use R_B as the outer boundary in this regime (e.g., [Ikoma et al. 2000](#), [Pollack et al. 1996](#)). Second, most of the gas outside R_B is weakly bound, and unlikely to remain attached to the planet if the disk suddenly dissipates.

The choice of R_H as the outer boundary is based on this being the largest radius where spherical hydrostatic balance is approximately (but not exactly, see §2.6.1) valid. When $R_B < R_H$, we thus include the fact that the density at R_B slightly exceeds the background disk density (see Ro6). In practice, this effect is not very significant. We would get similar results by choosing the outer boundary at R_B in this regime, as previous studies have done.

2.2.3 STRUCTURE EQUATIONS AND BOUNDARY CONDITIONS

Our atmosphere calculations use the standard structure equations of mass conservation, hydrostatic balance, thermal gradients, and energy conservation:

$$\frac{dm}{dr} = 4\pi r^2 \rho \quad (2.10a)$$

$$\frac{dP}{dr} = -\frac{Gm}{r^2} \rho \quad (2.10b)$$

$$\frac{dT}{dr} = \nabla \frac{T}{P} \frac{dP}{dr} \quad (2.10c)$$

$$\frac{dL}{dr} = 4\pi r^2 \rho \left(\epsilon - T \frac{\partial S}{\partial t} \bigg|_m \right), \quad (2.10d)$$

where r is the radial coordinate, L is the luminosity, and P , T , ρ and S are the gas pressure, temperature, density and entropy, respectively. The enclosed mass at radius r is m . Equation (2.10c) simply defines the temperature gradient $\nabla \equiv d \ln T / d \ln P$.

Radiation diffusion gives a temperature gradient

$$\nabla_{\text{rad}} \equiv \frac{3\kappa P}{64\pi G m \sigma T^4} L, \quad (2.11)$$

with σ the Stefan-Boltzmann constant. In our models, optically thick diffusion is a good approximation throughout the radiative zones. In convectively unstable regions, efficient convection gives an isentropic temperature gradient with $\nabla = \nabla_{\text{ad}}$, the adiabatic gradient

$$\nabla_{\text{ad}} \equiv \left(\frac{d \ln T}{d \ln P} \right)_{\text{ad}}. \quad (2.12)$$

According to the Schwarzschild criterion, convective instability occurs when $\nabla_{\text{rad}} > \nabla_{\text{ad}}$. Thus $\nabla = \min(\nabla_{\text{rad}}, \nabla_{\text{ad}})$ sets the temperature gradient.

In the energy equation (2.10d), ϵ represents all local sources of heat input, except for the motion of the atmosphere itself. From stellar structure, ϵ may be familiar as a nuclear burning term. In a protoplanetary atmosphere, dissipative drag on planetesimals contributes to ϵ . Our models set $\epsilon = 0$, consistent with our neglect of planetesimal accretion.

The energy input from gravitational contraction, $\epsilon_g = -T \partial S / \partial t$, is crucial for a cooling model.* The partial time derivative would normally require our radial derivative to be partial as well. However, our subsequent developments will replace the local energy equation (2.10d) with global energy balance (see section §2.2.4), reverting the structure equations to time-independent ordinary differential equations (ODEs).

To solve the equation set (2.10), an EOS is required for closure. In our study, we adopt an ideal gas law with a polytropic EOS

$$P = \rho \mathcal{R} T, \quad (2.13a)$$

$$S = \mathcal{R} \ln \left(\frac{T^{1/\nabla_{\text{ad}}}}{P} \right), \quad (2.13b)$$

with S a relative entropy. This work uses $\nabla_{\text{ad}} = 2/7$, i.e. a polytropic index $\gamma \equiv 1/(1 - \nabla_{\text{ad}}) =$

*In general, any motion is accounted for by this term. The partial time derivative is performed on shells of fixed mass.

7/5, for an ideal diatomic gas.[†] We thus neglect the presence of monatomic Helium in our choice of polytropes, a common practice in idealized studies. We do, however, account for Helium in our reference value of $\mu = 2.35$ proton masses.

Boundary conditions must be satisfied at both the base and the top of the atmosphere, with $m(R_c) = M_c$, $T(R_H) = T_d$ and $P(R_H) = P_d$. Our model atmospheres also obey $L(R_c) = 0$. Along with Equation (2.10d), this boundary condition is incorporated in the global cooling model described below.

2.2.4 GLOBAL COOLING OF AN EMBEDDED PLANET

We now consider the global energy balance of a planet embedded in a gas disk. More generally, our derivation applies to any spherical, hydrostatic object in pressure equilibrium with a background medium. The total atmospheric energy includes gravitational and internal energies, $E = E_G + U$, with

$$E_G = - \int_{M_c}^M \frac{Gm}{r} dm, \quad (2.14a)$$

$$U = \int_{M_c}^M u dm. \quad (2.14b)$$

The specific internal energy is $u = C_V T = \mathcal{R}(\nabla_{\text{ad}}^{-1} - 1)T$ for a polytropic EOS. For a star or coreless planet, $M_c = 0$.

We start with a standard result, global energy balance for an isolated, i.e. not embedded, planet:

$$L_M = L_c + \Gamma - \dot{E}. \quad (2.15)$$

The surface luminosity, L_M , includes the core luminosity L_c from e.g. planetesimal accretion or

[†]Equation (2.13b) is equivalent to the standard polytropic relation, $P = K\rho^\gamma$, if the polytropic index K replaces S .

radioactive decay. The total heat generation Γ is the integral of ϵ over the atmosphere. The rate of change of atmospheric energy, \dot{E} , is a loss term.

For an object with no core luminosity (or no core) and no internal heat sources, the energy equation $L_M = -\dot{E}$ describes KH contraction in its simplest form. When internal heat sources dominate, $L_M = \Gamma$, e.g. for nuclear burning in a main sequence star.

A protoplanetary atmosphere embedded in a gas disk lacks a free surface. For objects without a free surface (or interior to a free surface), the full energy equation,

$$L_M = L_c + \Gamma - \dot{E} + e_M \dot{M} - P_M \left. \frac{\partial V_M}{\partial t} \right|_M, \quad (2.16)$$

acquires surface terms as derived in Appendix A. The surface can be at any mass level M , where the instantaneous radius is R . Surface quantities are labeled by M subscripts (except for R). The energy accreted across the surface is given by the specific energy, $e_M = u_M - GM/R$, and the mass accretion rate of gas, \dot{M} . The work done by the surface is $P_M \partial V_M / \partial t$, with the partial derivative performed at fixed mass.

For static solutions, which are not the focus of this paper, the surface terms (and also \dot{E}) vanish. Static solutions are valid when imposed heat sources, i.e. L_c and Γ , exceed the atmospheric losses. Quantitatively, static solutions apply when the KH timescale,

$$\tau_{\text{KH}} \sim \frac{|E|}{L_M}, \quad (2.17)$$

is shorter than the actual evolutionary timescale. Thus, τ_{KH} , which our models calculate, gives strong lower limits on the time to form giant planets by core accretion.

2.2.5 THE TWO-LAYER MODEL

To simplify our evolutionary calculations, we develop a two-layer atmospheric model with a convective interior and a radiative exterior. The existence of this layered structure is well known from previous studies (e.g., Ro6) and can be readily understood. Before the protoplanetary atmosphere can cool, it has the entropy of the disk. As the atmosphere cools, the deep interior remains convective. Convective interiors are a common feature of low mass cool objects (brown dwarfs and planets) that results from the behavior of ∇_{rad} for realistic opacity laws. However, the entropy of the deep interior decreases as the atmosphere cools. A region of outwardly increasing entropy, i.e. a radiative layer, is required to connect the convective interior to the disk. A more complicated structure, with radiative windows in the convection zone, is possible as discussed in §2.6.2.

In convective regions, the adiabatic structure is independent of luminosity and can be calculated without local energy balance, Equation (2.10d). Thus, for fully convective objects, a cooling sequence can be established by connecting a series of adiabatic solutions using a global energy equation, $L_M = -\dot{E}$ or Equation (2.15). Such methods are commonly used for their computational efficiency and are sometime referred to as “following the adiabats,” since the steady state solutions evolve in order of decreasing entropy (Marleau & Cumming 2014).

In the radiative zone, local energy balance, Equation (2.10d), does affect the atmospheric structure. We proceed by assuming that the majority of energy is lost from the convective interior, and thus the luminosity can be treated as constant in the outer radiative zone, i.e. the RHS of Equation (2.10d) is set to zero. This assumption greatly simplifies the numerical problem. Instead of solving time dependent partial differential equations, we can solve for static solutions to a set of ODEs, Equations (2.10a – c), which we connect in a time series as described below. We show in §2.4.3 that the approximation of constant luminosity in the outer layer holds for our regime of interest.

To obtain a single atmosphere solution (indexed by i), we choose a planet mass M_i . At the outer

boundary, at $R_H(M_i)$, the temperature and pressure are set to the disk values. A luminosity value is required to compute ∇_{rad} and integrate Equations (2.10a–c). The correct value of the luminosity is not known in advance, and is the eigenvalue of the problem. The boundary conditions can only be satisfied for the correct value of the luminosity eigenvalue, which we find by the shooting method. Specifically, we alter the luminosity until the integrated value of mass at the core, $m(R_c)$, matches the actual core mass, M_c . Physically, the luminosity determines the location of the radiative-convective boundary (RCB), consistent with the structure equations and the Schwarzschild criterion.

To understand time evolution, we construct an array of solutions to Equations (2.10a – c) in order of increasing atmospheric mass. We then use global energy balance, Equation (2.16), to “follow the mass” and place these solutions in a cooling sequence. To establish the time difference between neighboring solutions, we apply Equation (2.16) at the RCB. In principle, energy balance could be evaluated at any level. Our approximate treatment of the radiative zone makes the RCB the preferred location. The elapsed time Δt between states i and $i + 1$ is given by the finite difference

$$\Delta t = \frac{-\Delta E + \langle e \rangle \Delta M - \langle P \rangle \Delta V_{\langle M \rangle}}{\langle L \rangle}, \quad (2.18)$$

using Equation (2.16) with $\Gamma = L_c = 0$. Brackets indicate an average of, and Δ indicates a difference between, the two states. All values are evaluated at the RCB. Due to the partial derivative in Equation (2.16), the volume difference $\Delta V_{\langle M \rangle}$ is performed at fixed mass, here the average of the masses at the RCB.

2.3 ANALYTIC COOLING MODEL

This section develops the analytic version of our two-layer model. This analytic model is less accurate than our numerical model, primarily because it neglects self-gravity. We show (in §2.4) that

self-gravity becomes important at rather low atmospheric masses, $M_{\text{atm}} \gtrsim 0.1 M_c$. Nevertheless, the analytic model is useful for understanding atmospheric evolution and interpreting the numerical results.

The analytic model also assumes that the upper radiative layer is thick enough that $P_{\text{RCB}} \gg P_d$. This approximation ignores the earliest stages of cooling, which are rapid enough to be of minor importance. The analytic model also ignores the surface terms in Equation (2.16), which we show to be a modest correction in §2.4.3. Finally, while the numerical models set the outer boundary at R_H , we simplify the analytic calculations by setting the outer boundary to infinity, effectively neglecting the finite scale-height of the disk. As shown in Appendix B.0.1, the effect of this approximation is minor for $R_B \lesssim R_H$, the primary case of interest (see also Ro6).

Of all the approximations, the neglect of self-gravity is by far the most significant, as we have verified by comparison to numerical integrations that only neglect self-gravity.

2.3.1 TWO LAYER STRUCTURE

In order to apply the two-layer cooling model analytically, we require expressions for the atmospheric structure. Conditions at the RCB are crucial as they set the interior adiabat and the radiative losses from the interior. (Recall that luminosity generation in the radiative zone is neglected.) We express the temperature and pressure of the RCB, at the radius R_{RCB} , as

$$T_{\text{RCB}} = \chi T_d \tag{2.19a}$$

$$P_{\text{RCB}} = \theta P_d e^{R_B/R_{\text{RCB}}} . \tag{2.19b}$$

The leading constants would be unity, $\chi = \theta = 1$, if the radiative zone were replaced by an isothermal layer. In practice, deviations from unity are modest. Standard radiative structure calculations

(see Appendix B.o.2 for details) give

$$\chi \simeq \left(1 - \frac{\nabla_{\text{ad}}}{\nabla_{\infty}}\right)^{-\frac{1}{4-\beta}} \simeq 1.53, \quad (2.20)$$

for $P_{\text{RCB}} \gg P_{\text{d}}$, our regime of interest, and with the radiative temperature gradient at depth, $\nabla_{\infty} = 1/2$, for our dust opacity. The radiative zones are thus nearly isothermal, as found by Ro6.

A numerical integration gives $\theta \simeq 0.556$ for our parameters.

Given the conditions at the RCB, the density and temperature profiles along the interior adiabat,

$$\rho = \rho_{\text{RCB}} \left[1 + \frac{R'_{\text{B}}}{r} - \frac{R'_{\text{B}}}{R_{\text{RCB}}}\right]^{1/(\gamma-1)} \quad (2.21a)$$

$$T = T_{\text{RCB}} \left[1 + \frac{R'_{\text{B}}}{r} - \frac{R'_{\text{B}}}{R_{\text{RCB}}}\right], \quad (2.21b)$$

follow from hydrostatic balance. We introduce an effective Bondi radius

$$R'_{\text{B}} \equiv \frac{GM_{\text{c}}}{C_P T_{\text{RCB}}} = \frac{\nabla_{\text{ad}}}{\chi} R_{\text{B}} \quad (2.22)$$

to simplify expressions, with $C_P = \mathcal{R}/\nabla_{\text{ad}}$ the specific heat capacity at constant pressure.

Deep in the adiabatic interior, where $r \ll R_{\text{RCB}} \ll R'_{\text{B}}$, the profiles follow simple power laws,

$$\rho \simeq \rho_{\text{RCB}} \left[\frac{R'_{\text{B}}}{r}\right]^{1/(\gamma-1)} \propto r^{-5/2} \quad (2.23a)$$

$$T \simeq T_{\text{RCB}} \frac{R'_{\text{B}}}{r} = \frac{GM_{\text{c}}}{C_P r}. \quad (2.23b)$$

While the radial density profile depends on the adiabatic index, the r^{-1} temperature scaling is universal. In self-gravitating models, the temperature gradient,

$$\frac{dT}{dr} = -\frac{Gm(r)}{C_P r^2}, \quad (2.24)$$

gives a profile that is flatter than $T \propto r^{-1}$.

Returning to our non-self-gravitating model, the total specific energy at depth,

$$e = e_g + u = -\nabla_{\text{ad}} \frac{GM_c}{r}, \quad (2.25)$$

is simply proportional to the gravitational potential, $e_g = -GM_c/r$.

2.3.2 MASS, ENERGY AND LUMINOSITY

The most relevant quantities for global cooling are the integrated energy, luminosity, and atmospheric mass. In our non-self-gravitating limit, the mass of our nearly isothermal radiative zones is less than the convective interior, as shown in Appendix B.0.1.

The atmospheric mass is thus given by the integration of Equation (2.21a),

$$M_{\text{atm}} = \frac{5\pi^2}{4} \rho_{\text{RCB}} R_{\text{B}}'^{5/2} \sqrt{R_{\text{RCB}}}, \quad (2.26)$$

in the relevant limit $R_c \ll R_{\text{RCB}} \ll R_{\text{B}}'$ and for $\gamma = 7/5$. Mass is concentrated near the outer regions of the convective zone, a result that holds for $\gamma > 4/3$.

Using Equation (2.19b) to eliminate R_{RCB} , the ratio of atmosphere to core mass becomes

$$\frac{M_{\text{atm}}}{M_c} = \frac{P_{\text{RCB}}}{\xi P_M}, \quad (2.27)$$

where we define a characteristic pressure and a logarithmic factor:

$$P_M \equiv \frac{4\nabla_{\text{ad}}^{3/2}}{5\pi^2\sqrt{\chi}} \frac{GM_c^2}{R_{\text{B}}'^4} \quad (2.28a)$$

$$\xi \equiv \sqrt{\ln[P_{\text{RCB}}/(\theta P_d)]}. \quad (2.28b)$$

The atmosphere mass increases as radiative losses lower the internal adiabat and increase P_{RCB} .

The crossover mass, $M_{\text{atm}} = M_c$, is reached when

$$P_{\text{RCB}} = \xi P_M, \quad (2.29)$$

i.e. near the characteristic pressure P_M . The critical value of the order unity factor ξ is found by eliminating P_{RCB} from Equations (2.28b) and (2.29). This logarithmic factor complicates our analytic description. Since it remains order unity, we simply hold it fixed in our scalings.

The total energy is concentrated towards the core if $|e|\rho r^3 \propto \rho r^2$ drops with increasing r . This condition requires $\gamma < 3/2$, which our choice of $\gamma = 7/5$ satisfies, but $\gamma = 5/3$ (monatomic gas) would not.

Integration of Equation (2.25) over the mass of the atmosphere thus gives

$$E = -4\pi \nabla_{\text{ad}} G M_c \int_{R_c}^{R_{\text{RCB}}} \rho r dr \quad (2.30a)$$

$$\approx -4\pi P_{\text{RCB}} R_B' \frac{1}{\nabla_{\text{ad}}} \left(\frac{\gamma - 1}{3 - 2\gamma} \right) R_c^{\frac{2\gamma-3}{\gamma-1}} \quad (2.30b)$$

$$\approx -8\pi P_{\text{RCB}} \frac{R_B'^{7/2}}{\sqrt{R_c}}, \quad (2.30c)$$

with $\gamma < 3/2$ and $\gamma = 7/5$ in Equations (2.30b) and (2.30c), respectively.

The emergent luminosity from the RCB,

$$L_{\text{RCB}} = \frac{64\pi G M_{\text{RCB}} \sigma T_{\text{RCB}}^4}{3\kappa P_{\text{RCB}}} \nabla_{\text{ad}} \approx L_d \frac{P_d}{P_{\text{RCB}}}, \quad (2.31)$$

follows from Equation (2.11) and marginal convective stability, $\nabla_{\text{rad}} = \nabla_{\text{ad}}$, where we define

$$L_d \equiv \frac{64\pi G M_{\text{RCB}} \sigma T_d^4}{3\kappa(T_d) P_d} \nabla_{\text{ad}} \chi^{4-\beta}. \quad (2.32)$$

The scaling $L_{\text{RCB}} \propto 1/P_{\text{RCB}}$ shows that luminosity drops as the atmosphere cools and P_{RCB} deepens. This result relies on the pressure independence of dust opacities. For fully non-self-gravitating results, we replace M_{RCB} , the mass up to the RCB, with the core mass, but the mass of the convective atmosphere can be included for a slightly higher order estimate.

2.3.3 COOLING TIMES & CORE MASSES

Our analytic cooling model uses $L = -\dot{E}$, neglecting the surface terms in Equation (2.16).[‡] Applying Equations (2.30c) and (2.31), the time it takes to cool the atmosphere until the RCB reaches a given pressure depth, P_{RCB} , is

$$t_{\text{cool}} = - \int_{P_d}^{P_{\text{RCB}}} \frac{dE/dP_{\text{RCB}}}{L_{\text{RCB}}} dP_{\text{RCB}} \quad (2.33a)$$

$$\approx 4\pi \frac{P_{\text{RCB}}^2}{P_d} \frac{R_B'^{7/2}}{L_d \sqrt{R_c}}. \quad (2.33b)$$

The initial RCB depth is set to P_d as a formality. The cooling slows as it proceeds with $t_{\text{cool}} \propto P_{\text{RCB}}^2$.

We expect runaway growth to begin around the crossover mass, $M_{\text{atm}} = M_c$. Equations (2.33) and (2.29) give the time to crossover as

$$t_{\text{co}} \approx 2 \times 10^8 \frac{F_T^{5/2} F_\kappa \left(\frac{\xi}{3.4}\right)^2}{m_{c10}^{5/3} a_{10}^{15/14}} \text{ yr}. \quad (2.34)$$

We estimate the critical core mass, M_{crit} , by equating the crossover time with a typical protoplanetary disk lifetime,

$$t_d = 3 \times 10^6 \text{ yr}. \quad (2.35)$$

[‡]Appendix B.o.4 shows that these terms are negligible for a non-self-gravitating model.

Setting $t_{\text{co}} = t_{\text{d}}$ gives

$$M_{\text{crit}} \approx 100 \frac{F_T^{3/2} F_\kappa^{3/5} \left(\frac{\xi}{2.6} \right)^{6/5}}{a_{10}^{9/14}} M_\oplus. \quad (2.36)$$

Both t_{co} and M_{crit} are too large to be interesting, or to be correct based on previous results and the numerical results in this paper. The main reason for this discrepancy is the neglect of self-gravity. Section 2.4 explores in detail the effects of self-gravity on atmospheric structure, luminosity and evolution. One might expect self-gravity to be only a modest correction for $M_{\text{atm}} \leq M_c$. This seemingly reasonable expectation can be misleading, an interesting result in itself.

Aside from this insight, the analytic model is useful because, despite the amplitude error, it explains the basic scaling of numerical cooling models. As is well known (Hubickyj et al. 2005), a lower opacity, here scaling with F_κ , allows faster cooling and gives a lower critical core mass. The cooling timescale and critical core mass depend only weakly on the disk pressure, via the logarithmic factor ξ . The almost exponential rise in radiative zone pressure with depth, see Equation (2.19b), explains why disk pressure has only a weak effect on cooling at the RCB.

Lower disk temperatures decrease both t_{co} and M_{crit} . The decline in both quantities with semi-major axis is completely explained by the temperature profile (ignoring the logarithmic factor ξ). The temperature dependence is a competition between two main effects. The Bondi radius, which quantifies the strength of gravity, decreases for lower temperatures. On the other hand, the luminosity, $\propto T^{4-\beta}$, is lower at colder temperatures, which slows cooling and opposes the overall effect. With $t_{\text{co}} \propto F_T^{\beta+1/2}$, the slope of the dust opacity, β , is an important factor in regulating the resulting growth time.

To facilitate comparison with our numerical results, we rescale the analytic results as follows. Since growth times are too slow in the non-self-gravitating analytic model, we modify the runaway growth criterion to occur at an effective crossover mass $M_{\text{atm}} = f M_c$, with $f < 1$. Specifically, we choose $f = 0.13$, because with this value the analytic model gives the same critical core mass at

10 AU as the numerical model, for our standard choices of other parameters. This prescription does not mean that runaway growth physically occurs at low atmosphere masses, nor does it cause perfect agreement between the models. Rather by artificially accelerating growth in the analytic model, we can more easily compare the parameter scalings of the two models. Mathematically, the modified crossover mass amounts to replacing $\xi \rightarrow f\xi$ in our analysis. With $f = 0.13$, the revised scalings are

$$t_{\text{run}} \approx 3 \times 10^6 \frac{F_T^{5/2} F_\kappa \left(\frac{\xi}{3.4}\right)^2}{m_{\text{c10}}^{5/3} a_{10}^{15/14}} \text{ yr} \quad (2.37a)$$

$$M_{\text{crit}} \approx 8 \frac{F_T^{3/2} F_\kappa^{3/5} \left(\frac{\xi}{2.6}\right)^{6/5}}{a_{10}^{9/14}} M_\oplus, \quad (2.37b)$$

now using t_{run} , defined as the time when $M_{\text{atm}} = f M_{\text{c}}$, instead of t_{co} for the runaway growth timescale. When plotting these rescaled analytic results, we include the variations in ξ from Equation (2.28b).

2.4 QUASI-STATIC KELVIN-HELMHOLTZ CONTRACTION

We examine the structure and evolution of our model atmospheres, calculated as described in §4.2. For comparison, we also show results of the non-self-gravitating analytic model of §2.3. Radial structure is presented in §2.4.1, time evolution is described in §2.4.2, and the validity of our two-layer cooling model is examined in §2.4.3.

2.4.1 ATMOSPHERIC STRUCTURE

Figure 2.1 shows radial profiles at different stages of atmospheric growth around a $5M_\oplus$ core at 60 AU. Quoted mass values include the core plus atmosphere within the smaller of R_{B} or R_{H} , which for these cases is R_{B} . The $8.99 M_\oplus$ solution is the mass that satisfies our runaway growth criteria (described in §2.4.2).

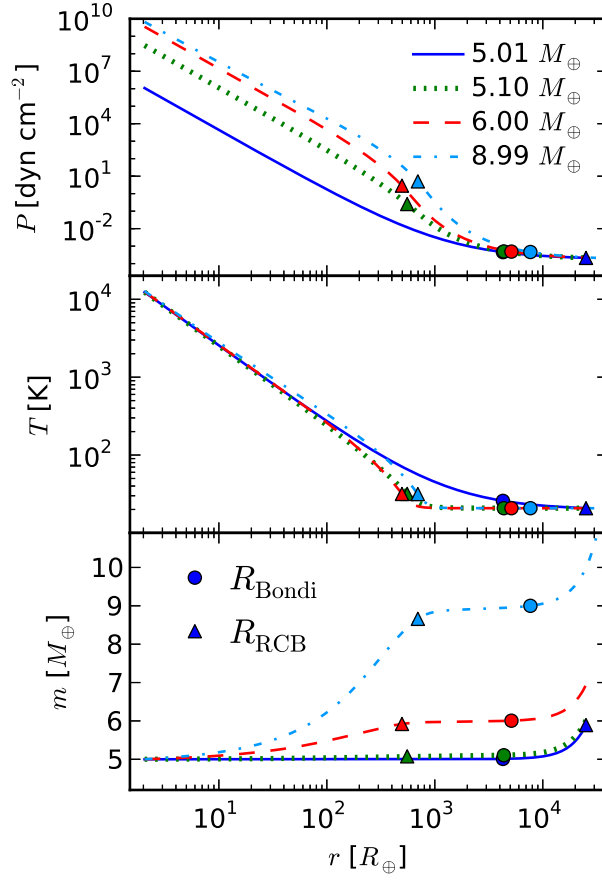


Figure 2.1: Radial profiles of atmospheric pressure, temperature and enclosed mass (core included) for a $5M_{\oplus}$ core at 60 AU. Solid, dotted, dashed and dot-dashed lines correspond to solutions with total mass (core and atmosphere) of $5.01M_{\oplus}$, $5.10M_{\oplus}$, $6.00M_{\oplus}$ and $8.99M_{\oplus}$, respectively (see text for significance of these masses). Circles and triangles mark the locations of the Bondi radii and of the radiative-convective boundaries, respectively. The radial profiles extend from the core to the Hill radius.

The lowest mass atmosphere – which we take as our initial state – is fully convective and shares the disk’s entropy. In Figure 2.1 this state is the $5.01 M_{\oplus}$ solution with no radiative zone.

Cooling and contraction allow the atmosphere to accrete more gas. In the convective zones, higher mass solutions have lower entropy and higher pressures. A radiative zone emerges to connect the lower entropy interior to the higher entropy disk. Figure 2.1 shows that this radiative zone is

already fairly deep in the $5.10 M_{\oplus}$ solution.

The atmospheric structure is well approximated by our non-self-gravitating, analytic solutions. Deep in convective zones, thermal energy is a fixed fraction of the gravitational potential energy, giving $T \propto r^{-1}$ and $P \propto r^{-1/\nabla_{\text{ad}}}$ as in Equation (2.23). This behavior is seen in Figure 2.1 for $r \ll R_{\text{RCB}}$. Near the core, Equation (2.23b) gives the core temperature, $T_c = GM_c/(C_P R_c)$, unaffected by the overlying atmosphere mass which does not contribute to the gravitational potential. Closer to the RCB, self-gravity is no longer negligible, particularly for large envelope masses. Instead, these high mass solutions show a slightly flatter profile in T and also in $P \propto T^{1/\nabla_{\text{ad}}}$, as explained by Equation (2.24).

In agreement with Equation (2.19), the radiative zones remain nearly isothermal, even for the higher masses. Consequently, the pressure increases nearly exponentially with depth.

2.4.2 TIME EVOLUTION

The cooling model of §2.2.5 is used to connect solutions with different atmospheric masses into an evolutionary sequence. Figure 2.2 shows the luminosity evolution and the elapsed time as a function of atmospheric mass for the same parameters as in Figure 2.1.

During the early stages of atmospheric growth, the luminosity drops sharply. This behavior is seen in both the full numerical solutions and the analytic model. With increasing atmospheric mass, the pressure depth of the RCB increases, along with the optical depth ($\propto \kappa P_{\text{RCB}}$). Consequently, the radiative luminosity decreases. This behavior is described in Equations (2.27) and (2.31).

At later stages of evolution, the numerical model in Figure 2.2 shows a flat luminosity with increasing mass and also time (not shown). By contrast, the non-self-gravitating analytic model gives a luminosity that continues to drop as the atmosphere becomes more massive. To understand this difference, consider the scaling of Equation (2.31), $L_{\text{RCB}} \propto M_{\text{RCB}} T_{\text{RCB}}^4 / (\kappa_{\text{RCB}} P_{\text{RCB}})$, which holds in both cases. Accounting for the higher enclosed mass in the self-gravitating model gives a

somewhat higher luminosity, as desired. However, the main effect is that Equation (2.27) – which describes a nearly linear relation between atmospheric mass and RCB pressure – breaks down for self-gravitating solutions. This behavior can be seen in the top panel of Figure 2.1 where the P_{RCB} increases significantly from 5.10 to 6.0 M_{\oplus} , but only increases relatively modestly with further growth to 8.99 M_{\oplus} . In the higher mass solutions, the relatively low P_{RCB} values (and thus the relatively high luminosities) require an outward shift in R_{RCB} , as shown in Figure 2.1. This shift does not occur in the analytic solution, where R_{RCB} continually decreases with atmospheric mass (cf. Equations 2.19b and 2.27).

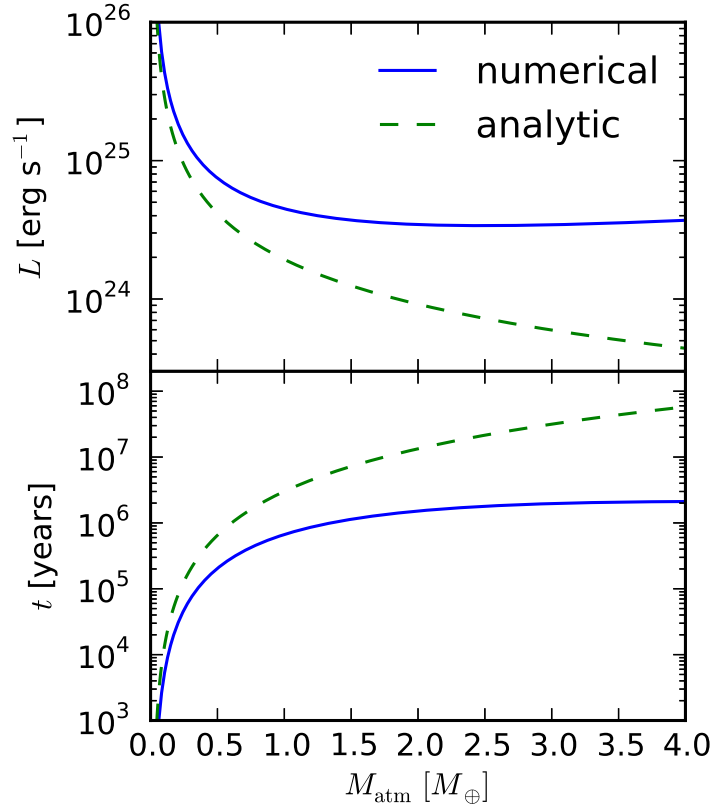


Figure 2.2: Evolution of the luminosity and elapsed time during atmospheric growth around a $5M_{\oplus}$ core at 60 AU. The luminosity is initially high, then decreases as the atmosphere grows in mass and the radiative zone becomes optically thicker. Due to the neglect of self-gravity, the analytic model (*dashed curve*) gives luminosities that are too low and evolution times that are too long.

The accelerated growth in the numerical model, as shown in the bottom panel of Figure 2.2, is also a direct result of the higher cooling luminosities with self-gravity included. Even when M_{atm}/M_c is only few percent, i.e. well before the crossover mass, the effect of self-gravity is quite evident. Closer to the star, the effects of self-gravity are not as strong for low atmosphere masses. Nevertheless, all our models show that self-gravity noticeably accelerates growth for $M_{\text{atm}} > 0.1M_c$.

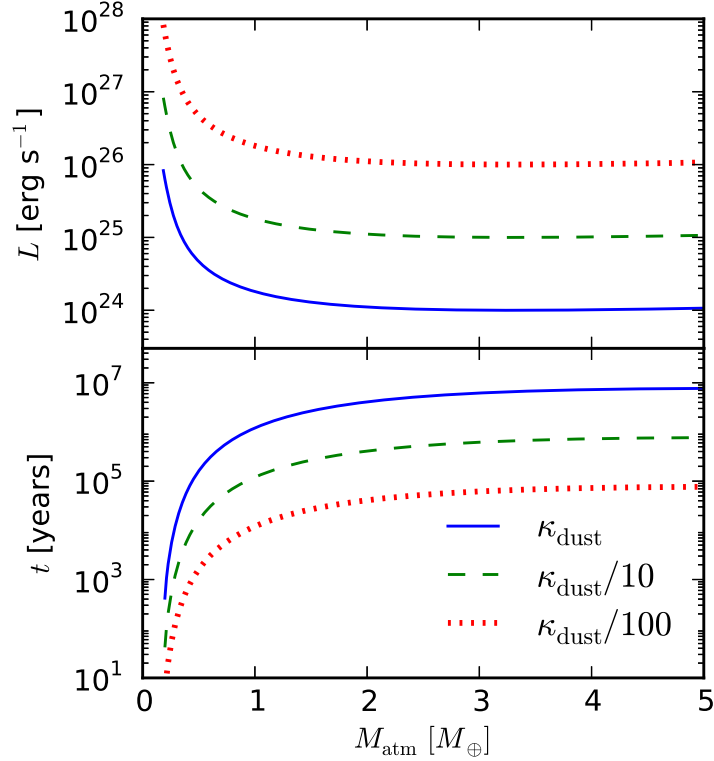


Figure 2.3: The effect of dust abundance on atmospheric evolution. Reducing dust opacities by factors of 10 and 100 from standard Solar abundances gives higher luminosities and faster atmospheric growth. Plotted quantities are similar to Figure 2.2, but for a $5M_{\oplus}$ core at 10 AU.

In Figure 2.3, our standard dust opacity, Equation (2.5), is reduced by factors of 10 and 100. Lower opacities result in higher luminosities and faster evolution. Our model thus confirms a well-established result (Hubickyj et al. 2005). While clearly an important effect, atmospheric dust opacities are difficult to robustly predict. Ablation of infalling solids is a dust source. Sinks include the

sequestration of solids in the core and dust settling through the radiative zone. Grain growth both reduces dust opacities per unit mass and favors settling. Our scenario of negligible ongoing particle accretion tends to favor low dust opacities. To be conservative, however, our reference case considers full Solar abundances. The effect of opacity reduction on the critical core mass is described in §2.5.

Figure 2.4 plots the evolution of the atmospheric growth timescale, M_{atm}/\dot{M} , around a $5M_{\oplus}$ core at several locations in our reference disk model. This instantaneous growth time shows clearly that the atmosphere spends the bulk of its time growing through intermediate atmospheric masses, $\sim 1 - 3 M_{\oplus}$ in this case. Growth times are short both early – when the radiative zone is transparent – and late – when self-gravity accelerates growth.

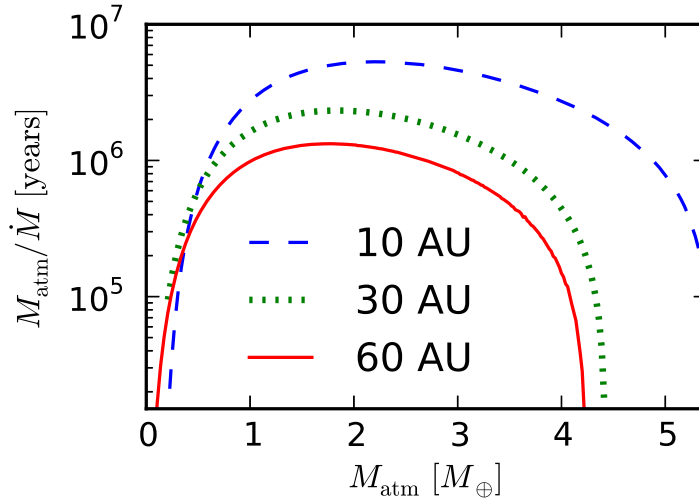


Figure 2.4: Evolution of the atmospheric growth timescale with mass around a $5M_{\oplus}$ solid core located at 10, 30 or 60 AU, for standard Solar opacities. Growth is slowest for $M_{\text{atm}} \sim 1 - 3M_{\oplus}$, i.e. before the crossover mass at $M_{\text{atm}} = M_c$.

The fact that growth times have a well defined maximum is a characteristic of accelerating growth. Unlike our analytic model, which must assume that runaway growth begins near the crossover mass, our numerical model allows us to measure when runaway accretion starts. Runaway growth

does not begin at a universal value of M_{atm}/M_c . Further from the star, runaway growth begins at smaller M_{atm}/M_c , as Figure 2.4 shows. Figure 2.6 (described in the next section) shows how the onset of runaway growth depends on core mass.

We quantify the runaway growth timescale, t_{run} , as the time when M_{atm}/\dot{M} drops to 10% of its maximum value. The choice of 10% is arbitrary; the precise threshold chosen is relatively unimportant because growth continues to accelerate.

2.4.3 VALIDITY OF THE TWO-LAYER COOLING MODEL

We examine the validity of our cooling model by comparing our model luminosity to the neglected luminosity, L_{negl} , that a more detailed model would generate in the radiative zone. We compute L_{negl} from the entropy difference between successive radiative zone solutions. We then integrate the energy equation, $\partial L/\partial m = -T\partial S/\partial t$, over the average depth of the radiative zone.[§]

Figure 2.5 shows that the neglected luminosity is indeed negligible during the early stages of evolution. However, L_{negl} exceeds the model luminosity, L , at high masses, $M_{\text{atm}} > 3M_{\oplus}$ in this case. Our cooling model is thus inaccurate at higher masses. However, the model remains reasonably accurate up to the beginning stages of runaway growth, which is sufficient for our purposes of widely exploring parameter space and exploring trends.

The individual terms in the global cooling model of Equation (2.16), evaluated at the RCB, are also plotted in Figure 2.5. At low masses, the change in energy, $-\dot{E}$, makes the dominant contribution to luminosity. As the mass increases, the surface terms become more significant, led by the accretion energy. However, the surface terms are everywhere smaller than L_{negl} . Thus wherever our model is accurate – including the crucial early phases of growth – surface terms are a minor correction. The neglect of surface terms in the analytic model is thus not a serious omission.

[§]While useful as a diagnostic, the neglected luminosity cannot reliably correct the global cooling model because the effects of L_{negl} on the structure of the radiative zone are still ignored.

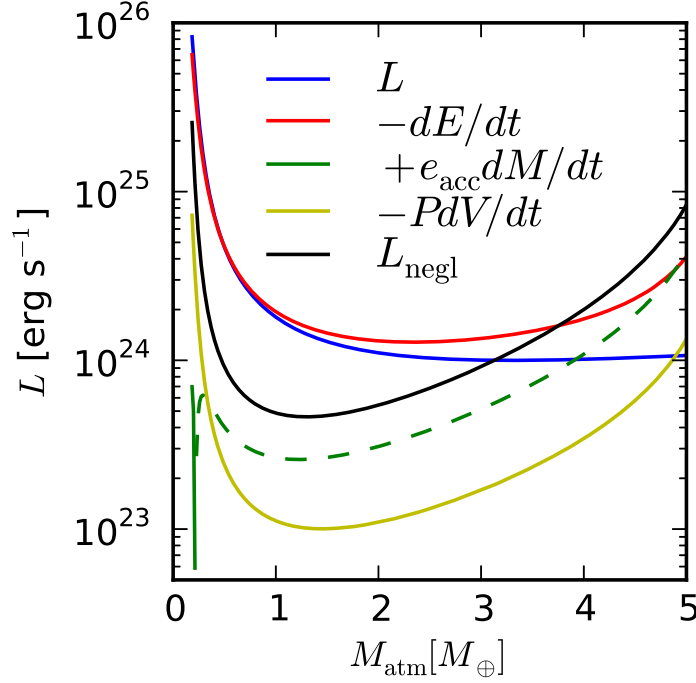


Figure 2.5: Individual terms in the atmospheric cooling model of Equation (2.16), for a $5M_{\oplus}$ core at 10 AU. The dashed curve for accretion energy indicates a negative contribution. All quantities are evaluated at the RCB, except for L_{negl} , the extra luminosity that would have been generated in the radiative zone, but is neglected in our model. The neglected luminosity is a small correction to the model luminosity L for $M_{\text{atm}} \lesssim 3M_{\oplus}$. Since these low masses dominate growth times, our model is roughly accurate.

2.5 RESULTS FOR GIANT PLANET FORMATION

We now use our structure and evolution models to estimate the timescales and minimum core masses for giant planet formation for a range of disk conditions and other model parameters. Our results for atmosphere growth times – the time for a core of fixed mass to undergo runaway gas accretion – are presented in §2.5.1. Section 2.5.2 gives our results for critical core masses, the minimum values that trigger runaway atmospheric growth within a plausible disk lifetime, here 3 Myr.

Our models focus on giant planet formation between 5 and 100 AU, as the outer disk is of par-

ticular interest for direct imaging searches. The growth of atmospheres close to the star is also important, but spherical accretion models (including ours) are less applicable here. In the inner disk, critical core masses increase, yet lower mass planets start to open gaps and outgrow the disk scale height, see Equation (2.9). These concerns prevent us from applying our model to the inner disk.

2.5.1 RUNAWAY GROWTH TIMESCALE

The time to undergo atmospheric runaway growth, t_{run} , sets a minimum timescale for the formation of giant planets. Due to the accelerating nature of runaway growth, the precise threshold chosen for t_{run} (explained in §2.4.2) is of minor significance.

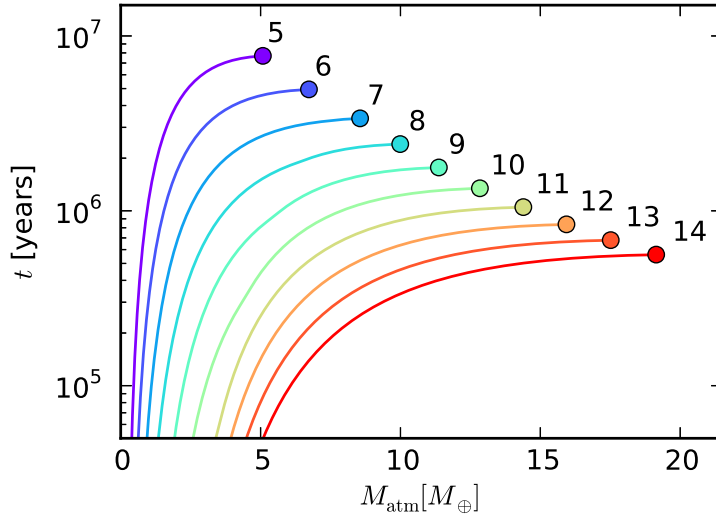


Figure 2.6: Time to grow an atmosphere of mass M_{atm} for cores with fixed masses between $5M_\oplus$ and $14M_\oplus$ (as labeled) at 10 AU in our fiducial disk. Circles mark the runaway growth time, t_{run} , which occurs at roughly the crossover mass, $M_{\text{atm}} = M_c$. Both the time to reach a fixed atmosphere mass and the runaway growth time are shorter for larger cores. For larger M_c , runaway growth commences at higher M_{atm}/M_c values.

2.5.1.1 EFFECTS OF CORE MASS

Figure 2.6 shows the growth of atmospheric mass with time for several core masses at 10 AU in our fiducial disk. Atmospheres grow faster around more massive cores due to stronger gravitational binding. The endpoint of each curve marks t_{run} . Runaway growth occurs near the crossover mass, when $M_{\text{atm}} \sim M_{\text{c}}$, in agreement with previous studies. Lower core masses undergo runaway accretion at fractionally smaller atmosphere masses.

Figure 2.7 shows how t_{run} varies with core mass, also at 10 AU. The numerical results are plotted against our non-self-gravitating analytic model, described in §2.3. The analytic model reproduces the general decline in t_{run} with core mass. The numerical model, which includes self-gravity, has a somewhat steeper mass dependence. A modest correction due to self-gravity is unsurprising, and consistent with the above-mentioned trend in $M_{\text{atm}}/M_{\text{c}}$ ratios. Moreover, in the analytic theory, crucial quantities like M_{atm} and L (both roughly $\propto M_{\text{c}}^3$ near crossover) have non-linear dependence on core mass, offering plenty of opportunity for self-gravitational corrections.

The effect of mean molecular weight is also shown in Figure 2.7. A lower μ gives longer growth times, because more cooling is required to compress the atmosphere. This effect is both well established in core accretion studies (Stevenson 1982) and intuitive since the atmospheric scale height $\propto 1/\mu$ is more extended for lower μ . Moreover, the Bondi radius decreases as $R_{\text{B}} \propto \mu$, giving a smaller gravitational sphere of influence (and a weaker compression at R_{H} when that is the more relevant scale). To see how this affects cooling times, note that the characteristic RCB depth near runaway scales as $P_{\text{RCB}} \sim P_{\text{M}} \propto \mu^{-4}$ from Equation (2.28). Thus $L \propto 1/P_{\text{RCB}} \propto \mu^4$ explains the trend of slower cooling for lower μ .

For $\mu = 2.0$, which represents the idealized case of an H_2 atmosphere completely devoid of Helium, t_{run} increases by factors of $\sim 2-3$. Thus fairly drastic changes in atmospheric composition are required for μ to significantly affect core accretion timescales. In principle, changes in the mean

molecular weight of the gas also affect the EOS, including ∇_{ad} , but such effects are not considered here (see §2.6.3).

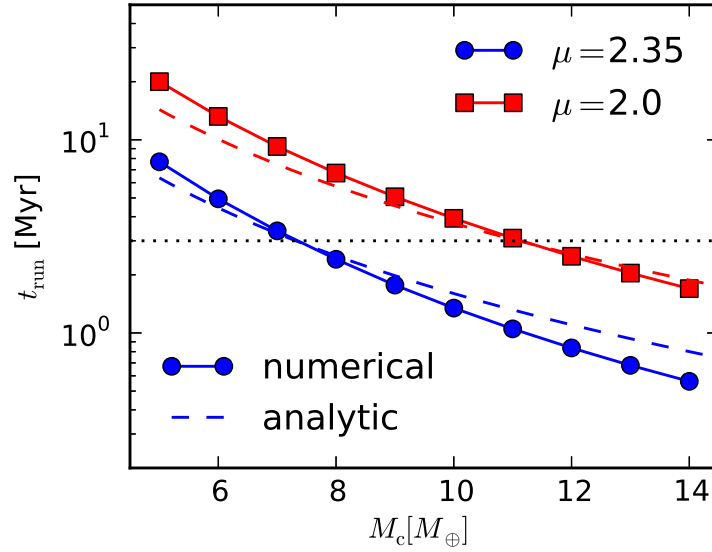


Figure 2.7: Runaway growth time, t_{run} , vs. core mass at 10 AU, for two values of the mean molecular weight. Our numerical model (*solid curves*) is compared to our non-self-gravitating analytic model (*dashed curves*, from Equation 2.37a). A typical protoplanetary disk life time of 3 Myr is plotted for comparison. The runaway growth time is larger for a lower mean molecular weight.

2.5.1.2 EFFECTS OF DISK TEMPERATURE AND PRESSURE

Figure 2.8 shows how the runaway accretion time varies with disk temperature, T_d , or pressure, P_d , holding the other quantity fixed. The analytic model roughly reproduces the temperature and pressure scalings, again with some discrepancies due mainly to the neglect of self-gravity. Temperature variations are much more significant than pressure variations (note the difference in logarithmic and linear axes). Since midplane disk conditions depend only on temperature and pressure in our model,[‡] the dominant effect of disk location is temperature.

[‡]See Equation (2.1). When gap opening is considered in models of later growth stages, the orbital frequency and effective viscosity become relevant as well.

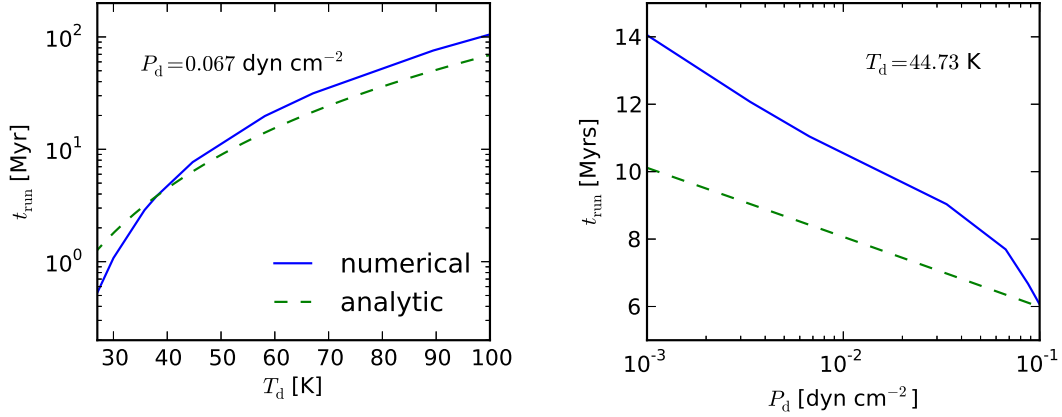


Figure 2.8: Runaway growth time as a function of disk temperature (*left*) and pressure (*right*) around a $M_c = 5M_\oplus$ core. The disk pressure or temperature (*left* or *right*, respectively) are fixed at values for 10 AU in our disk model. The analytic scalings given by Equation (2.37a) are plotted for comparison, as described in the text. Gas accretion slows down significantly at higher temperatures, but only speeds up modestly as the disk pressure or density increase.

The decline in growth times with lower temperatures arises from a balance of competing effects. The cooling luminosity is inherently smaller at lower temperatures. Overpowering this effect, the larger Bondi radius and lower dust opacity act to accelerate growth at lower temperatures.

Growth times depend only weakly on, but do fall slightly with, pressure. This result may be surprising, given that the disk is the source of atmospheric mass and the atmosphere must match onto the disk’s density and pressure. The nearly exponential increase in pressure with depth through the radiative zone explains this effect. Cooling is largely regulated at the RCB, and a modest change in RCB depth compensates for large variations in disk pressure.

Section 2.3 shows how these temperature and pressure effects arise in our analytic model.

2.5.2 CRITICAL CORE MASS

The critical core mass declines with distance from the star, as shown in Figure 2.9 for our standard disk model. The main reason for the decline, as explained above, is that atmospheres grow faster at lower temperatures. The lower densities and pressures in the outer disk have a much smaller effect.

Since the vast majority of disk models have a disk temperature that declines with a , our qualitative result is robust. We also show that higher μ values give lower values of M_{crit} .

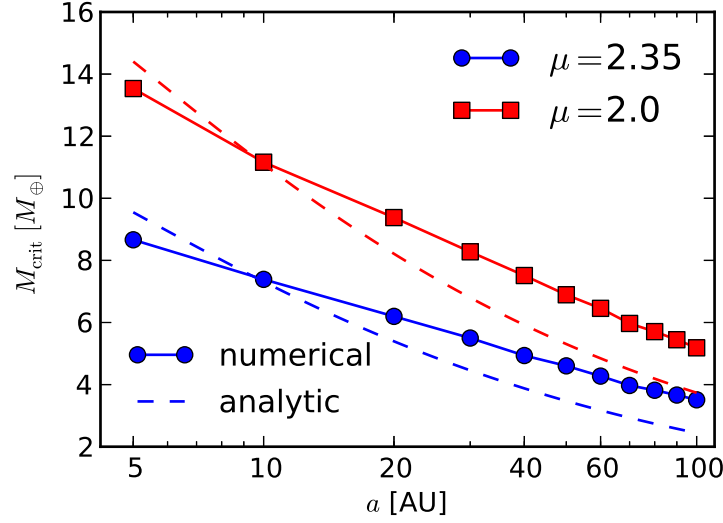


Figure 2.9: The critical core mass as a function of semimajor axis, for a disk lifetime of 3 Myrs and two values of the mean molecular weight ($\mu = 2.35$ is for Solar abundances). The decline in M_{crit} with distance is a robust result for standard disk models. The analytic model, which neglects self-gravity, over-predicts the steepness of the decline.

The average power-law decline from 1 to 100 AU (not plotted) is $M_{\text{crit}} \propto a^{-0.3}$, for both choices of μ . While not a drastic decline, the ability of distant low mass cores to accrete gas efficiently is significant for the interpretation of direct imaging surveys. However, our model offers no guarantee of copious giant planets at large distances. Many histories of solid accretion are possible, and solid cores may grow too slowly to allow the rapid gas accretion that we model.

Our non-self-gravitating analytic model (dashed curves in Figure 2.9) over-predicts the steepness of the decline in M_{crit} with a . This discrepancy is not surprising, as we have shown that self-gravity strongly affects evolution, even before runaway growth begins and the crossover mass is reached.

Figure 2.10 shows that reducing the opacity by an order of magnitude significantly reduces M_{crit} . Furthermore, this opacity effect is stronger at larger distances. The opacity reduction by a factor of

10 lowers M_{crit} at 5 AU by a factor of ~ 2.5 and at 100 AU by a factor of ~ 3.5 . Atmospheric opacity is a dominant uncertainty in core accretion modeling. However, unless atmospheric opacity varies significantly with disk radius, the general decline in M_{crit} with increasing a should hold. For our scenario of negligible ongoing planetesimal accretion, it is tempting to think that dust could settle out of the radiative zone, lowering the opacity (Podolak 2003). Nonetheless, since opacity near the RCB is a crucial factor, we speculate that convective overshoot may prevent very low opacities.

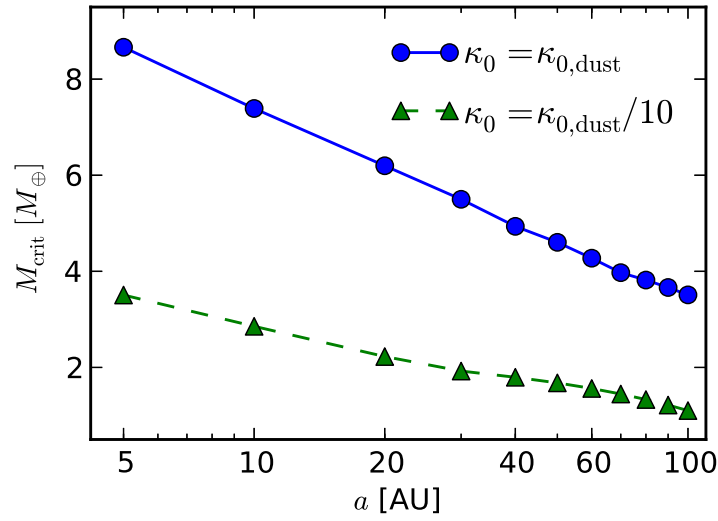


Figure 2.10: Critical core masses vs. distance for standard and reduced (by a factor of ten) dust opacities. Lower opacities give significantly lower M_{crit} values. Atmospheric opacity remains a large uncertainty in core accretion models.

A larger disk lifetime further reduces M_{crit} . Recent studies have shown that gas disks may live up to $\sim 10 - 12$ Myr (Bell et al. 2013). As $M_{\text{crit}} \sim t_{\text{d}}^{-3/5}$ (cf. Equation 2.34), a disk lifetime of 10 Myrs decreases the critical core mass by a factor of two. Of course, some fraction of the disk lifetime must be allocated to the growth and possibly migration of the core.

2.5.3 COMPARISON WITH PREVIOUS STUDIES

We can directly compare our results with other studies of protoplanetary atmospheric growth in the absence of planetesimal accretion, notably those in Ioo and PNo5. A major distinguishing feature of our study is that we explore a range of disk conditions, while Ioo and PNo5 focus on growth at the location of Jupiter, 5.2 AU, in their disk models. Moreover, both Ioo and PNo5 solve the full time dependent energy equation and consider more detailed EOSs, in addition to other detailed differences in model parameters. Despite these differences, the qualitative and quantitative agreement with our study is good.

Ioo give an approximate analytic fit to their models' envelope formation time (the equivalent of the runaway accretion time t_{run} in our models), at $a = 5.2$ AU,

$$\tau_{\text{env}} \sim 3 \times 10^8 \left(\frac{M_c}{M_{\oplus}} \right)^{-2.5} \left(\frac{\kappa}{1 \text{cm}^2 \text{s}^{-1}} \right) \text{ yr}. \quad (2.38)$$

Our model reproduces the linear opacity dependence (see §2.4.2), even though we use a temperature dependent opacity, Equation (2.5), instead of a constant κ . Our growth times at 5 AU,

$$t_{\text{run}} \sim 5 \times 10^8 \left(\frac{M_c}{M_{\oplus}} \right)^{-2.4} \text{ yr}, \quad (2.39)$$

agree well with the Ioo results, both in magnitude and scaling with core mass.

One goal of our study was to explain the extended luminosity minimum in evolutionary models that characterizes phase 2 in core accretion models, as described in the introduction. Previous work (see Figure 2 in Ioo and Figures 3 and 4 in PNo5) shows that this luminosity minimum is an intrinsic feature of atmospheric cooling even in the absence of planetesimal accretion. We not only reproduce this effect in our simplified model (see Figs. 2.2 and 2.3), but we also show that self-gravity is the essential ingredient to produce a broad luminosity minimum well before the crossover mass.

Time-dependent studies that incorporate planetesimal accretion generally find larger formation timescales and critical core masses than those of this work. This result is expected since additional energy from planetesimal accretion limits the ability of the atmosphere to cool. [Pollack et al. \(1996\)](#) find an evolutionary time and crossover mass of ~ 7.5 Myrs and $\sim 16 M_{\oplus}$, respectively, for a MMSN disk model at 5.2 AU and interstellar grain opacity. These values, however, decrease to ~ 3 Myrs and $\sim 12 M_{\oplus}$ if planetesimal accretion is entirely shut off during the gas accretion phase. The core accretion model of [Hubickyj et al. \(2005\)](#) for Jupiter’s formation predicts an evolutionary time of 3.3 Myrs for a $10 M_{\oplus}$ core, for an interstellar opacity, which is also consistent with our result at 5 AU.

A direct comparison with studies that only include planetesimal accretion, and neglect atmospheric cooling, is difficult. Note, however, that Ioo establishes the correspondence between the minimum luminosity in evolutionary models and the minimum planetesimal accretion rate needed in static models, which gives rise to the classical critical core mass of static models ([Mizuno et al. 1978](#); [Stevenson 1982](#)).

In terms of modern static studies, our results complement (and borrow some tools from) [Ro6](#) and [Rafikov \(2011\)](#). These studies consider the disk radius dependence of core accretion for protoplanets that continuously accrete planetesimals. We show that the limits on core accretion at large radial distance claimed by [Rafikov \(2011\)](#) (and references therein) can be overcome if planetesimal accretion shuts off and the atmosphere is allowed to cool. Nevertheless, the plausibility of rapid core growth followed by negligible subsequent solid accretion admittedly remains uncertain, as discussed in more detail in §2.7.

2.6 NEGLECTED EFFECTS

Since one goal of this paper was to obtain a detailed understanding of atmospheric evolution with a simple model, we have necessarily ignored effects of potential significance. We briefly address the most important of these and note that a followup work, [Piso, Youdin & Murray-Clay \(in prep.,](#)

hereafter Paper II), will extend our current models to address some of these effects.

2.6.1 HYDRODYNAMIC EFFECTS

The neglect of hydrodynamical effects in our model is best discussed in terms of the thermal mass, M_{th} , and the length scales introduced in §2.2.2. In the low mass regime, $M_{\text{p}} < M_{\text{th}}/\sqrt{3}$, where $R_{\text{B}} < R_{\text{H}}$, we assume that hydrostatic balance holds out to the outer boundary at R_{H} . In this low mass regime, [Ormel \(2013\)](#) calculated the 2D (radial and azimuthal) flow patterns driven by stellar tides and disk headwinds. On scales $\gtrsim R_{\text{B}}$ the flows no longer circulate the planet: they belong to the disk. While the density structure still appears roughly spherical and hydrostatic, these flows could affect the planet’s cooling. We expect such effects to be weak, as heat losses at greater depths dominate planetary cooling, but more study is needed, especially in 3D.

At higher masses, non-hydrostatic effects become more severe. At $M_{\text{p}} \gtrsim M_{\text{th}}$ planets can open significant gaps ([Zhu et al. 2013](#)). At yet higher masses accretion instabilities could occur ([Ayliffe & Bate 2012](#)). However, in this high mass regime, the spherically symmetric approximation has already broken down.

Thus by restricting our attention to low masses, neglected hydrodynamic effects should be minor. Moreover, since $M_{\text{th}} \propto a^{6/7}$ increases with disk radius, spherical hydrostatic models like ours have a greater range of applicability in the outer regions of disks.

2.6.2 REALISTIC OPACITIES

The importance of envelope opacity is an established factor in core accretion calculations (e.g., [Stevenson 1982](#), [Ikoma et al. 2000](#), [Ro6](#)), and several studies explore the influence of opacity on the timescales for giant planet formation in detail (e.g., [Hubickyj et al. 2005](#)). Treating dust (and total) opacities as a power law in temperature is a simplification. Opacities drop by order unity when ice grains sublime for $T \gtrsim 150$ K and they drop by orders of magnitude when silicate grains evapo-

rate above $T \gtrsim 1500$ K (Semenov et al. 2003; Ferguson et al. 2005). Grain growth and composition also affect opacities. Our scenario of no ongoing accretion of solids may result in a grain-free atmosphere, which could substantially reduce the critical core mass ($\sim 1 M_{\oplus}$ in the case of Jupiter, Hori & Ikoma 2010). Paper II explores more realistic opacity laws.

For this work, we justify a simplified dust opacity by the cool temperatures of both the outer disk and our nearly isothermal radiative zones (see §2.4.1). While convective interiors get significantly hotter than 1500 K, opacity does not affect the structure of adiabatic convecting regions. A possible caveat is the existence of radiative zones sandwiched inside the convection interior. Such “radiative windows” arise if the opacity drop from ice and metal grain sublimation occurs at sufficiently low pressures. Our two-layer model ignores this possibility, but radiative windows are known to exist in hot Jupiter models (Burrows et al. 1997; Arras & Bildsten 2006) and have been seen in some core accretion models (Lissauer, personal communication). The role of radiative windows in core accretion models remains to be explored in detail.

2.6.3 EQUATION OF STATE

Our model uses an ideal gas law and a polytropic EOS, given by Equation (2.13). However, non-ideal effects can affect atmospheric structure and evolution. In the lower atmosphere, H_2 can partially dissociate at high temperatures. In the upper atmosphere, H_2 rotational levels can become depopulated at lower temperatures. Paper II uses the Saumon et al. (1995) EOS, with extensions to lower pressures and temperatures as needed, to explore these effects.

2.6.4 CORE GROWTH

Our model purposefully neglects the accretion of solids to study the fastest rates of gas accretion. Our M_{crit} values thus differ from the M_{crit} values in static models, such as Ro6. For similar parameters, we generally obtain lower M_{crit} values than Ro6 because our atmospheres are not heated by

ongoing planetesimal accretion. Paper II presents a quantitative comparison.

At low planetesimal accretion rates, \dot{M}_c , a static model could formally give lower M_{crit} values than our evolutionary calculations. Ro6 shows that $M_{\text{crit}} \propto \dot{M}_c^{3/5}$ in static models. The underlying assumption of static models, a negligibly short KH contraction time, fails whenever static models give a lower M_{crit} . Thus our results give a firm lower limit on M_{crit} which complement the results of static models with planetesimal accretion.

2.7 SUMMARY

We study the formation of giant planets by the core accretion mechanism. Our models start with a solid core that is embedded in a gas disk and no longer accreting solids. We determine – as a function of disk location, core mass, and the atmosphere’s mean molecular weight and opacity – whether runaway atmospheric growth can occur within a typical disk lifetime of 3 Myr. By neglecting the accretion luminosity of planetesimals and smaller solids, we obtain the fastest allowed rate of gas accretion.

We address core accretion in the outer disk, as it is relevant to direct imaging surveys. Our model approximations, including spherical accretion and low mass radiative exteriors with opacities dominated by dust, are tuned to conditions in the outer disk. Our main findings are as follows:

1. The minimum or critical core mass, M_{crit} , for giant planet formation declines with stellocentric distance in standard protoplanetary disk models. For our reference case, the critical mass is $\sim 8.5 M_{\oplus}$ at $a = 5$ AU, decreasing to $\sim 3.5 M_{\oplus}$ at $a = 100$ AU. This decline roughly follows $M_{\text{crit}} \propto a^{-0.3}$.
2. The drop in disk temperature with radial distance explains the decrease in critical core masses. The lower pressures and densities in the outer disk only weakly suppress atmospheric growth.

3. Reducing dust opacities by a factor of 10 reduces critical core masses by a factor of ~ 3 . This reduction is somewhat stronger (weaker) at larger (smaller) separations from the star.
4. A larger mean molecular weight reduces critical core masses, in agreement with Hori & Ikoma (2011). If enrichment in heavy elements correlates with increased dust opacity, then the stronger opacity effect will dominate, increasing M_{crit} .
5. Runaway growth begins roughly at the crossover mass, when atmosphere and core masses are equal, $M_{\text{atm}} \sim M_{\text{c}}$, in agreement with previous work (Pollack et al. 1996). Further from the star, runaway growth begins at smaller $M_{\text{atm}}/M_{\text{c}}$ ratios. For larger core masses, runaway growth begins at larger values of $M_{\text{atm}}/M_{\text{c}}$.
6. Self-gravity affects atmospheric evolution before crossover. Significant self-gravitational corrections appear when the atmosphere is only $\sim 10\%$ as massive as the core.

Rapid gas accretion onto low mass cores could explain the origin of distant directly imaged giant planets (Marois et al. 2008; Lagrange et al. 2010). However, our model does not address the details of how solid cores grow, as many possibilities exist and many uncertainties remain. For a giant planet to form with a core near the minimum masses we derive, core growth must first be rapid and then slow significantly, as in phases 1 and 2, respectively, of Pollack et al. (1996).

Initial core growth must be fast, compared to the disk lifetime, to get a sufficiently massive core. Such rapid core growth is possible in a variety of scenarios, including the fastest gas-free planetesimal accretion rates (Dones & Tremaine 1993) and – probably more relevantly for gas rich disks – the aerodynamic accretion of mm-m sized “pebbles” and “boulders” in gas disks (Ormel & Klahr 2010; Lambrechts & Johansen 2012). Moreover, cores could form rapidly closer to the star, then migrate or be scattered outwards by already formed giants (Ida et al. 2013).

A stronger constraint is that core growth subsequently slow severely, to allow the atmosphere to cool and contract. To be more quantitative, the minimum cooling luminosity in Figure 2.2,

$L \approx 3.5 \times 10^{24} \text{ ergs}^{-1}$, could be cancelled by low levels of heating from solid accretion. A core mass doubling timescale of $\sim 400 \text{ Myr}$, or faster, would thus provide enough heating to stall atmospheric cooling and growth. An additional concern is that isolation masses tend to grow with disk radius, as $M_{\text{iso}} \propto \Sigma_{\text{p}}^{3/2} a^2 \propto a^{3/4}$ under the approximation that the surface density of accreted planetesimals (Σ_{p}) scales with the gas (Youdin & Kenyon 2013). While this behavior is nominally inconsistent with final core masses that decline with distance, the predictive power of the isolation mass is imperfect. For starters, the efficiency of planetesimal formation remains uncertain. Moreover, the locality of core growth, which underlies the isolation mass, disappears when accreted solids drift and/or cores migrate significantly.

Thus while our calculations show that low mass cores can grow into gas giants in the outer disk, ongoing solid accretion could prevent significant atmospheric growth. In the Solar System, the ice giants Uranus and Neptune, with core (here ice and rock) masses of $\sim 13\text{--}15 M_{\oplus}$, argue for the latter possibility. Ongoing exoplanet imaging surveys and their successors (Hinz et al. 2012; Macintosh et al. 2012; Close et al. 2014) will help discriminate among the various planet formation pathways in the outskirts of protoplanetary disks.

3

Minimum Core Masses for Giant Planet Formation With Realistic Equations of State and Opacities

ABSTRACT

Giant planet formation by core accretion requires a core that is sufficiently massive to trigger runaway gas accretion in less than the typical lifetime of protoplanetary disks. We explore how the minimum required core mass, M_{crit} , depends on a non-ideal equation of state and on opacity changes due to grain growth, across a range of stellocentric distances from 5-100 AU. This minimum M_{crit}

applies when planetesimal accretion does not substantially heat the atmosphere. Compared to an ideal gas polytrope, the inclusion of molecular hydrogen (H_2) dissociation and variable occupation of H_2 rotational states increases M_{crit} . Specifically, M_{crit} increases by a factor of ~ 2 if the H_2 spin isomers, ortho- and parahydrogen, are in thermal equilibrium, and by a factor of $\sim 2 - 4$ if the ortho-to-para ratio is fixed at 3:1. Lower opacities due to grain growth reduce M_{crit} . For a standard disk model around a Solar mass star, we calculate $M_{\text{crit}} \sim 8M_{\oplus}$ at 5 AU, decreasing to $\sim 5M_{\oplus}$ at 100 AU, for a realistic EOS with an equilibrium ortho-to-para ratio and for grain growth to cm-sizes. If grain coagulation is taken into account, M_{crit} may further reduce by up to one order of magnitude. These results for the minimum critical core mass are useful for the interpretation of surveys that find exoplanets at a range of orbital distances.

The contents of this chapter are published in *Piso, A.-M. A., Youdin, A. N., & Murray-Clay, R. A. 2015, ApJ, 800, 82*

3.1 INTRODUCTION

Core accretion — a prominent theory of giant planet formation — stipulates that Jupiter-sized planets form when planetesimal accretion produces a solid core large enough to attract a massive atmosphere (e.g., [Mizuno et al. 1978](#), [Stevenson 1982](#), [Bodenheimer & Pollack 1986](#), [Wuchterl 1993](#), [D’Angelo et al. 2011](#)). Because protoplanetary disks dissipate on timescales of a few Myrs (e.g., [Jayawardhana et al. 1999](#)), cores must grow quickly to accrete disk gas. Fast growth is particularly challenging far from a core’s host star, where dynamical times are long. Understanding whether core accretion can work in the outer disk may provide valuable insights into the formation of wide-separation planets such as the directly-imaged giants orbiting HR 8799 ([Marois et al. 2008](#)).

Production of such planets *in situ* by core accretion requires faster core growth rates than typically assumed. However, even if fast growth could be achieved, it produces an additional difficulty. Though the minimum, or critical, core mass to form a giant planet is often quoted as $M_{\text{crit}} \sim$

$10M_{\oplus}$, the actual value depends on how quickly the core accretes planetesimals (e.g., Pollack et al. 1996, Ikoma et al. 2000, Rafikov 2006). Fast accretion heats a core’s atmosphere, increasing pressure support and hence M_{crit} . Rafikov (2011) finds that beyond 40–50 AU, a core cannot reach M_{crit} while accreting at the rate it requires to grow during its host disk’s lifetime.

This limit on the distance at which core accretion operates may be overcome if core growth does not proceed at a constant rate. Time-dependent models (e.g., Pollack et al. 1996; Ikoma et al. 2000) suggest that a planet’s feeding zone may be depleted of planetesimals before disk dissipation, causing core growth to stall. Planetesimal accretion no longer deposits energy into the atmosphere which, without this balance for radiative losses, cannot maintain a steady state. The envelope accretes gas while undergoing Kelvin-Helmholtz (KH) contraction. In this regime, a core of any mass would evolve into a giant planet if given an infinite amount of time. In practice, a core produces a giant planet if it has enough time to accumulate an atmosphere of approximately its own mass before its host disk dissipates. The minimum core mass satisfying this criterion is M_{crit} .

Because extra heating increases an atmosphere’s pressure, opposing runaway envelope growth, M_{crit} is smallest in the absence of planetesimal accretion. While M_{crit} has been systematically computed as a function of disk properties and stellocentric separation for steady-state atmospheres heated by planetesimal accretion (Rafikov 2006), no equivalent systematic study is available for this minimum value of M_{crit} .

In Piso & Youdin (2014, hereafter Paper I) and this paper, we provide such a systematic study. Given a fiducial disk model, we calculate the M_{crit} required to nucleate runaway atmospheric growth for a fully formed—and no longer accreting—core. We model the planet’s evolution using a series of quasi-static two-layer atmospheres embedded in a protoplanetary disk. Here, we build on the results of Paper I by making two important additions: (1) a realistic equation of state (EOS), and (2) realistic dust opacities. Our aim is twofold: (1) to explain how hydrogen and helium’s non-ideal EOS affects atmospheric growth when compared to an ideal gas, and (2) to provide realistic estimates for

the minimum critical core mass required to form a giant planet over a range of semimajor axes.

3.1.1 EQUATION OF STATE

We use the EOS of hydrogen and helium mixtures calculated by [Saumon et al. \(1995\)](#), which captures non-ideal effects such as dissociation, ionization, and selective occupation of quantum states at low temperatures. We extend these tables to the very low temperatures and pressures required for planets forming in the outer regions of disks (Appendix C). The EOS tables from [Saumon et al. \(1995\)](#) have often been used to model the interiors of giant planets (e.g., [Pollack et al. 1996](#), [Ikoma et al. 2000](#), [Alibert et al. 2005](#), [Hubickyj et al. 2005](#), [Papaloizou & Nelson 2005](#), [Mordasini et al. 2012](#)), as well as in complex stellar evolution simulations involving low temperatures (e.g., [Paxton et al. 2011](#), [Paxton et al. 2013](#), which use the code MESA). More recent EOS tables ([Nettelmann et al. 2008](#), [Nettelmann et al. 2012](#), [Militzer & Hubbard 2013](#)) are based on ab initio molecular dynamics simulations and thus avoid some of the approximations of the [Saumon et al. \(1995\)](#) semi-analytical approach. However, though these newer tables are sufficient to model the internal structures of Jupiter and of close-in extrasolar planets, they do not extend to the low temperatures and pressures required for wide-separation planets ($T \lesssim 500$ K, $P \lesssim 1$ GPa, e.g. [Militzer & Hubbard 2013](#)). Moreover, the [Militzer & Hubbard \(2013\)](#) EOS tables and the [Saumon et al. \(1995\)](#) tables are in good agreement for entropies, S , such that $\log_{10}(S) \gtrsim 8.75 \text{ erg g}^{-1} \text{ K}^{-1}$. All models presented here satisfy this constraint.

3.1.2 OPACITY

Opacities in protoplanetary disks are unlikely to be interstellar, and are lowered by grain growth and dust settling. Numerous studies have demonstrated that atmospheric evolution depends strongly on opacity—lower opacities accelerate envelope growth and reduce M_{crit} . For example, the analytic model of [Stevenson \(1982\)](#) showed that $M_{\text{crit}} \propto \kappa^{3/4}$ for a fully radiative envelope with constant

opacity κ . A series of more modern studies conclude that: Jupiter may have formed in 1 Myr with a core of $10M_{\oplus}$ for an opacity arbitrarily reduced to 2% of the interstellar value (Hubickyj et al. 2005); M_{crit} for Jupiter may be as low as $\sim 1M_{\oplus}$ for a grain free envelope (Hori & Ikoma 2010); and the use of grain opacities that take into account coagulation and settling reduces the formation time for Jupiter by up to 80% (Movshovitz et al. 2010). A recent study by Mordasini et al. (2014) investigates the effect of opacity on the formation of populations of synthetic planets, and finds from comparisons with observations that opacities are likely to be much smaller than interstellar. Lastly, Paper I shows that reducing the opacity from interstellar to 1% of interstellar reduces M_{crit} by a factor of ~ 2 .

Thus, to provide realistic estimates for M_{crit} , we must employ realistic opacities. For temperatures below dust sublimation, we employ opacity tables from D’Alessio et al. (2001), which are used to model observations of protoplanetary disks. We present results for both a standard collisional cascade grain size distribution and for a shallower distribution, appropriate for coagulation (see Section 3.5 for details). At high temperatures, where dust sublimates, we employ the analytic opacity law of Bell & Lin (1994). For our purposes, this expression sufficiently represents the more detailed opacity tables of Semenov et al. (2003) with reduced computational complexity (see Appendix E). We note that most previous works that study the quantitative effects of opacity reductions on M_{crit} are primarily focused on the formation of Jupiter at 5.2 AU. In contrast, our aim is to provide realistic estimates for M_{crit} for a larger parameter space, and to analyze the dependence of M_{crit} on semimajor axis.

3.1.3 PAPER PLAN

After reviewing the quasi-static and cooling models derived in Paper I (Section 3.2), we add a non-ideal EOS. Because the adiabatic gradient, ∇_{ad} , is an important determinant of atmospheric structure, we first explain how dissociation and variable occupation of low-energy rotational states change

∇_{ad} (Section 3.3). Section 3.4 presents the impact of these effects on atmosphere evolution. We introduce realistic opacities in Section 3.5 and determine M_{crit} in Section 3.6. Section 3.7 compares our results to those obtained by studies employing high planetesimal accretion rates. We summarize our findings in Section 3.8.

3.2 ATMOSPHERIC MODEL REVIEW

We begin with a brief review of Paper I’s model for the structure and evolution of a planetary atmosphere embedded in a protoplanetary disk. We summarize assumptions of the model and properties of our assumed disk in §3.2.1 and list expressions for the atmosphere’s structure and time evolution in §3.2.2.

3.2.1 ASSUMPTIONS AND DISK MODEL

We assume that the planet consists of a solid core of fixed mass and a two-layer atmosphere composed of an inner convective region and an outer radiative zone that matches smoothly onto the disk. The two regions are separated by the Schwarzschild criterion for convective instability (see §3.2.2) at radius $r = R_{\text{RCB}}$, known as the radiative-convective boundary (RCB). We assume that the luminosity is constant throughout the radiative region (see Section §3.6 for additional discussion). Note that a similar method is used by [Papaloizou & Nelson \(2005\)](#) and [Mordasini et al. \(2012\)](#), who find that it agrees with more complex models.

Our model applies when planetesimal accretion is minimal, so that the envelope’s evolution is dominated by KH contraction (see §3.7 for a discussion of the physical conditions required for a core to be in this regime). The atmosphere is spherically symmetric, self-gravitating and in hydrostatic balance. We apply our model at semimajor axes $a \gtrsim 5$ AU. Here the disk scale height is larger than the radius at which the planet matches onto the disk (see Paper I for further details), and hence spherical symmetry holds. The nebular gas is composed of a hydrogen-helium mixture, with hydro-

gen and helium mass fractions of 0.7 and 0.3, respectively. Because the envelope grows slowly, we calculate its evolution using a series of linked quasi-static equilibrium models.

The temperature and pressure at the outer boundary of the atmosphere are given by the nebular temperature and pressure. We use the minimum mass, passively irradiated disk model of [Chiang & Youdin \(2010\)](#). The surface density, mid-plane temperature and mid-plane pressure are

$$\Sigma_d = 2200 (a/\text{AU})^{-3/2} \text{ g cm}^{-2} \quad (3.1a)$$

$$T_d = 120 (a/\text{AU})^{-3/7} \text{ K} \quad (3.1b)$$

$$P_d = 11 (a/\text{AU})^{-45/14} \text{ dyn cm}^{-2}, \quad (3.1c)$$

for a mean molecular weight $\mu = 2.35$.

3.2.2 STRUCTURE EQUATIONS AND COOLING MODEL

The structure of a static atmosphere is described by the standard equations of hydrostatic balance and thermal equilibrium:

$$\frac{dP}{dr} = -\frac{Gm}{r^2} \rho \quad (3.2a)$$

$$\frac{dm}{dr} = 4\pi r^2 \rho \quad (3.2b)$$

$$\frac{dT}{dr} = \nabla \frac{T}{P} \frac{dP}{dr} \quad (3.2c)$$

$$\frac{dL}{dr} = 4\pi r^2 \rho (\epsilon + \epsilon_g), \quad (3.2d)$$

where r is the radial coordinate, P , T and ρ are the gas pressure, temperature, and density, respectively, m is the mass enclosed by radius r , L is the luminosity from the surface of radius r , and G is

the gravitational constant. The gas is heated at a rate $\epsilon_g \equiv -T dS/dt$ per unit mass due to gravitational contraction, where S is the specific gas entropy, while ϵ represents the rate at which internal heat is generated per unit mass. We do not take into account any internal energy sources and set $\epsilon = 0$. The temperature gradient $\nabla \equiv d \ln T / d \ln P$ depends on whether energy is transported throughout the atmosphere by radiation or convection. In the case of radiative diffusion for an optically thick gas, the temperature gradient is

$$\nabla = \nabla_{\text{rad}} \equiv \frac{3\kappa P}{64\pi G m \sigma T^4} L, \quad (3.3)$$

where σ is the Stefan-Boltzmann constant and κ is the dust opacity. In our models the atmosphere is optically thick throughout the outer boundary. Where energy is transported by convection, the temperature gradient is

$$\nabla = \nabla_{\text{ad}} \equiv \left(\frac{d \ln T}{d \ln P} \right)_{\text{ad}}, \quad (3.4)$$

with ∇_{ad} the adiabatic temperature gradient. The convective and radiative layers of the envelope are separated by the Schwarzschild criterion (e.g., [Thompson 2006](#)): the atmosphere is stable against convection when $\nabla < \nabla_{\text{ad}}$ and convectively unstable when $\nabla > \nabla_{\text{ad}}$. Since convective energy transport is highly efficient, $\nabla \approx \nabla_{\text{ad}}$ in convecting regions. The temperature gradient is thus given by $\nabla = \min(\nabla_{\text{ad}}, \nabla_{\text{rad}})$.

Equation set (3.2) is supplemented by an equation of state (EOS) relating pressure, temperature and density, as well as an opacity law. As summarized in Sections 3.1.1 and 3.1.2, this paper improves on the ideal gas polytropic EOS and interstellar medium dust opacity employed in Paper I. We discuss the impact of our choices in Sections 3.3, 3.4, and 3.5.

We assume that the atmosphere forms around a solid core of fixed mass M_c with a radius $R_c = (3M_c/4\pi\rho_c)^{1/3}$, where ρ_c is the core density. We choose $\rho_c = 3.2 \text{ g cm}^{-3}$ (e.g., [Papaloizou &](#)

Terquem 1999). Two radial scales determine the extent of the atmosphere: the Hill radius, $R_H \equiv a[M_p/(3M_\odot)]^{1/3}$, where the gravitational attraction of the planet and the tidal gravity due to the host star are equal, and the Bondi radius, $R_B \equiv GM_p/c_s^2 = GM_p/(\mathcal{R}T_d)$, where the thermal energy of the nebular gas is approximately the gravitational energy of the planet. Here, M_p is the total planet mass, c_s is the isothermal sound speed, $\mathcal{R} = k_B/(\mu m_p)$ is the reduced gas constant, k_B is the Boltzmann constant, and m_p the proton mass. We define the planet mass as the mass enclosed inside the smaller of R_B or R_H . For $R_B < R_H$, several studies assume that the atmosphere matches onto the disk at R_B (e.g., Ikoma et al. 2000, Pollack et al. 1996). In all cases, we choose the Hill radius as our outer boundary because the temperature and pressure at R_H are those of the disk, $T(R_H) = T_d$ and $P(R_H) = P_d$ (see Paper I for more details). Outside R_B , gas flows no longer circulate the planet, but rather belong to the disk. However, when $R_B < R_H$, the density structure between R_B and R_H remains spherical and is still well described by hydrostatic balance (Ormel 2013).

Finally, we employ a cooling model developed in Paper I to determine the time evolution of the atmosphere between subsequent static models. A protoplanetary atmosphere embedded in a gas disk emits a total luminosity

$$L = L_c + \Gamma - \dot{E} + e_{\text{acc}}\dot{M} - P_M \frac{\partial V_M}{\partial t}. \quad (3.5)$$

Here, L_c is the luminosity from the solid core, which may include planetesimal accretion and radioactive decay, and Γ is the rate of internal heat generation. We set $L_c = \Gamma = 0$. The \dot{E} term is the rate at which total energy (internal and gravitational) is lost. Gas accretes at a rate $\dot{M}(r)$ with a specific energy $e(r) = u(r) - GM(r)/r$, where $u(r)$ is the internal energy per unit mass and $M(r)$ is the mass enclosed by radius r . To evaluate Equation 3.5, we choose a boundary radius $r = R$, so that $e_{\text{acc}} = e(R)$. Finally, the last term in Equation 3.5 represents the work done on a surface mass

element.

We obtain an evolutionary series for the atmosphere by connecting sets of subsequent static atmospheres through the cooling Equation (3.5). Details of our numerical procedure are described in Paper I. In contrast with Paper I, we evaluate Equation (3.5) at R_B rather than R_{RCB} . This ensures that our calculations are consistent, because realistic opacities introduce inner radiative windows in the atmospheric structure and thus multiple RCBs (see Section 3.5).

3.3 ADIABATIC GRADIENT FOR THE TABULATED EQUATION OF STATE

For our gas equation of state, we use the interpolated EOS tables of [Saumon et al. \(1995\)](#) for a helium mass fraction $Y = 0.3$, and extend them to lower temperatures and pressures corresponding to the conditions in our fiducial disk. Appendix C describes our extension procedure.

For ease of discussion, we choose to represent the EOS through the adiabatic gradient ∇_{ad} (defined in Equation 3.4). In contrast with an ideal gas polytrope, the EOS of a realistic gas cannot be fully specified by ∇_{ad} . The [Saumon et al. \(1995\)](#) EOS tables are obtained using free energy minimization (see, e.g., [Graboske et al. 1969](#)), which provides additional information about the relationship between the thermodynamic variables. Nevertheless, ∇_{ad} is a useful parameter for understanding atmospheric structure. For an ideal gas polytropic EOS, the adiabatic gradient is constant. Non-ideal effects such as dissociation or ionization produce temperature-dependent variations in ∇_{ad} . Figure 3.1 shows a contour plot of ∇_{ad} as a function of gas temperature and pressure. We distinguish three separate temperature regimes:

1. Intermediate temperature regime ($300 \text{ K} \lesssim T \lesssim 2000 \text{ K}$), where the hydrogen-helium mixture behaves like an ideal gas with a polytropic EOS.
2. High temperature regime ($T \gtrsim 2000 \text{ K}$), where dissociation of molecular hydrogen occurs, followed by ionization of atomic hydrogen for $T \gtrsim 10,000 \text{ K}$.

3. Low temperature regime ($T \lesssim 300$ K), where the rotational states of the hydrogen molecule are not fully excited.

We note that helium behaves like an ideal monatomic gas with $\nabla_{\text{ad}} = 2/5$ in our regime of interest. Its presence in the atmosphere thus only causes a small, constant upward shift in the adiabatic gradient of the mixture.

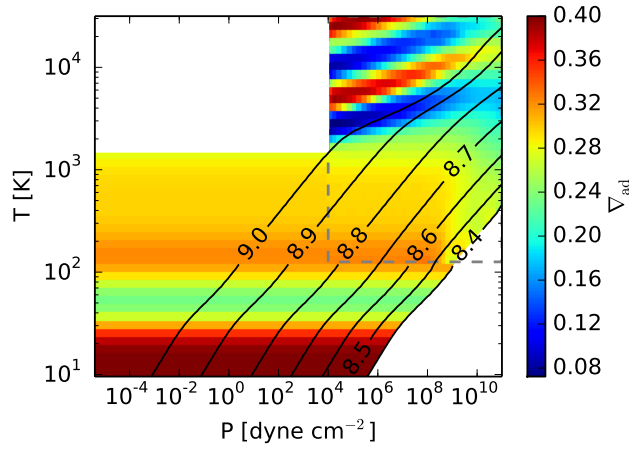


Figure 3.1: Contour plot of the adiabatic gradient ∇_{ad} for a hydrogen-helium mixture in thermodynamic equilibrium as a function of gas temperature and pressure. The upper-right rectangle encloses the region described by the original [Saumon et al. \(1995\)](#) EOS tables, while the rest of the plot is our extension. The black curves represent constant entropy adiabats, with the labels $\log_{10}(S)$ [erg K $^{-1}$ g $^{-1}$]. The regions in which the EOS is either invalid or not computed are masked in white. Further details about the masked regions can be found in Appendix C.0.5.

3.3.1 INTERMEDIATE T : IDEAL GAS

For $300 \text{ K} \lesssim T \lesssim 2000 \text{ K}$, the hydrogen molecule is not energetic enough to dissociate and hydrogen behaves as an ideal diatomic gas with constant ∇_{ad} (Figure 3.1). The monatomic helium component increases the adiabatic index slightly, so that $\nabla_{\text{ad}} \approx 0.3$ rather than $2/7$ for a pure diatomic gas.*

*Recall that for an ideal gas, $\nabla_{\text{ad}} \equiv \frac{\gamma-1}{\gamma}$, where the adiabatic index $\gamma = 7/5$ for a diatomic gas and $5/3$ for a monatomic gas.

3.3.2 HIGH T : DISSOCIATION AND IONIZATION OF HYDROGEN

Hydrogen is molecular at low temperatures, dissociates at $T \gtrsim 2000 - 3000$ K, and ionizes at $T \gtrsim 10,000$ K. In stellar and giant planet interiors there is little overlap between the two processes: hydrogen is almost entirely dissociated into atoms by the time ionization becomes important.

As displayed in Figure 3.1, the adiabatic gradient decreases significantly in regions of partial dissociation and partial ionization. This reduction occurs because dissociation and ionization act as energy sinks. When internal energy is input into a partially dissociated gas, a portion is used to break down molecules, reducing the amount available to increase the temperature of the system.

An expression for ∇_{ad} as a function of the dissociation fraction is presented in Appendix D.o.7. As expected, ∇_{ad} is $2/7$ for pure molecular hydrogen and $2/5$ when hydrogen is fully dissociated, but decreases significantly during partial dissociation and is smallest when half of the gas is dissociated. Note that this behavior differs from a mixture of molecular and atomic hydrogen, for which $2/7 < \nabla_{\text{ad}} < 2/5$.

3.3.3 LOW T : HYDROGEN ROTATION AND SPIN ISOMERS

The (diatomic) hydrogen molecule has five degrees of freedom, three associated with translational motion and two associated with rotation. At T well above the molecule's excitation temperature for rotation, $\Theta_r \approx 85$ K (Kittel et al. 1981), its rotational states are fully excited and its EOS is that of an ideal diatomic gas (Section 3.3.1). As $T \rightarrow 0$, rotation ceases entirely and $\nabla_{\text{ad}} \approx 2/5$, the value for an ideal monatomic gas. At temperatures comparable to Θ_r , the rotational states of H_2 are partially excited, and its EOS depends on the relative occupation of two isomeric forms, parahydrogen and orthohydrogen, distinguished by the spin symmetry of the molecule's two protons.

Because protons are fermions, the Pauli exclusion principle implies that the total wave function of H_2 must be antisymmetric with respect to proton exchange. Two components of the wave func-

tion may provide this asymmetry—proton spins and the molecule’s rotational state. Parahydrogen has antiparallel proton spins and thus can only occupy symmetric rotational states with even angular quantum number j (Farkas 1935). In contrast, orthohydrogen has parallel proton spins, and can only occupy states with odd j . In thermal equilibrium at $T \rightarrow 0$ all hydrogen molecules are in the ground state with $j = 0$, which corresponds to parahydrogen. As temperature increases, parahydrogen starts converting into orthohydrogen. Because the proton spin state is a triplet for orthohydrogen and a singlet for parahydrogen, this conversion plateaus at an ortho-para equilibrium ratio of 3:1 for $T \gtrsim 150$ K.

Spin conversion requires energy. In thermal equilibrium, a portion of any internal energy input at $20 \lesssim T \lesssim 150$ K is used to convert para- to orthohydrogen, reducing the amount available to increase T . As a result, ∇_{ad} declines (Figure 3.1; see Appendix D.0.8 for further discussion).

3.3.3.1 THERMODYNAMIC EQUILIBRIUM OF SPIN ISOMERS

We conduct the majority of our calculations using the thermal equilibrium EOS illustrated in Figure 3.1. For reference, we also include results for a fixed 3:1 ortho-para ratio (used, e.g., by D’Angelo & Bodenheimer 2013).[†]

Ortho- and parahydrogen remain in thermodynamic equilibrium if the isomers can interconvert on a timescale shorter than the atmosphere’s KH contraction time. In isolation, isomeric conversion requires a forbidden transition and has a timescale longer than the age of the universe (e.g., Pachucki & Komasa 2008). Fast conversion requires a magnetic catalyst to aid the transition between the triplet and singlet spin states.

In astrophysical contexts, this catalyst is typically provided by collisions with ions such as H^+ or

[†]When interconversion timescales are longer than the system evolution time, populations of the two isomers evolve independently, with a fixed abundance ratio. Even at low temperature, formation of H_2 on grains produces an ortho-para ratio of 3:1 since the formation energy 4.48 eV, equipartitioned into vibrational, rotational, and translational energy, yields a rotation temperature of 9200 K (e.g., Takahashi 2001; c.f. Fukutani & Sugimoto 2013). In the absence of thermal equilibrium, a fixed ratio of 3:1 is likely.

H_3^+ (e.g., [Lique et al. 2012, 2014](#)). At high densities, collisions with H_2 also contribute to conversion through interactions between the spin state and the magnetic dipole of the H_2 molecule ([Huestis 2008](#)).

For a core of mass M_{crit} , the KH contraction time during the slowest phase of growth is approximately the disk lifetime, $t_{\text{disk}} \sim 3 \times 10^6$ years. The thermodynamic equilibrium EOS is thus appropriate if the ortho-para equilibration time, t_{equil} is smaller than t_{disk} . To determine whether this condition is met throughout the outer atmosphere (where $T \lesssim 150$ K), we check t_{equil} at the RCB and in the disk.

For core masses $6\text{--}30 M_{\oplus}$, our models produce RCB densities in the range $n = 1.5\text{--}5 \times 10^{14}$ during the longest phase of atmospheric evolution. The integrated column through the atmosphere at the RCB is $\sim 10^{25} \text{ cm}^{-2}$, larger than the $\sim 10^{22}\text{--}10^{23} \text{ cm}^{-2}$ required to be optically thick to X-rays ([Glassgold et al. 1997](#)), so that ionizations in this interior portion of the atmosphere are attenuated. However, densities at the RCB are high enough that H_2 collisions cause substantial isomeric conversion. Extrapolating from calculations of catalysis by O_2 , [Conrath & Gierasch \(1984\)](#) estimate a rate coefficient for conversion of $k_{H_2} = 8 \times 10^{-29} (T/125\text{K})^{1/2} \text{ cm}^3 \text{ s}^{-1}$, marginally consistent with the production of non-equilibrium ortho-para ratios in solar system giants by upwellings and flows (e.g. [Fouchet et al. 2003](#)). [Huestis \(2008\)](#) estimates a faster rate coefficient given by $\log_{10} k_{H_2} [\text{cm}^3 \text{ s}^{-1}] = 10^{-28} [1.56 + 12.2 \exp(-173\text{K}/T)]$, consistent with laboratory experiments in liquid and gaseous H_2 ([Farkas 1935](#); [Milenko et al. 1997](#)). At $T = 50\text{K}$ (T in the radiative region only varies from the disk temperature by an order unity factor; see Section 3.4.2), the equilibration time is

$$t_{\text{equil}} = (k_{H_2} n_{H_2})^{-1} = 1.5\text{--}6 \times 10^6 \text{ yr} \left(\frac{n}{10^{14} \text{ cm}^{-3}} \right)^{-1}, \quad (3.6)$$

which is comparable to or shorter than t_{disk} .

Where the outer atmosphere matches conditions in the disk, we turn to calculations for pro-

toplanetary disks for guidance. [Boley et al. \(2007\)](#) estimate a minimum $t_{\text{equil}} \sim 300$ yr. Isomeric conversion primarily results from collisions between H_2 and ionic species, with $t_{\text{equil}} \sim (k_{\text{ion}} n_{\text{ion}})^{-1} \sim 3 \times 10^6 \text{ yr } (n_{\text{ion}}/10^{-4} \text{ cm}^{-3})^{-1}$, where $k_{\text{ion}} \sim 10^{-10} \text{ cm}^3 \text{ s}^{-1}$ [Walmsley et al. \(2004\)](#). Typical ion abundances in disks are small, and calculations require involved photochemical networks. Detailed work suggests that ion densities of 10^{-4} cm^{-3} are achieved beyond 30 AU and, depending on the disk’s dust complement, may be present throughout our region of interest (e.g., [Glassgold et al. 1997](#); [Bai & Goodman 2009](#); [Turner et al. 2010](#); [Perez-Becker & Chiang 2011](#)). Inside ~ 10 AU, our atmospheric profiles are less sensitive to whether spin isomers reach thermodynamic equilibrium since disk temperatures exceed the peak conversion temperature of ~ 50 K.

We conclude that during the longest phase of atmospheric growth, to which M_{crit} is most sensitive, the equilibrium EOS is appropriate for the majority of and possibly all of our parameter space.

For our calculations, the difference between thermal equilibrium and a fixed ortho-para ratio of 3:1 is more prominent at larger stellocentric distances, where disk temperatures are lower. We find that a fixed ortho-para ratio may increase the atmospheric evolutionary time by up to a factor of ~ 3 (corresponding to 100 AU in our fiducial disk; see Appendix D.0.8, Figure D.3), and hence M_{crit} by up to a factor of 2. This effect is much smaller in the inner parts of the disk — the atmospheric growth time only increases by $\sim 25\%$ at 10 AU.

3.4 ROLE OF THE EQUATION OF STATE

Variations in the EOS, and hence ∇_{ad} , due to partial dissociation and fractional occupation of H_2 rotational states affect atmospheric evolution by yielding: (1) a lower envelope luminosity L , and (2) a larger amount of radiated energy per unit of accreted mass $-dE/dM$, when compared to the polytropic EOS considered in Paper I. As a result, the rate of change in atmospheric mass,

$$\dot{M} = -\frac{L}{dE/dM}, \quad (3.7)$$

(cf. Equation 3.5 and ignoring surface terms, which only become significant in the late stages of atmospheric evolution) is lower than in the polytropic case. Slower gas accretion increases the growth time of the atmosphere. Since envelope growth is faster for larger cores, we calculate a larger M_{crit} .

Modifications in the EOS affect L and $-dE/dM$ because both of these quantities depend on the global structure of the envelope. From Equation (3.3) applied at the RCB where $\nabla_{\text{ad}} = \nabla_{\text{rad}}$, and for a fixed atmospheric mass, the luminosity emerging from the convective interior scales as $L \propto T_{\text{RCB}}^4/P_{\text{RCB}}$. We have shown in Paper I that the outer radiative layer of the atmosphere is nearly isothermal, and that T_{RCB} is only a factor unity correction from the disk temperature, while the pressure in the radiative region increases exponentially with depth. It follows that L primarily scales as $1/P_{\text{RCB}}$. This pressure depth at the RCB depends on both the interior structure of the atmosphere at high temperatures, and on the matching to the nebula through the radiative region at low temperatures. Similarly, the EOS affects the distribution of total energy $E(r)$ throughout the envelope, and thus $-dE/dM$.

Since both dissociation deep in the convective interior and variable occupation of rotation states in the outer envelope affect atmospheric structure and evolution, it is helpful to separate these effects and study them independently.

Figure 3.2 shows the time evolution of atmospheres forming at 5 AU around cores of mass $M_{\text{c}} = 10M_{\oplus}$ and described by various equations of state, as follows:

1. Ideal gas polytrope with $\nabla_{\text{ad}} = 0.3$.
2. Ideal gas polytrope with $\nabla_{\text{ad}} = 0.3$ for $T > 500$ K and realistic EOS for $T < 500$ K, which includes the effects of fractional occupation of H_2 rotational states.

3. Ideal gas polytrope with $\nabla_{\text{ad}} = 0.3$ for $T < 500$ and realistic EOS for $T > 500$ K, which includes the effects of hydrogen dissociation.
4. Realistic EOS at all T .

We choose $T = 500$ K as the cutoff temperature because the hydrogen-helium mixture behaves like an ideal gas, with $\nabla_{\text{ad}} = 0.3$, in this temperature regime (see Figure 3.1). Both EOS 2 and EOS 3 yield slower gas accretion when compared to EOS 1. Noting the logarithmic scale in Figure 3.2, we see that the combined effect of fractional occupation of rotational states and dissociation is significantly greater than either individually. We explore these contributions in Sections 3.4.1 and 3.4.2.

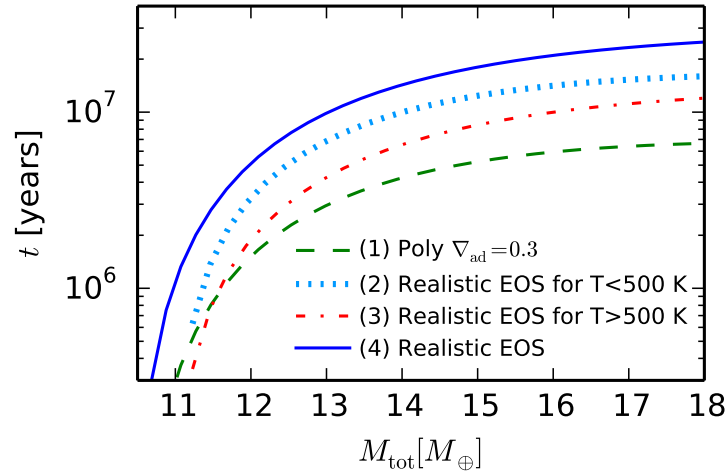


Figure 3.2: Elapsed time to grow a planet of total mass (core + atmosphere) for a variety of EOS combinations (see text), for a planet forming at 5 AU and with a fixed core mass $M_c = 10M_{\oplus}$. Both hydrogen dissociation at high temperatures deep in the atmosphere and fractional occupation of H_2 rotational states at low temperatures in the outer envelope result in slower gas accretion when compared to an ideal gas polytrope.

Throughout Section 3.4, we use a power-law opacity given by

$$\kappa = 2F_{\kappa} \left(\frac{T}{T_{\text{ref}}} \right)^{\beta}, \quad (3.8)$$

with $\beta = 2$, $F_\kappa = 1$, and $T_{\text{ref}} = 100\text{K}$, appropriate for ice grains in the interstellar medium (ISM) (Bell & Lin 1994). We improve our treatment of opacity in Section 3.5.

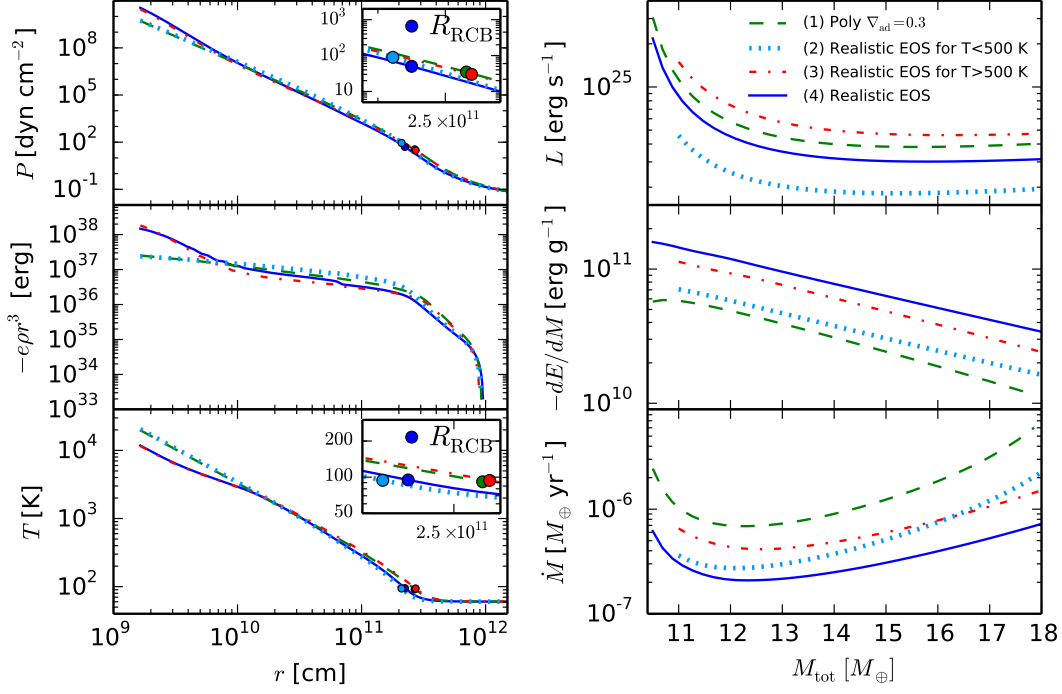


Figure 3.3: We explore atmosphere growth around a core of $M_c = 10M_\oplus$ forming at 5 AU in our fiducial disk, for the EOS choices in Figure 3.2. Left panels show radial profiles of pressure (upper), $-epr^3$ (middle) and temperature (lower), for a total mass (core + atmosphere) of $12M_\oplus$. Right panels display evolution with total mass of L (upper), $-dE/dM$ (middle) and \dot{M} (lower). Upper-left and upper-right: The variable occupation of H_2 rotational states in the outer atmosphere results in a deeper RCB and a lower luminosity for the realistic EOS. Middle-left and middle-right: the (negative) total energy of the atmosphere is more concentrated at the bottom of the envelope when compared to an ideal gas polytrope due to H_2 dissociation. This increases the amount of energy per unit mass, $-dE/dM$, that needs to be radiated away to accrete the next parcel of gas. Lower-left: H_2 dissociation in the inner atmosphere decreases the temperature near the core. Lower-right: Dissociation and fractional occupation of rotational states reduce \dot{M} and thus slow down atmospheric growth.

3.4.1 ROLE OF $-dE/dM$

Variations in ∇_{ad} due to dissociation increase $-dE/dM$ (Figure 3.3, middle-right). The atmosphere's total (negative) energy at scale r , $-epr^3$ is concentrated in the atmospheric interior for all

EOSs (Figure 3.3, middle-left). However, $-e\rho r^3$ for EOS 3 and EOS 4 is much larger in magnitude near the core when compared to the others. This is due to the fact that ∇_{ad} decreases in dissociation regions (Figure 3.1). Dissociation adds particles to the gas and hence increases its entropy. In order for entropy to stay constant with radius in the convective interior, the temperature must drop, lowering ∇_{ad} and $|dT/dr|$ and resulting in lower temperatures near the core (cf. Figure 3.3, bottom-left). Because the specific internal energy $u \propto T$, dissociation decreases the total energy deep in the interior. Note that this loss of thermal energy due to dissociation can be large enough to trigger dynamical instabilities and eventual collapse in higher mass objects such as protostars (Larson 1969) or during the runaway growth of giant planets (Bodenheimer et al. 1980).

The reduced total energy of an atmosphere with a realistic EOS can also be explained qualitatively using ∇_{ad} . The density profile in an adiabatic, non-self-gravitating atmosphere composed of an ideal gas scales as $\rho(r) \propto r^{-1/\nabla_{\text{ad}}+1}$, and the total specific energy is $e(r) \propto 1/r$ (see Paper I). Thus $-e\rho r^3 \sim r^{-1/\nabla_{\text{ad}}+3}$. The total energy is concentrated near the core if $\nabla_{\text{ad}} < 1/3$, and at the outer boundary otherwise. Dissociation reduces ∇_{ad} , and for smaller ∇_{ad} , the total energy is more tightly packed in the envelope's interior.

An atmosphere with more negative total energy (EOS 3 and 4) requires a larger amount of energy to be radiated away to bind the next batch of gas. This implies a larger $-dE/dM$ during atmospheric evolution (Figure 3.3, middle-right), and thus a lower \dot{M} (Figure 3.3, lower-right).

3.4.2 ROLE OF L

The increase in ∇_{ad} at low temperatures, where H_2 rotational states are not fully excited (Figure 3.3, upper-right) decreases the atmosphere's luminosity. This result may be understood as consequence of matching between the atmosphere's interior convective and exterior radiative profiles. The profiles must match at the RCB, constrained by the known total mass. This match determines the pressure at the RCB, $P_{\text{RCB}} \propto \exp(R_B/R_{\text{RCB}})$. Higher P_{RCB} implies lower luminosity (Equation

3.3).

The adiabatic gradient of EOS 2 is larger, on average, than for EOS 1 in the outer part of the convective region.[‡] To understand how a variable, but overall larger ∇_{ad} in the outer atmosphere affects evolution, we study the simplified problem of atmospheres composed of an ideal gas with adiabatic gradient

$$\nabla_{\text{ad}} = \begin{cases} \nabla_{\text{ad},1}, & T > 500 \text{ K} \\ \nabla_{\text{ad},2}, & T < 500 \text{ K} \end{cases} \quad (3.9)$$

where $\nabla_{\text{ad},1}$ and $\nabla_{\text{ad},2}$ are constant (Figure 3.4).

The adiabatic gradient $\nabla_{\text{ad},1}$ dictates the temperature profile deep in the convective interior. Deep in the atmosphere, where $r \ll R_{\text{RCB}}$, virial equilibrium yields a temperature profile

$$T(r) \approx \frac{\nabla_{\text{ad},1} G M_{\text{c}}}{\mathcal{R} r}. \quad (3.10)$$

Even though $\nabla_{\text{ad},1}$ is an order unity coefficient, the temperature scaling with $\nabla_{\text{ad},1}$ in Equation (3.10) is exact (Figure 3.4, upper-right panel). Because the radial temperature profile in the atmospheric interior is set by $\nabla_{\text{ad},1}$, the radius R_{switch} at which the adiabatic gradient changes shows little variation with $\nabla_{\text{ad},2}$.

The RCB temperature, T_{RCB} , is an order unity correction from the disk temperature that depends on the adiabatic gradient in the outer envelope, $\nabla_{\text{ad},2}$. We have shown in Paper I that $T_{\text{RCB}} \simeq T_{\text{d}}(1 - 2\nabla_{\text{ad},2})^{-1/2}$ (for $\beta = 2$ in Equation 3.8). This approximation agrees with the numerically calculated T_{RCB} shown in Figure 3.4 to within 5%. Note that T_{RCB} modestly increases with $\nabla_{\text{ad},2}$ (upper-left panel), and is constant for fixed $\nabla_{\text{ad},2}$ regardless of $\nabla_{\text{ad},1}$ (upper-right panel).

[‡] ∇_{ad} for EOS 2 increases with radius (i.e., with decreasing temperature) throughout the convective zone, then becomes lower near the RCB.

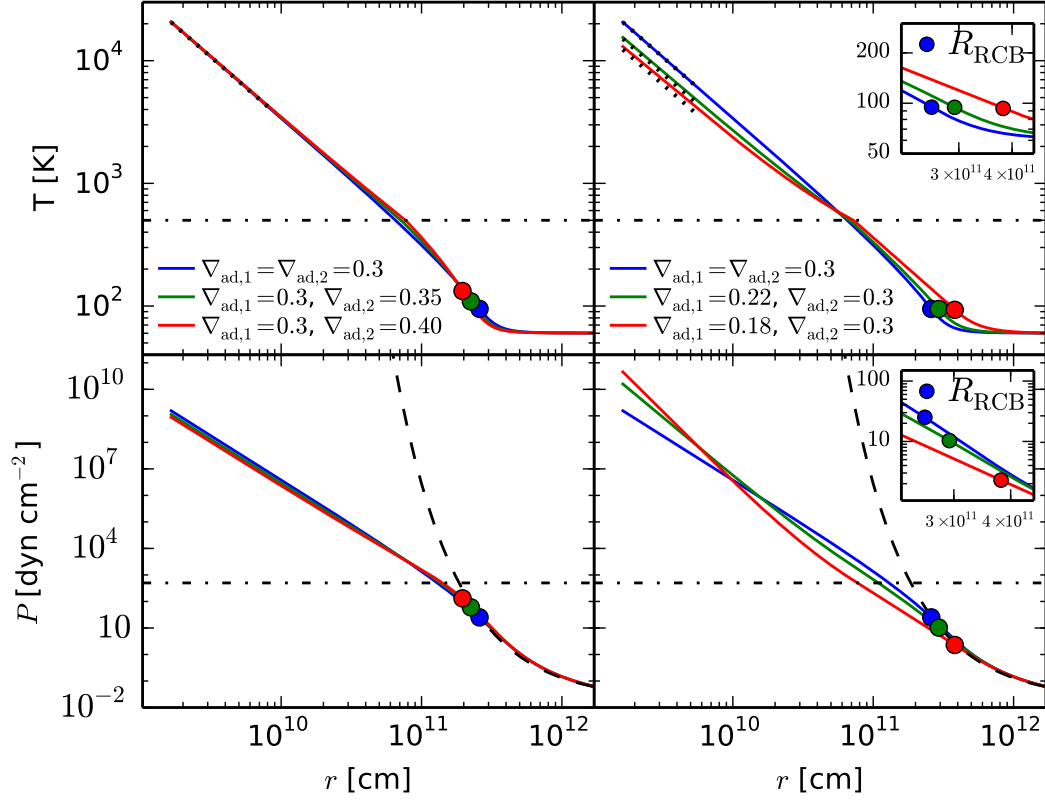


Figure 3.4: As an illustrative numerical experiment, we explore atmosphere growth around a core with $M_c = 10M_\oplus$ forming at 5 AU, and with total mass (core + atmosphere) $12 M_\oplus$, for the EOS choice of Equation (3.9) and various $\nabla_{\text{ad},1}$ and $\nabla_{\text{ad},2}$. In each panel, the circles mark the RCB location. The horizontal dash-dotted lines show the temperature $T_{\text{switch}} = 500$ K at which the adiabatic gradient changes. We show radial profiles of temperature (upper panels) and pressure (lower panels). Upper-left: fixed $\nabla_{\text{ad},1}$, varying $\nabla_{\text{ad},2}$. A larger $\nabla_{\text{ad},2}$ yields a deeper radiative region. Upper-right: varying $\nabla_{\text{ad},1}$, fixed $\nabla_{\text{ad},2}$. A lower $\nabla_{\text{ad},1}$ yields a more shallow radiative region. In both upper panels, the analytic profile of Equation (3.10) is over-plotted for comparison (*dotted line*) in regions of agreement. Lower-left: fixed $\nabla_{\text{ad},1}$, varying $\nabla_{\text{ad},2}$. Lower-right: varying $\nabla_{\text{ad},1}$, fixed $\nabla_{\text{ad},2}$. In both lower panels, the dashed black line is the analytic prediction for the pressure profile in the radiative zone, which agrees with the numerical results.

When these temperature conditions are matched for a fixed atmosphere mass, Figure 3.4 shows that a larger adiabatic gradient in the outer atmosphere results in a deeper radiative region. We can understand this effect by assuming that R_{switch} is fixed. A steeper adiabat (i.e., with a larger adiabatic gradient) that starts at a given depth (here R_{switch}) will match the fixed RCB temperature at a

smaller radius. A quantitative scaling of R_{RCB} is not possible because Equation (3.10) is only valid to order of magnitude at R_{switch} and relatively small variations in the physical depth of the RCB can impact the RCB pressure significantly. It follows that $L \propto 1/P_{\text{RCB}}$ decreases with increasing outer ∇_{ad} ; thus the overall larger adiabatic gradient due to the variable occupation of rotation states at low temperatures decreases L and slows down growth.

3.5 IMPACT OF OPACITY ON ATMOSPHERE EVOLUTION

Our calculations so far have assumed that the dust opacity in the radiative region of the atmosphere is given by the standard ISM opacity. However, our scenario of low planetesimal accretion is likely to favor lower dust opacities, due to grain growth and dust settling. Grain growth, in particular, lowers the absolute value of the opacity, and may change the particle size distribution when compared to the standard ISM size distribution (e.g., [Pollack et al. 1985](#)). Enhanced metallicity due to planetesimal accretion, by construction not present during our atmosphere’s growth, cannot make up for this reduction.

Although grain growth and evidence for a non-ISM size distribution have been observed in protoplanetary disks (e.g., [Beckwith et al. 1990](#), [Beckwith & Sargent 1991](#), [Pérez et al. 2012](#)), the size distribution of dust particles has not been tightly constrained. Typically, the differential grain size distribution is assumed to be a power-law:

$$\frac{dN}{ds} \propto s^{-p}, \quad (3.11)$$

where dN is the number of particles with sizes between s and $s + ds$ and $p = 3.5$ (a standard [Dohnanyi 1969](#) collisional cascade; appropriate for the ISM) or $p = 2.5$ (an approximation for coagulation). In this work we use the [D’Alessio et al. \(2001\)](#) frequency-dependent opacity tables to obtain the temperature-dependent Rosseland mean opacity κ . We take as a fiducial case a maximum

particle size $s_{\text{max}} = 1$ cm and a grain size distribution given by Equation (3.11) with $p = 3.5$. Other choices for the power-law coefficient p are discussed later in this section. Though we choose our opacities to reflect ambient conditions in the disk, we note that grains can also grow within an accreting atmosphere, decreasing its opacity at depth (Movshovitz et al. 2010; Mordasini 2014; Ormel 2014).

The D’Alessio et al. (2001) opacities are only relevant at temperatures that are sufficiently low for dust grains to remain solid ($T \lesssim 1000$ K). At higher temperatures, we use the Bell & Lin (1994) analytic opacity laws, ensuring smooth transition from the grain growth opacities, as illustrated in Figure E.1.

The sharp drop in opacity ($\kappa \sim T^{-24}$, see Figure E.2) due to dust sublimation lowers the radiative temperature gradient significantly (see Equation 3.3), and may thus generate radiative layers within the inner region of the atmosphere (see Appendix E, Figure E.2). Additionally, the weak temperature dependence of grain growth opacities may cause larger outer radiative zones than when ISM opacities are used. This could pose two challenges for our model:

1. The additional luminosity, ΔL , generated in the outer radiative layer of the envelope may not satisfy $\Delta L \ll L$, where L is the assumed fixed atmospheric luminosity. For $p = 3.5$ in Equation (3.11), we have checked that $\Delta L \ll L$ in all the cases presented in this study. For $p = 2.5$, however, this approximation breaks down at low core masses, as we show in §3.6.
2. As little as half of the atmosphere’s luminosity is generated in the innermost convective layer when radiative windows exist. We must therefore check that our assumption of constant L does not substantially change the structure of the atmosphere in the region of the radiative windows. Fortunately, these radiative windows are either very narrow compared to the height of the convective regions (Figure E.2, middle panel), or have $\nabla_{\text{ad}} \approx \nabla_{\text{rad}}$ throughout, which makes the distinction between convective and radiative layers less pronounced

(Figure E.2, bottom panel). This implies that the entropy drop across the radiative windows is small. We investigate the luminosity structure in greater detail in Appendix E and conclude that our model remains a reasonably good approximation even in the presence of radiative windows.

We thus find that our atmospheric and cooling model is valid in our regions of interest, with some exceptions discussed in §3.6.

3.6 CRITICAL CORE MASS

In this section we put together the results obtained in Sections §3.4 and §3.5, and determine the minimum core mass, M_{crit} , to initiate runaway gas accretion during a typical protoplanetary disk lifetime, $t = 3$ Myr. As in Paper I, we quantify the runaway accretion time t_{run} as the time at which the atmosphere growth timescale M_{atm}/\dot{M} drops to 10% of its maximum value (see Paper I for details).

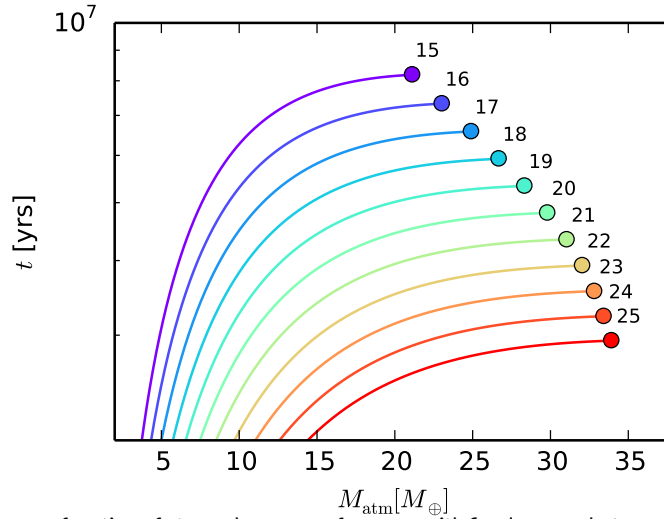


Figure 3.5: Elapsed time as a function of atmosphere mass, for cores with fixed masses between $15M_{\oplus}$ and $25M_{\oplus}$ at $a = 10$ AU in our fiducial disk, for a realistic EOS with an equilibrium ortho-to-para ratio and standard ISM opacity. The circles mark the runaway growth time. The numbers label the core mass in Earth masses. A larger core mass results in a lower t_{run} .

Figure 3.5 displays the time evolution and the runaway growth time for atmospheres forming around cores with masses between $15 M_{\oplus}$ and $25 M_{\oplus}$ at $a = 10$ AU in our fiducial disk, for a realistic EOS with an equilibrium ortho-to-para ratio and standard ISM opacity. Higher mass cores have shorter t_{run} , consistent with the results of Paper I. We also note that M_{atm} at t_{run} is larger for the realistic EOS than for the polytropic EOS considered in Paper I, for the same core mass.

Figure 3.6, upper panel, displays M_{crit} for a gas described by a realistic EOS and an ISM dust opacity. The results of Paper I for an ideal diatomic gas are plotted for comparison. When compared to an ideal gas polytrope, the inclusion of realistic EOS effects increases M_{crit} by a factor of ~ 2 if the H_2 spin isomers are in equilibrium, and by a factor of $\sim 2 - 4$ for a fixed 3:1 ortho-to-para ratio. This latter increase is more significant at larger stellocentric distances. In Figure 3.6, bottom panel, we compare our results with those for a disk with a gas surface density an order of magnitude larger than Σ_d of our fiducial disk (see Equation 3.1a), and find that M_{crit} reduces by ~ 15 -25%.

Figure 3.7 shows M_{crit} as a function of semimajor axis, for a realistic EOS with an equilibrium ortho-to-para ratio and grain growth opacity with a size distribution given by Equation (3.11) with $p = 3.5$ and maximum particle size $s_{\text{max}} = 1$ cm. The critical core mass is lower than in the standard interstellar opacity case, and less sensitive to location in the disk. Location primarily affects the atmosphere through the opacity in the outer envelope, which depends on disk temperature. For the simplified analytic model developed in Paper I, we approximated t_{run} by t_{co} , the time when $M_{\text{atm}} = M_c$, and found that $t_{\text{co}} \sim T_d^{\beta+1/2}$, with β the power-law exponent in Equation (3.8). Opacity is less sensitive to temperature variations for larger grains and has an almost flat profile (see Figure E.1), which results in $\beta \ll 1$ and a much weaker temperature (and therefore semimajor axis) dependence of M_{crit} , as seen in Figure 3.7. Moreover, grain growth reduces the absolute value of the opacity, which also lowers M_{crit} .

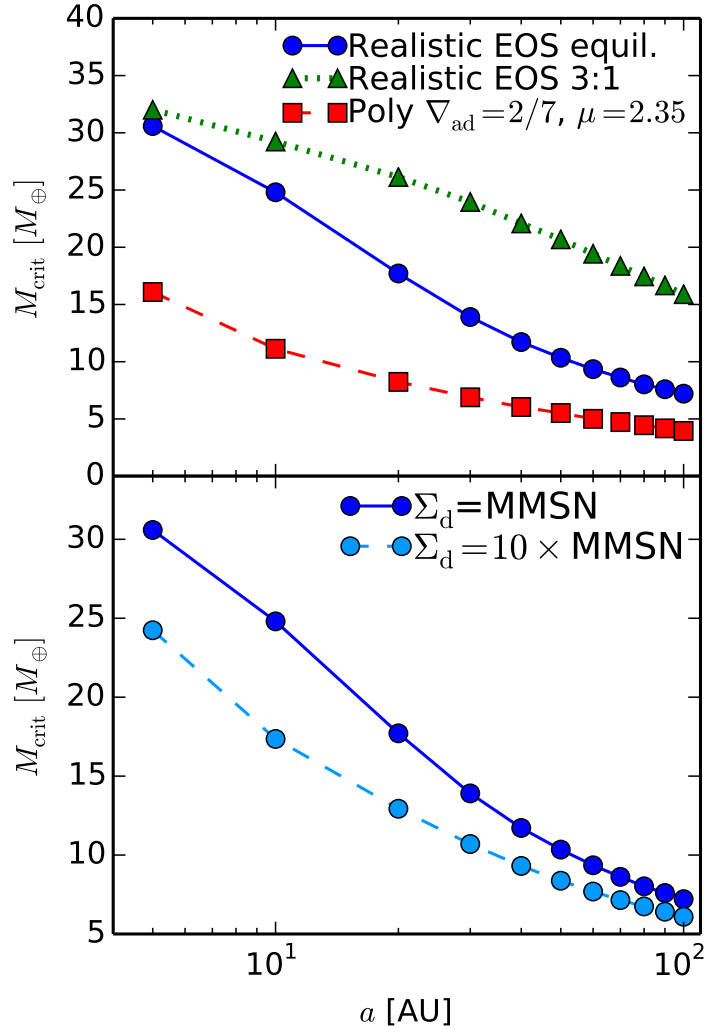


Figure 3.6: Top panel: The minimum core mass for an atmosphere to initiate runaway gas accretion within the lifetime of a typical protoplanetary disk $t \sim 3$ Myrs as a function of semimajor axis, for a realistic hydrogen-helium mixture and a standard ISM opacity. The results of Paper I for an ideal diatomic gas are plotted for comparison. The realistic EOS yields core masses larger by a factor of ~ 2 when compared to the polytrope, for an equilibrium ortho-to-para ratio. The critical core mass is $\sim 2 - 4$ times larger than the polytrope case for a fixed 3:1 ratio between the H_2 spin isomers. The increase is more pronounced at larger stellocentric distances. Bottom panel: Critical core mass as a function of semimajor axis for a disk gas surface density 10 times larger than that of our fiducial disk. A larger Σ_{d} reduces M_{crit} by $\sim 15 - 25\%$.

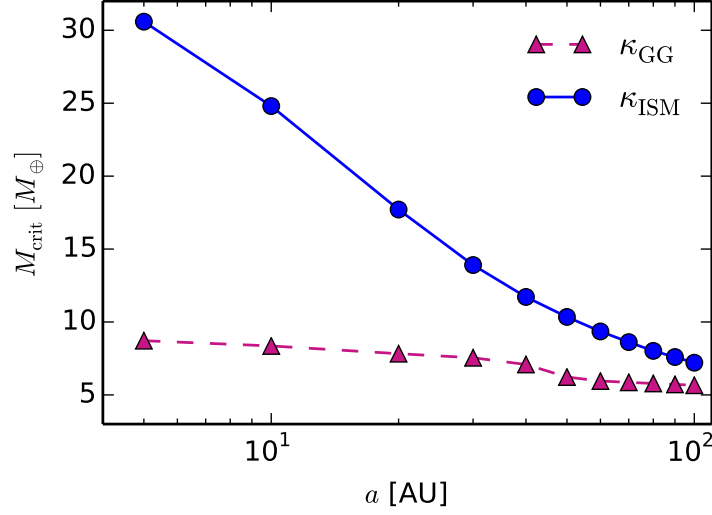


Figure 3.7: Critical core mass as a function of semimajor axis for a realistic EOS with an equilibrium ortho-to-para ratio and radiative opacities that account for grain growth (purple triangles, with $p = 3.5$ and $a_{\text{max}} = 1$ cm; see text for details). The critical core mass is lower than it would be if dust grains had an ISM-like size distribution (blue circles).

In Equation (3.11), the coefficient $p = 3.5$ corresponds to a standard collisional cascade. If coagulation is taken into account, the exponent p can be approximated as $p = 2.5$ (D’Alessio et al. 2001). This results in a flatter and significantly lower opacity (see Appendix E), which may substantially reduce M_{crit} . However, we have found that our model breaks down for low core masses ($M_c \lesssim 3M_{\oplus}$) under our assumption of constant luminosity in the outer radiative layer. Figure 3.8 shows the runaway accretion time t_{run} as a function of semimajor axis for the lowest core mass for which our model is valid, $M_c = 4M_{\oplus}$. The runaway accretion time is more than one order of magnitude lower for $p = 2.5$, which implies that M_{crit} may be, in fact, significantly lower than presented in Figure 3.7. In other words, grain growth can yield critical core masses up to an order of magnitude lower than in the case where interstellar opacities are used.

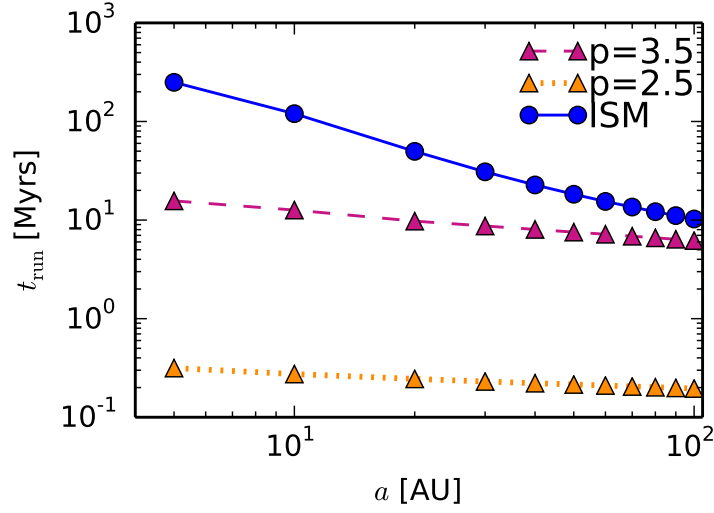


Figure 3.8: Runaway accretion times for a realistic EOS with an equilibrium ortho-to-para ratio and different grain size distributions, for an atmosphere forming around a core with $M_c = 4M_\oplus$. The lines marked by purple and orange triangles have grain growth opacities with $a_{\max} = 1$ cm, and $p = 3.5$ and $p = 2.5$, respectively (see text for details). The blue circle line has an ISM power-law opacity. The runaway accretion time is more than one order of magnitude lower when coagulation is accounted for, i.e. $p = 2.5$.

In summary, we have found $M_{\text{crit}} \sim 30M_\oplus$ at 5 AU, steadily decreasing to $\sim 7M_\oplus$ at 100 AU, for a realistic EOS with the H_2 spin isomers in equilibrium and interstellar opacity. For a fixed 3:1 ortho-to-para ratio and interstellar opacity, M_{crit} is $\sim 32M_\oplus$ at 5 AU and decreases to $\sim 15M_\oplus$ at 100 AU. For a grain growth opacity with a size distribution given by Equation (3.11) with $p = 3.5$ and an equilibrium ortho-to-para ratio, M_{crit} significantly drops to $\sim 8M_\oplus$ at 5 AU and $\sim 5M_\oplus$ at 100 AU. Accounting for coagulation (i.e., $p = 2.5$) M_{crit} is less than $4M_\oplus$ and may be up to an order of magnitude smaller.

3.7 EFFECTS OF PLANETESIMAL ACCRETION

This study considers protoplanets with fully formed cores for which planetesimal accretion is negligible and KH contraction dominates the luminosity evolution of the atmosphere. This approach

contrasts with that of models which assume high planetesimal accretion rates and find that the atmosphere is in steady state and solely heated due to accretion of solids. In both cases, as the envelope and core become comparable in mass, hydrostatic balance no longer holds and runaway gas accretion commences. For fast accretion, M_{crit} is uniquely defined as the maximum core mass for which the atmosphere is still in hydrostatic equilibrium for a fixed planetesimal accretion rate and a set of disk conditions. In this section we compare our results for M_{crit} to analogous results from steady-state fast planetesimal accretion calculations. We discuss the core accretion rates that are necessary for our regime to be valid in §3.7.1. In §3.7.2, we estimate core growth at the maximum rate for which the KH regime is valid, and show it is negligible over the timescale on which the atmosphere evolves. Finally, we compare our results with those assuming fast planetesimal accretion in §3.7.3.

3.7.1 PLANETESIMAL ACCRETION RATES

Kelvin-Helmholtz contraction dominates an atmosphere's luminosity if $L_{\text{acc}} < L_{\text{KH}}$, where L_{acc} is the accretion luminosity,

$$L_{\text{acc}} = G \frac{M_c \dot{M}_c}{R_c}, \quad (3.12)$$

and L_{KH} is given by Equation (3.5) with $L_c = \Gamma = 0$. This condition is satisfied as long as the planetesimal accretion rate

$$\dot{M}_c < \dot{M}_{c,\text{KH}} \equiv \frac{L_{\text{KH}} R_c}{G M_c}. \quad (3.13)$$

To illustrate the magnitude of $\dot{M}_{c,\text{KH}}$, we choose as a fiducial case an atmosphere forming at 30 AU and with a core mass of $10M_{\oplus}$. Since analytic studies of critical core masses at high planetesimal accretion rates assume an ideal gas EOS, for ease of comparison we choose an ideal gas polytropic EOS with constant adiabatic gradient $\nabla_{\text{ad}} = 2/7$ and mean molecular weight $\mu = 2.35$ (see

also Paper I). For this choice of parameters, the runaway accretion time is $t_{\text{run}} \sim 1.4$ Myrs, which is within the typical lifetime of a protoplanetary disk. We also estimate two reference accretion rates. The first one is the core accretion rate $\dot{M}_{\text{c,acc}}$ needed to grow the core to $M_{\text{c}} = 10M_{\oplus}$ on the same timescale as our model atmosphere, $\tau = 1.4$ Myrs:

$$\dot{M}_{\text{c,acc}}(M_{\text{c}}) \sim \frac{M_{\text{c}}}{\tau}. \quad (3.14)$$

The second reference planetesimal accretion rate is $\dot{M}_{\text{c,Hill}}$, a typically assumed planetesimal accretion rate for which the random velocities of the planetesimals are of the order of the Hill velocity around the protoplanetary core (for a review, see [Goldreich et al. 2004](#)). Following Ro6 (equation A1),

$$\dot{M}_{\text{c,Hill}} = \Omega \Sigma_{\text{p}} R_{\text{c}} R_{\text{H}}, \quad (3.15)$$

where Σ_{p} is the surface density of solids, assumed to satisfy $\Sigma_{\text{d}} \approx 100\Sigma_{\text{p}}$ for a dust-to-gas ratio of 0.01.

Figure 3.9 shows that $\dot{M}_{\text{c,KH}}$ is $\sim 2 - 3$ orders of magnitude lower than $\dot{M}_{\text{c,acc}}$. Had the core accreted planetesimals at the $\dot{M}_{\text{c,KH}}$ rate since it started forming, it could not have grown large enough to attract an atmosphere within a typical disk lifetime. Our model requires that the planetesimal accretion rate is initially large during core growth, then significantly reduces as the gaseous envelope accumulates, as suggested by, e.g., [Pollack et al. \(1996\)](#). This is a plausible scenario: the core's feeding zone may be depleted of solids if it is not refilled by radial drift of planetesimals through the nebula, or the core may form in the inner part of the disk and later be scattered outwards by other giants in the system ([Ida et al. 2013](#)).

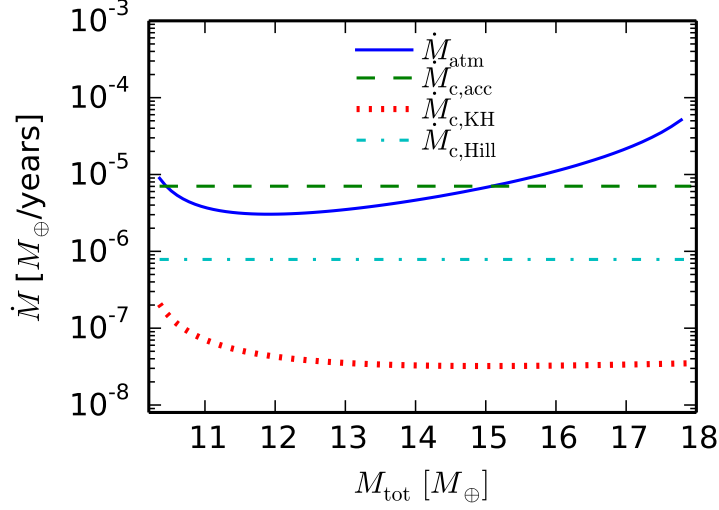


Figure 3.9: Various accretion rates for a planet forming at 30 AU and with a core mass $M_c = 10M_\oplus$, using a polyropic EOS and ISM power-law opacity. For this choice of parameters, the runaway accretion time is $t_{\text{run}} \sim 1.4$ Myrs. The \dot{M}_{atm} (solid blue) curve represents the growth rate of the atmosphere as estimated by our model. The core accretion rate $\dot{M}_{c,\text{acc}}$ (dashed green) necessary to grow the core on the timescale t_{run} is larger than $\dot{M}_{c,\text{KH}}$ (dotted red), the maximum planetesimal accretion rate during KH contraction for which our regime is valid (see text). The frequently used planetesimal accretion rate $\dot{M}_{c,\text{Hill}}$ (dashed-dotted light blue) for which the random velocity of the planetesimals is given by the Hill velocity due to the core (see text), also exceeds $\dot{M}_{c,\text{KH}}$. This motivates our requirement that planetesimal accretion must have slowed down after core growth for our model to be valid.

3.7.2 CORE GROWTH DURING KH CONTRACTION

Planetesimal accretion during the KH contraction phase of atmosphere growth at a rate $\dot{M}_c < \dot{M}_{c,\text{KH}}$ cannot alter the core mass enough to affect the time evolution of the atmosphere. We can quantitatively estimate the maximum increase in core mass as

$$\Delta M_c = \int_0^{t_{\text{run}}} \dot{M}_c dt \approx \sum_i \dot{M}_{ci} \Delta t_i, \quad (3.16)$$

where the accretion rate \dot{M}_{ci} is given by

$$\dot{M}_{c,i} = \frac{L_i R_c}{GM_c} \quad (3.17)$$

from Equation (3.12), with L_i the luminosity of the atmosphere at time t_i in our model. For $M_c = 10M_\oplus$, we find $\Delta M_c \approx 0.05M_\oplus \ll 10M_\oplus$. Core growth is negligible in our regime, and the time evolution of the atmosphere is thus insensitive to core mass changes at a rate imposed by the assumption that $L_{\text{acc}} < L_{\text{KH}}$.

3.7.3 COMPARISON WITH STEADY-STATE RESULTS

We compare our results for M_{crit} with those of studies that assume large planetesimal accretion rates. In principle, the disk lifetime could be short enough that our calculated M_{crit} could exceed the M_{crit} estimated for a steady-state, accretion-heated core. This prospect is not self-contradictory since at higher luminosity, an atmosphere evolves more quickly and hence reaches steady state on a timescale shorter than our calculated KH contraction time. We show here that disk lifetimes are long enough that this is not the case. Our model yields lower core masses than those found when fast planetesimal accretion is considered.

The critical core mass is larger for higher planetesimal accretion, as additional heating increases the core mass required for collapse. As such, if atmosphere collapse does not occur for the lowest value of $\dot{M}_{c,\text{KH}}$ over the course of the atmosphere's growth, then it can only occur in the KH dominated regime.

In order to estimate the critical core mass $M_{\text{crit,KH}}$ corresponding to planetesimal accretion at the rate $\dot{M}_{c,\text{KH}}$, we use the results of Ro6 for low luminosity atmospheres forming in the outer disk ($\gtrsim 2 - 5$ AU). Ro6 assumes an ideal gas polytropic EOS and an opacity lower than that of the ISM (see Equation 3.8). For comparison, we calculate M_{crit} for an ideal gas polytrope and an opacity, κ , given by Equation 3.8 with F_κ reduced by a factor of 100. This choice is comparable to the opacity

law used by Ro6.[§]

Following Ro6, we find that the critical core mass when accretion luminosity dominates the evolution of the atmosphere can be expressed as

$$M_{\text{crit,KH}} \sim \left[\frac{\min[\dot{M}_{\text{c,KH}}(M_{\text{c}})]}{64\pi^2 C} \frac{\kappa}{\sigma G^3} \frac{1}{R_{\text{c}} M_{\text{c}}^{1/3}} \left(\frac{k_B}{\mu m_p} \right)^4 \right]^{3/5}, \quad (3.18)$$

where C is an order unity constant depending on the adiabatic gradient and disk properties (see Ro6, Equation B3). From Equation (3.13), the accretion rate $\dot{M}_{\text{c,KH}}$ depends on the core mass M_{c} . We find $M_{\text{crit,KH}}$ numerically by setting $M_{\text{c}} = M_{\text{crit,KH}}$ on the right-hand side of Equation (3.18). The result is displayed in Figure 3.10; the critical core mass corresponding to planetesimal accretion at the rates displayed in Figure 3.9 is displayed for comparison.

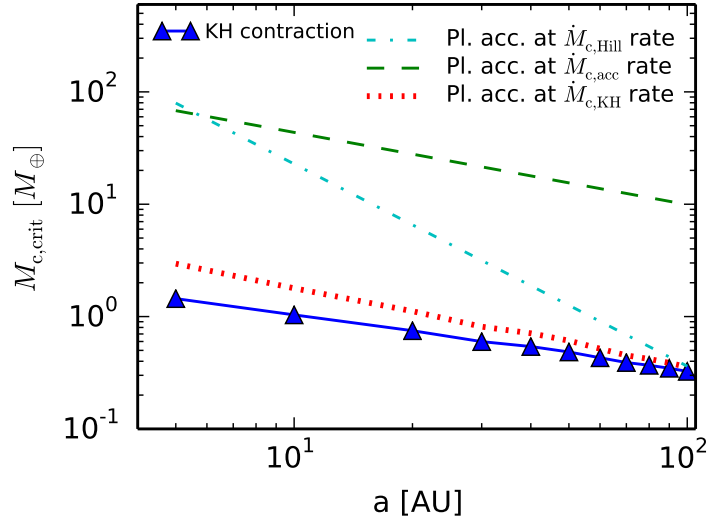


Figure 3.10: Comparison between the critical core mass $M_{\text{crit,KH}}$ given significant planetesimal accretion and the critical core mass when gas contraction dominates, for a polytropic EOS and an ISM opacity reduced by a factor of 100. Our results yield lower core masses than in the fast planetesimal accretion case (e.g., Rafikov 2006). The critical core mass corresponding to $\dot{M}_{\text{c,Hill}}$ and $\dot{M}_{\text{c,acc}}$ from Figure 3.9 is plotted for comparison.

[§]The power-law opacity of Ro6 is scaled to the (semimajor axis dependent) disk temperature, while our opacity is scaled to an absolute reference temperature. We thus cannot directly use the Ro6 opacities for our comparison.

The critical core mass in the regime where KH contraction dominates is smaller than in the case in which planetesimal accretion dominates the evolution of the atmosphere. This leads to two conclusions:

1. Planetesimal accretion can be safely ignored in our regime.
2. Giant planets can form from smaller cores if planetesimal accretion significantly reduces during atmosphere growth.

3.8 SUMMARY

In this paper we study the formation of giant planets embedded in a gas disk. We consider atmospheric evolution around fully grown cores and determine the minimum (critical) core mass, M_{crit} , required to form a gas giant during the typical lifetime of a protoplanetary disk. We improve the model developed in [Piso & Youdin \(2014, hereafter Paper I\)](#) by including realistic equation of state (EOS) tables and dust opacities.

For a realistic EOS with the molecular hydrogen (H_2) spin isomers in thermal equilibrium, and grain growth opacity with maximum particle size $s_{\text{max}} = 1$ cm and a power-law size distribution (3.11) with $p = 3.5$, M_{crit} is $\sim 8M_{\oplus}$ at 5 AU in our fiducial disk and drops to $\sim 5M_{\oplus}$ at 100 AU. The realistic EOS and grain growth opacity have two competing effects on M_{crit} :

1. Realistic EOS effects increase M_{crit} by a factor of ~ 2 when compared to the ideal gas polytrope, for an equilibrium ratio of ortho- and parahydrogen. If the H_2 spin isomers are in a fixed 3:1 ratio, M_{crit} increases by a factor of $\sim 2 - 4$ when compared to the polytrope. This increase is most significant at larger stellocentric distances, where disk temperatures are lower than the peak ortho-to-para conversion temperature of ~ 50 K.
2. Grain growth opacities decrease M_{crit} by a factor of ~ 3.5 at 5 AU and by a factor of ~ 1.2 at 100 AU, when compared to ISM opacities, for a particle distribution given by the power-law

(3.11) with $p = 3.5$ and a maximum particle size of 1 cm. The critical core mass is less sensitive to the location in the disk when realistic opacities are used. If $p = 2.5$, an approximation for coagulation, M_{crit} further reduces by up to an order of magnitude.

In our core accretion models, the dissociation of molecular hydrogen slows the atmospheric cooling and gas accretion rate. This finding is somewhat surprising because H_2 dissociation can trigger the gravitational collapse of protostellar or planetary mass gas clouds (Bodenheimer et al. 1980, Inutsuka 2012). The presence of a massive solid core is the key factor that prevents dissociation from inducing a global collapse in our models.

Our results yield lower core masses than analogous results that consider high planetesimal accretion rates for which the core and atmosphere grow simultaneously. It is thus possible to form a giant planet from a smaller core if the core grows first, then the accretion rate of solids is reduced and a gaseous envelope is accumulated. Moreover, since additional heat sources such as planetesimal accretion limit the ability of the atmosphere to cool and undergo Kelvin-Helmholtz contraction, our results represent a true minimum on the core mass needed to form a giant planet during the typical lifetime of a protoplanetary disk.

4

C/O and Snowline Locations in Protoplanetary Disks: The Effect of Radial Drift and Viscous Gas Accretion

ABSTRACT

The C/O ratio is a defining feature of both gas giant atmospheric and protoplanetary disk chemistry. In disks, the C/O ratio is regulated by the presence of snowlines of major volatiles at different distances from the central star. We explore the effect of radial drift of solids and viscous gas accretion onto the central star on the snowline locations of the main C and O carriers in a protoplanetary disk,

H₂O, CO₂ and CO, and their consequences for the C/O ratio in gas and dust throughout the disk. We determine the snowline locations for a range of fixed initial particle sizes and disk types. For our fiducial disk model, we find that grains with sizes $\sim 0.5 \text{ cm} \lesssim s \lesssim 7 \text{ m}$ for an irradiated disk, and $\sim 0.001 \text{ cm} \lesssim s \lesssim 7 \text{ m}$ for an evolving and viscous disk, desorb at a size-dependent location in the disk, which is independent of the particle's initial position. The snowline radius decreases for larger particles, up to sizes of $\sim 7 \text{ m}$. Compared to a static disk, we find that radial drift and gas accretion in a viscous disk move the H₂O snowline inwards by up to 40 %, the CO₂ snowline by up to 60 %, and the CO snowline by up to 50 %. We thus determine an inner limit on the snowline locations when radial drift and gas accretion are accounted for.

The contents of this chapter are published in *Piso, A.-M. A., Öberg, K.I., Birnstiel, T., & Murray-Clay, R. A. 2015, ApJ, 815, 109*

4.1 INTRODUCTION

The chemical composition of protoplanetary disks affects planet formation efficiencies and the composition of nascent planets. Gas giants accrete their envelopes from the nebular gas. As such, planet compositions are tightly linked to the structure and evolution of the protoplanetary disk in which they form. It is thus essential to understand the disk chemistry and dynamics well enough to (1) predict the types of planet compositions that result from planet formation in different parts of the disk, and (2) backtrack the planet formation location based on planet compositions.

The structures of protoplanetary disks are complex, and affected by a multitude of chemical and dynamical processes (see review by [Henning & Semenov 2013](#)). From the chemistry perspective, volatile compounds are particularly important. Their snowline locations determine their relative abundance in gaseous and solid form in the disk,. Based on protostellar and comet abundances, some of the most important volatile molecules are H₂O, CO₂, CO, N₂. Recent observations of protoplanetary disks have provided valuable information about the abundances and snowline locations

of some of these compounds. For example, the CO snowline has been detected in the disk around TW Hya (Qi et al. 2013), as well as in the disk around HD 163296 (Mathews et al. 2013) using line emissions from DCO^+ . Observations of TW Hya have also revealed a H_2O snowline (Zhang et al. 2013), and more such snowline detections are expected in future ALMA cycles. These observations are currently lacking an interpretive framework that takes into account all important dynamical and chemical processes. Furthermore, such a framework is crucial to connect observed snowline locations to planet formation.

An important consequence of snowline formations in disks is that disks are expected to present different carbon-to-oxygen (C/O) ratios in the gas and in icy dust mantles at different disk radii. This effect was quantified by Öberg et al. (2011b), who considered the fact that the main carriers of carbon and oxygen, i.e. H_2O , CO_2 and CO, have different condensation temperatures. This changes the relative abundance of C and O in gaseous and solid form as a function of the snowline location of the volatiles mentioned above. Öberg et al. (2011b) calculated analytically the C/O ratio in gas in dust as a function of semimajor axis for passive protoplanetary disks and found a gas C/O ratio of order unity between the CO_2 and CO snowlines, where oxygen gas is highly depleted. This effect was used to explain claims of detections of superstellar C/O ratios in exoplanet atmospheres (e.g., WASP-12b, Madhusudhan et al. 2011), which however have been unambiguously refuted (Stevenson et al. 2014, Kreidberg et al. 2015).

Öberg et al. (2011b) assumed a static disk with no chemical evolution. In reality, dynamical and chemical processes affect the snowline locations and the resulting C/O ratio. Several works have addressed some of these effects. Madhusudhan et al. (2014) use a steady-state active disk model that includes planetary migration and use the C/O ratio to constrain migration mechanisms. Ali-Dib et al. (2014) calculate the C/O ratio throughout the disk by incorporating the evolution of solids, i.e. radial drift, sublimation and grain coagulation, as well as the diffusion of volatile vapors. Ali-Dib et al. (2014) use the 1+1D α -disk model of Hughes & Armitage (2010), in which the gas drifts

outwards in the disk midplane, and thus small particles that are well-coupled to the gas will also advect outward. Their model assumes a cyclical conversion between H_2O or CO dust and vapor: large enough particles that are decoupled from the gas drift inwards and start desorbing. Once their sublimation is complete, back-diffusion moves the H_2O or CO vapor outwards to their respective snowlines, where they instantly condense into mm-sized particles that diffuse outwards with the gas while coagulating into larger particles. Once the grains become large enough to decouple from the gas and drift inwards, the cycle restarts. This “conveyor belt” model is based on the pioneering work by Cuzzi & Zahnle (2004), and Ciesla & Cuzzi (2006) for the evolution of H_2O in a viscous disk. This approach leads Ali-Dib et al. (2014) to find that the gaseous C/O ratio increases with time inside the H_2O snowline, approaching unity at 2 AU after $\sim 10^4 - 10^5$ years. Thiabaud et al. (2015) consider additional carbon carrier volatile species in their chemical network, such as CH_4 , and find that the gas C/O ratio may be enriched by up to four times the Solar value in the outer parts of the disk where CH_4 and CO are the only gaseous carriers of C and O. They also include nitrogen carriers such as N_2 or NH_3 , and perform similar calculations for nitrogen.

Each of these studies have considered a specific combination of dynamical and chemical effects. One scenario that has not yet been considered is the combination of radial drift and viscous gas accretion in isolation. Studying these two dynamical processes makes it possible to quantify their separate effect on snowline locations and the C/O ratio at various disk radii.

In this paper, we perform a systematic study to understand the detailed qualitative and quantitative effects of radial drift and gas accretion on the H_2O , CO_2 and CO snowline locations, and the resulting C/O ratio in gas and dust throughout the protoplanetary disk. More importantly, we obtain a limit on how close to the star the snowline locations can be pushed by radial drift and gas accretion.

This paper is organized as follows. In Section 4.2, we present our disk, radial drift and desorption models, as well as the timescales relevant to the coupled drift-desorption process. We calculate the

H₂O, CO₂ and CO snowline locations as a function of particle size for an irradiated and an evolving disk in Section 4.3, and the resulting C/O ratio throughout the disk in Section 4.4. In Section 4.5, we discuss the generality of our results, as well as additional effects on the snowline locations. Finally, we summarize our findings in Section 4.6.

4.2 MODEL FRAMEWORK

We present our protoplanetary disk model for a static, an irradiated, an evolving, and a viscous disk in section 4.2.1. In section 4.2.2, we describe our analytic model for the radial drift of solids. We summarize our ice desorption model in section 4.2.3. Finally, we discuss the relevant timescales for dynamical effects that affect snowline locations in section 4.2.4.

4.2.1 DISK MODEL

To understand the separate effects of radial drift, radial movement of gas throughout the disk due to gas accretion, and accretion heating, we use four separate disk models: *static disk*, which is solely irradiated by the host star and does not take into account gas accretion onto the star or radial drift; *irradiated disk*, which has the same temperature profile as the static disk and does not experience gas accretion or accretional heating, but it takes into account radial drift of solids; *evolving disk*, in which the gas is accreting onto the central star causing the gas surface density to decrease with time, but which does not experience accretion heating; and *viscous disk*, for which the mass flux \dot{M} is constant in time and independent of semimajor axis, and the temperature profile is calculated using both accretional heating and stellar irradiation.

Static and Irradiated disk. We adopt a minimum mass solar nebula (MMSN) disk model for a static and an irradiated disk similar to the prescription of [Chiang & Youdin \(2010\)](#). The gas

surface density and midplane temperature are

$$\Sigma = 2000 (r/\text{AU})^{-1} \text{ g cm}^{-2} \quad (4.1a)$$

$$T = 120 (r/\text{AU})^{-3/7} \text{ K}, \quad (4.1b)$$

where r is the semimajor axis. Our surface density profile is flatter than the $\Sigma \propto r^{-3/2}$ used by Chiang & Youdin (2010). Our choice is inspired by observations of protoplanetary disks at radii larger than ~ 20 AU (e.g., Andrews et al. 2010), which suggest that typical disks may have surface density profiles with $\Sigma \propto r^{-1}$. A slope flatter than $\Sigma \propto r^{-3/2}$ is also more consistent with the temperature profile for a steady-state gas disk (see the Viscous disk heading below and Appendix F). We use the static disk model to compare our results with those of Öberg et al. (2011b).

Evolving disk. We model the evolving disk as a thin disk with an α -viscosity prescription (Shakura & Sunyaev 1973):

$$\nu = \alpha c H. \quad (4.2)$$

Here ν is the kinematic viscosity, $\alpha < 1$ is a dimensionless coefficient and we choose $\alpha = 0.01$, and c , H are the isothermal sound speed and disk scale height, respectively:

$$c = \sqrt{\frac{k_B T}{\mu m_p}} \quad (4.3a)$$

$$H = \frac{c}{\Omega_k}, \quad (4.3b)$$

where k_B is the Boltzmann constant, μ is the mean molecular weight of the gas, m_p is the proton mass, and $\Omega_k \equiv \sqrt{GM_*/r^3}$ is the Keplerian angular velocity, with G the gravitational constant and M_* the stellar mass. We choose $M_* = M_\odot$ and $\mu = 2.35$, corresponding to the Solar composition of hydrogen and helium. The temperature profile for the evolving disk is assumed to be the same

as for the irradiated disk and given by Equation (4.1b). From Equations (4.2) and (4.3), the viscosity can thus be expressed as a power-law in radius, $\nu \propto r^\gamma$, with $\gamma = 15/14 \approx 1$ for our choice of parameters. Following [Hartmann et al. \(1998\)](#), we define $R \equiv r/r_c$ and $\nu_c \equiv \nu(r_c)$, where r_c is a characteristic disk radius. We choose $r_c = 100$ AU. The gas surface density is given by the self-similar solution

$$\Sigma(R, \tilde{t}) = \frac{M(2-\gamma)}{2\pi r_c^2 R^\gamma} \tilde{t}^{-(5/2-\gamma)/(2-\gamma)} \exp \left[-\frac{R^{(2-\gamma)}}{\tilde{t}} \right], \quad (4.4)$$

where M is the total disk mass and

$$\tilde{t} \equiv \frac{t}{t_c} + 1 \quad (4.5a)$$

$$t_c \equiv \frac{1}{3(2-\gamma)^2} \frac{r_c^2}{\nu_c}, \quad (4.5b)$$

where t is time. We choose $M = 0.1M_\odot$ (e.g., [Birnstiel et al. 2012](#)), but we note that our results are insensitive to this choice (see Section 4.5). The irradiated and evolving disk surface densities match at $t \approx 5 \times 10^5$ years in the inner disk, but they diverge at distances larger than a few AU due the exponential cutoff in radius of the surface density of the evolving disk (Equation 4.4).

Viscous disk. Calculating the midplane temperature self-consistently for an evolving disk that is also actively heated, and thus whose thermal evolution is dominated both by accretion heating and stellar irradiation, is non-trivial. We therefore use instead the Shakura-Sunyaev thin disk steady-state solution to derive the midplane temperature profile, T_{act} . The equations governing the evolution of the steady-state disk are listed in Appendix F. We assume an interstellar opacity for the dust grains given by [Bell & Lin \(1994\)](#), but reduced by a factor of 100. This reduction is due to the fact that disk opacities are lower than the interstellar one. While this scaling is consistent with more detailed models of grain opacities in disks (e.g., [Mordasini et al. 2014](#)), realistic disk opacities are much less

sensitive to changes in temperature than the interstellar opacity if substantial grain growth has occurred. However, the disk temperature does not vary significantly across the small region of the disk where accretion heating is important ($r \lesssim 1$ AU). Moreover, using an analytic opacity formula is more convenient since it results in a constant gas surface density in the inner disk region (see below). Our opacity law is thus

$$\kappa = \kappa_0 T_{\text{act}}^2, \quad (4.6)$$

where $\kappa_0 = 2 \times 10^{-6}$. By solving the Equation set (F.1) we find

$$T_{\text{act}} = \frac{1}{4r} \left(\frac{3G\kappa_0 \dot{M}^2 M_* \mu m_p \Omega_k}{\pi^2 \alpha k_B \sigma} \right)^{1/3}. \quad (4.7)$$

Since both accretion heating and stellar irradiation contribute to the thermal evolution of the disk, we compute the midplane temperature for our viscous disk as

$$T^4 = T_{\text{act}}^4 + T_{\text{irr}}^4, \quad (4.8)$$

where to avoid notation confusion $T_{\text{irr}} = T$ from Equation (4.1b), the temperature profile for an irradiated disk. We can then easily determine c and H from Equation (4.3), as well as the viscosity ν from Equation (4.2) for a given α . For consistency, we choose $\alpha = 0.01$ as in the previous case. Finally, we determine Σ from Equation (F.1g), where we choose $\dot{M} = 10^{-8} M_\odot \text{ yr}^{-1}$ based on disk observations (e.g., [Andrews et al. 2010](#)). In the inner portion of our disk ($r \lesssim 1$ AU for our fiducial model with $\dot{M} = 10^{-8} M_\odot \text{ yr}^{-1}$), our choice of opacity (Equation 4.6) implies that the disk has a constant surface density with radius (see Equations F.1).

Before we proceed forward, we note that our disk models assume a constant stellar luminosity L_* , as well as a constant mass accretion rate \dot{M} for the viscous disk. In reality, the stellar luminosity

decreases as the host star contracts, which will reduce the disk temperature and push the snowlines inward, as we explain in Section 4.5.2. For a Solar type star, as our fiducial model assumes, L_* remains relatively constant during the star’s pre-main sequence evolution of ~ 10 Myr (Kennedy et al. 2006), which is larger than the giant planet formation timescale. Thus the midplane temperature will not change significantly for our model due to variations in stellar luminosity, but it may decrease substantially for smaller stars, pushing the snowline inward (see Section 4.5.2 for details). Realistic mass accretion rates, \dot{M} , may vary between $\sim 10^{-7}$ and $\sim 10^{-9} M_\odot \text{ yr}^{-1}$ as the disk evolves (e.g., Chambers 2009, Sicilia-Aguilar et al. 2010). For $\dot{M} \lesssim 10^{-9} M_\odot \text{ yr}^{-1}$, the disk becomes optically thin and hence depleted of gas, which means giant planets must have formed before \dot{M} becomes too low. Garaud & Lin (2007) find that the snowline locations scale as $r_{\text{snow}} \propto \dot{M}^{1/3}$. A factor of 100 reduction in the mass accretion rate will thus move the H_2O snowline inwards by a factor of ~ 4 — since accretion heating is dominant only in the inner disk, the CO_2 and CO snowline locations are unlikely to be affected by changes in mass accretion rate. The inward movement of the H_2O snowline due to the decrease in \dot{M} may be even larger, by up to one order of magnitude (Chambers 2009). We thus conclude that changes in L_* throughout time may only modestly affect our results, while changes in \dot{M} may significantly affect our results for the H_2O snowline, as its location may be determined by the decline in mass accretion rate rather than radial drift. The time variability of L_* and \dot{M} should be taken into account when drawing more robust conclusions, as well as for different host star and disk properties.

4.2.2 RADIAL DRIFT

Solid particles orbit their host star at the Keplerian velocity $v_k \equiv \Omega_k r$. The gas, however, experiences an additional pressure gradient, which causes it to rotate at sub-Keplerian velocity (Weidenschilling 1977). Dust grains that are large enough thus experience a headwind, which removes angular momentum, causing the solids to spiral inwards and fall onto the host star. Small particles

are well-coupled to the gas, while large planetesimals are decoupled from the gas. From the review by [Chiang & Youdin \(2010\)](#), the extent of coupling is quantified by the dimensionless stopping time, $\tau_s \equiv \Omega_k t_s$, where t_s is

$$t_s = \begin{cases} \rho_s s / (\rho c), & s < 9\lambda/4 \text{ Epstein drag} \\ 4\rho_s s^2 / (9\rho c \lambda), & s < 9\lambda/4, \text{Re} \lesssim 1 \text{ Stokes drag.} \end{cases} \quad (4.9)$$

Here ρ is the gas midplane density, $\rho_s = 2 \text{ g cm}^{-3}$ is the density of a solid particle, s is the particle size, λ is the mean free path, and Re is the Reynolds number.

For an irradiated disk, the radial drift velocity can be approximated as

$$\dot{r} \approx -2\eta\Omega_k r \left(\frac{\tau_s}{1 + \tau_s^2} \right), \quad (4.10)$$

where

$$\eta \equiv -\frac{\partial P / \partial \ln r}{2\rho v_k^2} \approx \frac{c^2}{2v_k^2} \quad (4.11)$$

and $P = \rho c^2$ is the disk midplane pressure.

For an evolving disk, the radial drift velocity has an additional term due to the radial movement of the gas ([Birnstiel et al. 2012](#)), i.e.

$$\dot{r} \approx -2\eta\Omega_k r \left(\frac{\tau_s}{1 + \tau_s^2} \right) + \frac{\dot{r}_{\text{gas}}}{1 + \tau_s^2}, \quad (4.12)$$

where \dot{r}_{gas} is the radial gas accretion velocity and can be expressed as (e.g., [Frank et al. 2002](#))

$$\dot{r}_{\text{gas}} = -\frac{3}{\Sigma\sqrt{r}} \frac{\partial}{\partial r} (\nu \Sigma \sqrt{r}) \quad (4.13)$$

with Σ from Equation (4.4). For the viscous disk (see Section 4.2.1), \dot{r}_{gas} can be expressed more

simply using the definition of the mass flux, $\dot{M} = -2\pi r \dot{r}_{\text{gas}} \Sigma$, with \dot{M} fixed and Σ obtained from Equation (F.1g). For our choice of parameters for both the evolving and the viscous disks, we have found that the radial flow of gas (calculated from Equation 4.13 for the evolving disk and from $\dot{r}_{\text{gas}} = -\dot{M}/(2\pi r \Sigma)$ for the viscous disk) is always directed inward for our parameter space of interest, in contrast with the model of [Ali-Dib et al. \(2014\)](#) which assumes that the gas drifts outwards (see Section 4.1). For our evolving disk, the gas starts drifting outwards at a radius $r_{\text{switch}} \approx 200 \text{ AU}$, which is however well outside the CO snowline in our model. We thus note that variations in our fiducial disk model parameters (e.g., T , Σ , \dot{M}) may cause the gas to flow outwards in the outer parts of the disk, specifically at the CO₂ and CO snowline locations. Since drifting particles larger than a few cm are only modestly affected by gas accretion, an outward gas flow would move the CO₂ and CO locations further away from the star only for the smallest particles in our model, which are well-coupled to the gas.

4.2.3 VOLATILE DESORPTION

In order for a volatile species to thermally desorb, it has to overcome the binding energy that keeps it on the grain surface. Following [Hollenbach et al. \(2009\)](#), the desorption rate per molecule for a species x can be expressed as

$$R_{\text{des},x} = \nu_x \exp(-E_x/T_{\text{grain}}), \quad (4.14)$$

where E_x is the adsorption binding energy in units of Kelvin, T_{grain} is the grain temperature, and $\nu_x = 1.6 \times 10^{11} \sqrt{(E_x/\mu_x)} \text{ s}^{-1}$ is the molecule's vibrational frequency in the surface potential well, with μ_x the dimensionless mean molecular weight. We assume that the dust and gas have the same temperature in the disk midplane, hence $T_{\text{grain}} = T$. For H₂O, CO₂ and CO, the binding energies E_x are assumed to be 5800 K, 2000 K and 850 K, respectively ([Collings et al. 2004](#), [Fraser et al. 2001](#), [Aikawa et al. 1996](#)). We use the desorption rate, R_{des} , to estimate the desorption timescale for

particles of different sizes as described in section 4.2.4.

4.2.4 RELEVANT TIMESCALES

We can estimate the extent to which radial drift and gas accretion affect desorption by comparing the timescales for desorption, drift and accretion, for solids of different sizes and compositions.

Desorption timescale. We assume that the solid bodies are perfect spheres and are entirely composed of only one volatile species, i.e. either H_2O , CO_2 or CO^* . The timescale to desorb a single layer of molecules can then be estimated as

$$t_{\text{des}} = \frac{\rho_s}{3\mu_x m_p} \frac{s}{N_x R_{\text{des},x}}, \quad (4.15)$$

where $N_x \approx 10^{15} \text{ sites cm}^{-2}$ is the number of adsorption sites of volatile x per cm^2 , assuming that the particle has a smooth surface (Hollenbach et al. 2009).

Radial drift timescale. To order of magnitude, the radial drift timescale can be estimated as

$$t_{\text{drift}} \sim \left| \frac{r}{\dot{r}} \right|, \quad (4.16)$$

where \dot{r} is the radial drift velocity given by Equation (4.10) for an irradiated disk and by Equation (4.12) for an evolving disk.

Gas accretion timescale. The timescale for gas accretion onto the central star for an evolving disk is (e.g., Armitage 2010)

$$t_{\text{gas,acc}} \sim \frac{r^2}{\nu} \sim \frac{1}{2\alpha\eta\Omega_k}, \quad (4.17)$$

with the latter expression derived from Equations (4.2) and (4.11).

*We discuss the validity of these simplifications in section 4.5.

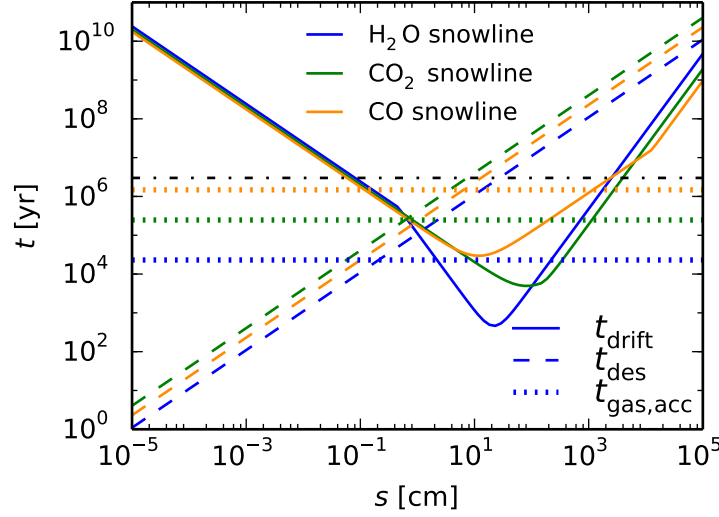


Figure 4.1: Relevant timescales for dynamical effects in the desorption process: t_{drift} (solid lines), t_{des} (dashed lines) and $t_{\text{gas,acc}}$ (dotted lines). The timescales are calculated at three representative locations, i.e. the H_2O , CO_2 and CO snowlines in the static disk. For our choice of parameters, the snowlines are located at ~ 0.7 AU (blue lines), ~ 8.6 AU (green lines) and ~ 59 AU (red lines), respectively. The horizontal dot-dashed line represents a typical disk lifetime of 3 Myr. The particle size ordering at the minimum t_{drift} is not monotonic in snowline distance due to different drag regimes for those particle sizes at the snowline locations (Epstein drag at the H_2O and CO_2 snowlines, and Stokes drag at the CO snowline). Similarly, the ordering of t_{des} is not monotonic in snowline distance due to the non-monotony in mean molecular weight between H_2O , CO_2 and CO ($18 m_p$, $44 m_p$ and $28 m_p$, respectively). Radial drift and gas accretion affect desorption in the regions where their respective timescales, i.e. t_{drift} and $t_{\text{gas,acc}}$, are comparable to the desorption timescale t_{des} .

For simplicity, we calculate the radial drift timescale, t_{drift} , for an irradiated disk in this section, but most of our conclusions hold true for an evolving disk as well. Figure 4.1 shows t_{des} , t_{drift} and $t_{\text{gas,acc}}$ as a function of particle size at three different locations in the disk, corresponding to the H_2O , CO_2 and CO snowlines in the static disk. As expected, micron-sized particles desorb on very short timescales of $\sim 1 - 1000$ years in the close vicinity of their respective snowlines, since the desorption rate depends exponentially on temperature and hence on disk location (see Equation 4.14). On the other hand, their radial drift timescale exceeds the typical disk lifetime of a few Myr by several orders of magnitude due to their strong coupling with the gas. Thus for small particles

in an irradiated disk, the snowline locations and the C/O ratio are the same as for a static disk (see Figure 1 from [Öberg et al. 2011b](#)). This is not true for an evolving disk, however, where gas accretion causes even micron-sized particles to drift significantly before desorbing, as we show in section 4.3. At the other extreme, kilometer-sized particles are unaffected by gas drag and have long desorption timescales ($\gg 1$ Myr), and the snowline locations and C/O ratio remain unchanged in this case as well. This is true for both irradiated and evolving disks, since large planetesimals are decoupled from the gas and hence unaffected by gas accretion onto the host star.

In the particle size regime for which (1) $t_{\text{drift}} \lesssim t_{\text{des}} \lesssim t_{\text{d}}$ ($t_{\text{d}} = 3$ Myr is the disk lifetime), i.e. for ~ 0.5 cm $\lesssim s \lesssim 1000$ cm, or (2) $t_{\text{gas,acc}} \lesssim t_{\text{des}} \lesssim t_{\text{d}}$, i.e. for ~ 0.1 cm $\lesssim s \lesssim 10$ cm, radial drift or gas accretion (or both) are faster than thermal desorption, which is of particular interest for our purposes. We note that $t_{\text{gas,acc}} < t_{\text{d}}$ always holds true. Particles of sizes that satisfy the requirements above will drift significantly due to radial drift or gas accretion before desorbing, thus moving the H₂O, CO₂ and CO snowlines closer towards the central star and changing the C/O ratio throughout the disk. We quantify these effects in sections 4.3 and 4.4.

4.3 SNOWLINE LOCATIONS

In this section we use the model described in section 4.2 to quantify the effects of radial drift (irradiated disk) or radial drift and gas accretion (evolving disk) on the snowline location, for dust particles of different sizes composed of either H₂O, CO₂ or CO. Specifically, we determine a particle's final location (i.e., where the particle either fully desorbs or remains at its initial size due to having a desorption timescale longer than the time at which we stop the simulation) as a function of its initial position in the disk, after the gas disk has dissipated. The disk lifetime, t_{d} , is particularly relevant since the timescale for giant planet formation must be less than or equal to t_{d} . The snowline locations at $t = t_{\text{d}}$ throughout the protoplanetary disk determine the disk C/O ratio in gas at this time, and thus the C/O ratio in giant planet atmospheres that have formed *in situ*, before planetesimal

accretion or core dredging.

For each species x , we determine the final location in the disk of a particle of initial size s_0 by solving the following system of coupled differential equations:

$$\frac{ds}{dt} = -\frac{3\mu_x m_p}{\rho_s} N_x R_{\text{des},x} \quad (4.18a)$$

$$\frac{dr}{dt} = \dot{r}, \quad (4.18b)$$

where the desorption rate $R_{\text{des},x}$ for each particle type (i.e., composed of H_2O , CO_2 or CO) is evaluated at $T = T(r)$, and the radial drift velocity \dot{r} is given by Equation (4.10) for an irradiated disk and Equation (4.12) for an evolving disk. Equations (4.18a) and (4.18b) describe the coupled desorption and radial drift, and can be derived straightforwardly from Equation (4.15). Our initial conditions are $s(t_0) = s_0$ and $r(t_0) = r_0$, where t_0 is the initial time at which we start the integration and r_0 is the initial location of the particle. We choose $t_0 = 1$ year, but our result is independent on the initial integration time as long as $t_0 \ll t_d$. The desorption timescale t_{des} will then satisfy $s(t_{\text{des}}) = 0$, from which we can determine the desorption distance $r_{\text{des}} = r(t_{\text{des}})$.

We define the final position of a grain as the disk location it has reached after $t_d = 3$ Myr, or the radius at which it completely desorbs if that happens after a time shorter than 3 Myr. Figure 4.2 shows our results for H_2O , CO_2 and CO particles, for both an irradiated and an evolving disk. We do not show the results for the viscous disk as they would complicate the plot without adding any qualitative insight — the results for the viscous disk are quantitatively similar with those of the evolving disk for the CO_2 and CO particles, but they are different for the H_2O grains, since accretion heating will push the H_2O snowline outwards (see Section 4.4). We also show the static snowlines for comparison, which are calculated by balancing adsorption and desorption (Hollenbach et al. 2009). Kilometer-sized bodies do not drift or desorb during the disk lifetime neither for an ir-

radiated nor for an evolving disk. Similarly, micron- to mm-sized particles in the irradiated disk do not drift and only desorb if they are located inside the static snowlines. In an evolving disk, however, micron-to mm-sized grains do drift significantly since they move at the same velocity as the accreting gas. For $0.5 \text{ cm} \lesssim s_0 \lesssim 700 \text{ cm}$ in an irradiated disk and $0.001 \text{ cm} \lesssim s_0 \lesssim 700 \text{ cm}$ in an evolving disk, we notice that particles of initial size s_0 desorb at a particle size dependent radius r_{des} regardless of their original location in the disk. In fact, the only grains that will both drift and evaporate are those that reach their fixed final location (represented by the horizontal curves in Figure 4.2) within the disk lifetime. We show in section 4.4 that this result is essential in determining the C/O ratio throughout the disk for different particle sizes.

Another interesting feature of Figure 4.2 is that particles above a certain size ($\sim 7 \text{ m}$ for our choice of parameters) all desorb at the same distance. This is due to the fact that once the large bodies pass the static snowline, they first lose mass, thus eventually following the same evolutionary track as the meter-sized bodies and evaporating at the same location.

Intuitively, this fixed r_{des} should be the location in the disk for which $t_{\text{drift}} \sim t_{\text{des}}$, given an initial particle size. We can calculate this location analytically by equating Equations (4.15) and (4.16) and solving for $r = r_{\text{des}}(s)$ for a given particle size s . Figure 4.3 shows r_{des} calculated analytically using the prescription above as a function of the actual desorption distance calculated numerically. We display this result for the range of particle sizes that desorb at a fixed distance in an irradiated and an evolving disk (see Figure 4.2). We notice that the analytic approximation accurately reproduces the numerical result for most cases of interest, but it deviates for particles larger than $s \gtrsim 10 \text{ cm}$. For small particles with $\tau_s \ll 1$, t_{drift} is a power-law in r (for our parameters, $t_{\text{drift}} \propto r^{-1/14}$ for the irradiated disk in the Epstein drag regime), and the Equation set (4.18) has an explicit analytic solution (see Appendix G). Once particles are large enough so that $\tau_s \sim 1$, t_{drift} has a more complicated dependence on r (see Equation 4.9), and the coupled drift-desorption differential equations have to be integrated numerically to obtain an accurate result.

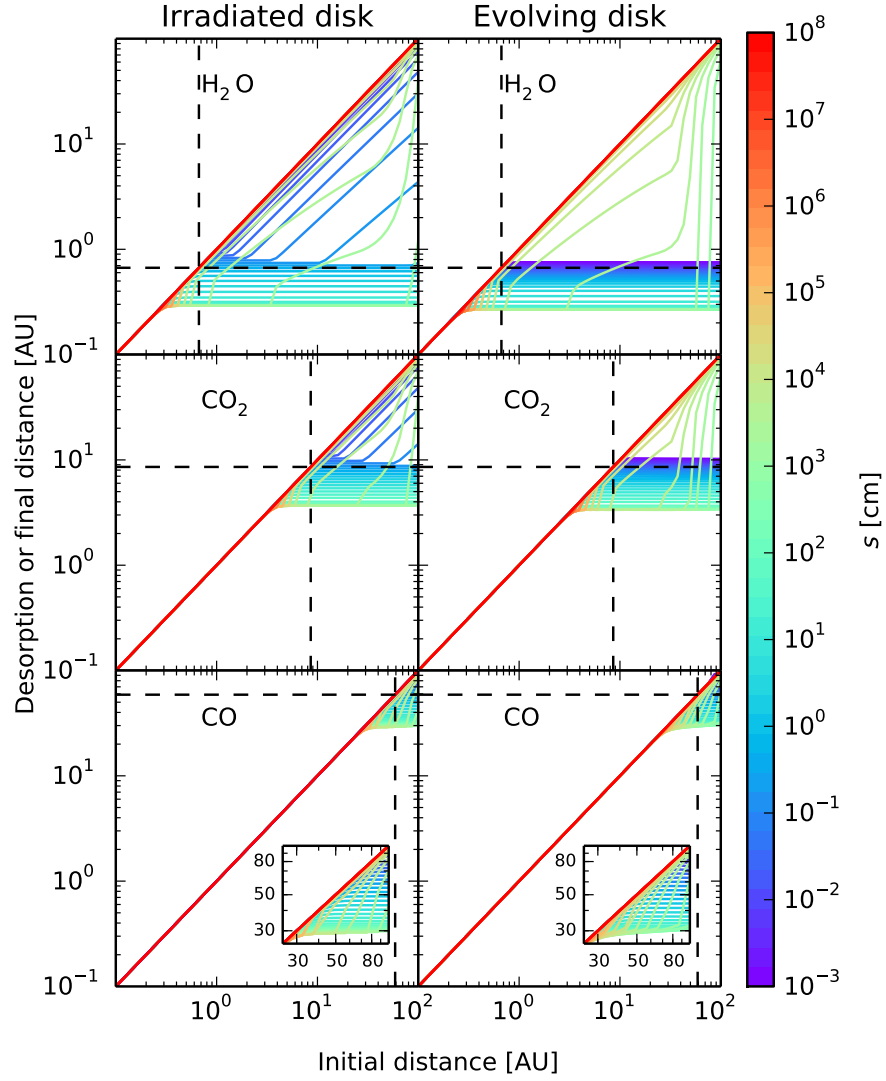


Figure 4.2: Desorption distance (if a grain fully desorbs; horizontal lines) or final distance (if a grain does not fully desorb; diagonal lines for particles that do not drift and non-horizontal, non-diagonal lines for particles that drift), as a function of a particle's initial location in the disk, for a range of particle sizes, and for both an irradiated disk (left panels) and an evolving disk (right panels). The desorption distance is calculated for particles composed of H_2O (top panels), CO_2 (middle panels) and CO (bottom panels). The desorption distance for a static disk is shown for comparison (dashed vertical and horizontal lines). The particle size increases from 10^{-3} cm to 10^8 cm as indicated by the color bar. For a particle of a given initial size that entirely desorbs during $t_d = 3$ Myr, the desorption distance is the same regardless of the particle's initial location.

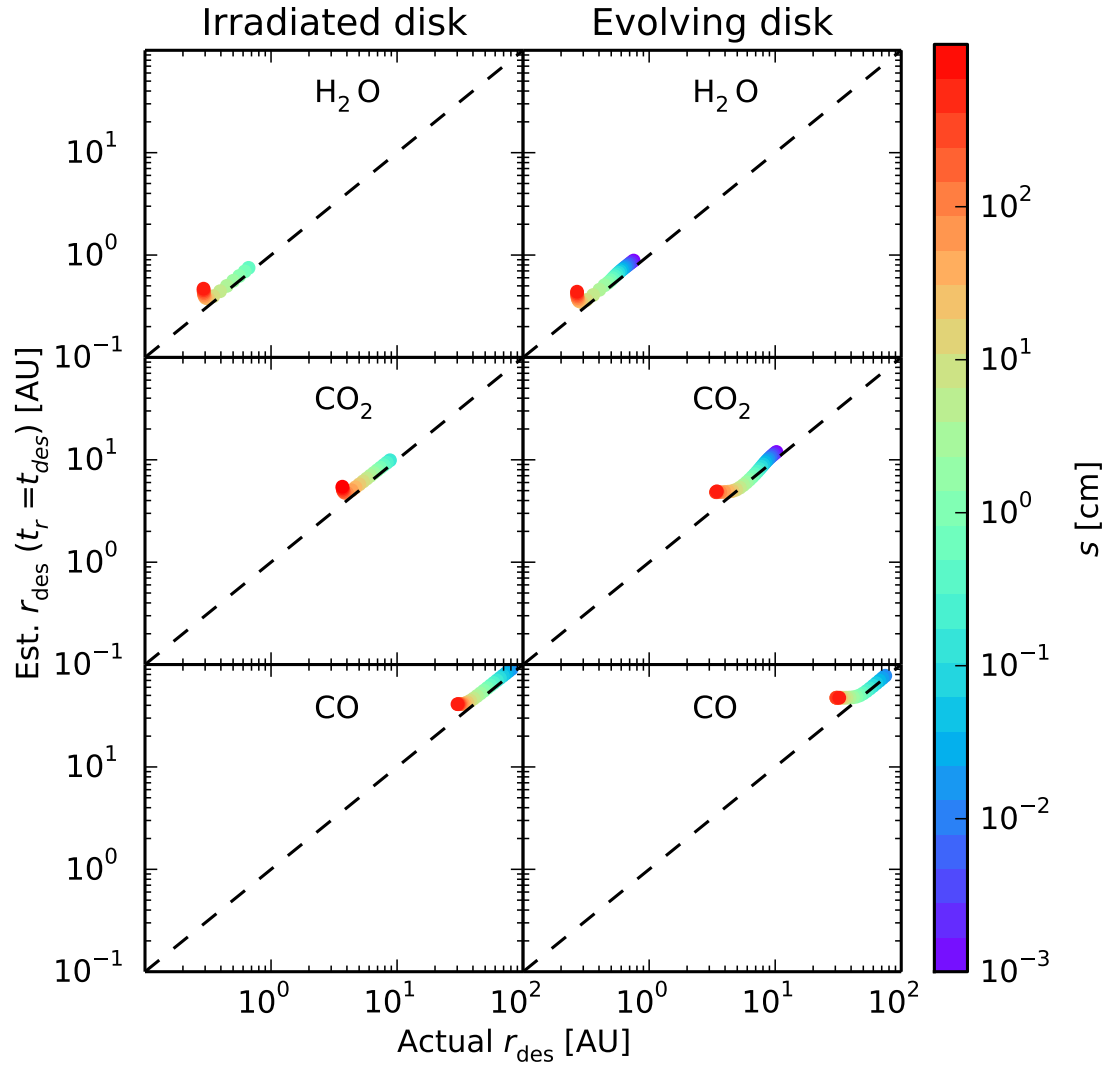


Figure 4.3: Desorption distance estimated from analytic calculations (see text) as a function of the desorption distance calculated numerically, for the range of particle sizes that desorb at a fixed distance regardless of their initial location (see Figure 4.2 and text). The estimate is performed for an irradiated disk (left panels) and an evolving disk (right panels). The particles are composed of H_2O (top panels), CO_2 (middle panels) and CO (bottom panels). The analytic approximation is in good agreement with the numerical result for most cases, with the exception of larger particles, $s \gtrsim 10$ cm (see text).

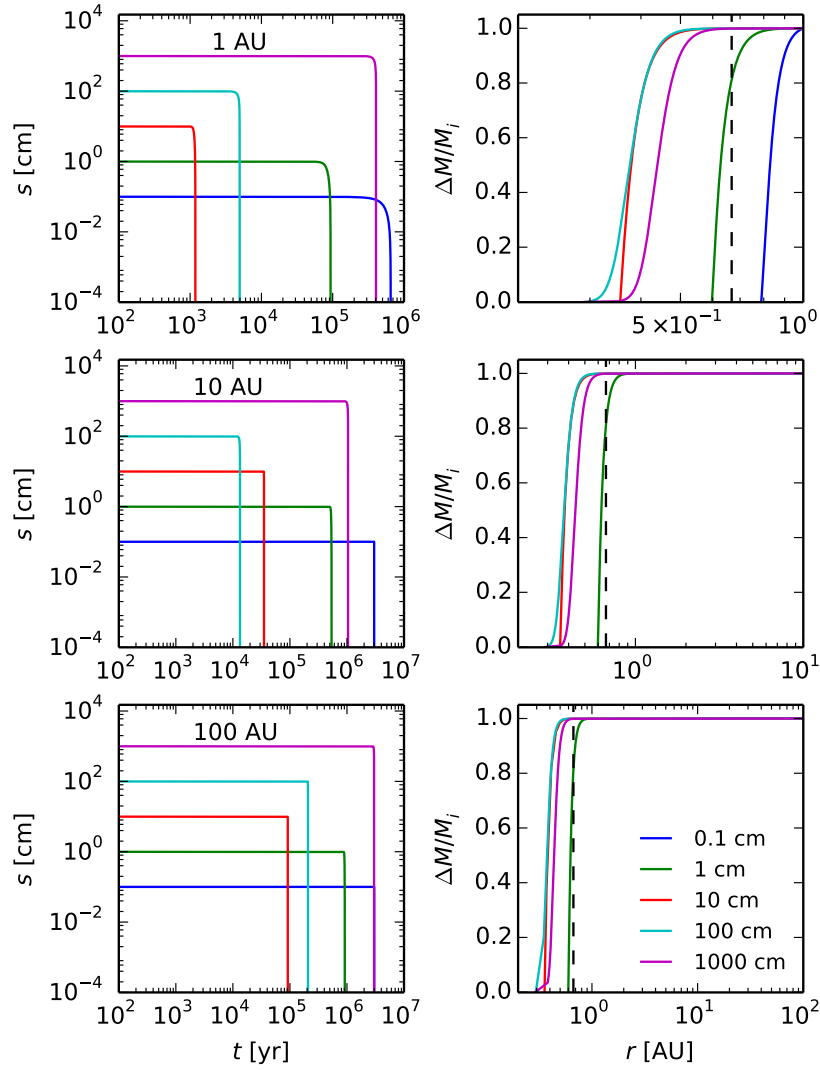


Figure 4.4: Left panels: size of desorbing H_2O particles as a function of time, for different initial particle sizes and for three initial locations in an irradiated disk: 1 AU (top left), 10 AU (middle left) and 100 AU (bottom left). Particles desorb almost instantaneously. Right panel: fractional mass of the desorbing particles as a function of the particle's location as it drifts, for different initial particle sizes, and at the same initial locations presented in the left panel. Particles lose most of their mass very close to the distance at which they fully desorb. The static H_2O snowline is shown for reference (dashed vertical lines).

Given r_{des} , we need to only calculate the distance over which particles desorb to determine the location of a snowline. Figure 4.4, left panels, shows the size evolution with time for H_2O particles of various initial sizes, starting at three different initial locations in an irradiated disk. Once solid H_2O particles begin to evaporate, they do so almost instantly for all explored particle sizes and initial locations.

The right panels of Figure 4.4 show that the drifting grains lose most of their mass in a very narrow distance range; moreover, this distance is the same for a given initial particle size, no matter where the particle started drifting at the time t_0 when the simulation is started. Figure 4.4 thus demonstrates that solid particles that drift and fully desorb during the lifetime of the protoplanetary disk do so (1) instantaneously, and (2) at a fixed stellocentric distance, regardless of their initial location in the disk. It follows that the H_2O , CO_2 and CO snowlines are fixed for a given initial particle size and disk model. Both of these conclusions remain valid for an evolving and a viscous disk, as well as for particles composed of CO_2 or CO , but the snowline locations will vary between the three disks for a given initial particle size (see Section 4.4). If we do not take into account the time dependence of the mass accretion rate and stellar luminosity (see Section 4.2.1), the C/O ratio will then only depend on disk properties, grain size, and the abundance of H_2O , CO_2 and CO relative to the H_2 abundance in the disk midplane, and *not* directly on the disk age when only considering drift, accretion and desorption.

4.4 C/O RATIO ESTIMATES

Given our results in Section 4.3, a disk's C/O ratio is mainly affected by the snowline location for the particle size housing the most mass in ice. Realistic grain size distributions in disks are dominated by large grains (e.g., [D'Alessio et al. 2001](#), [Birnstiel et al. 2012](#)). In Figure 4.5, we display the H_2O , CO_2 , and CO snowline locations as a function of particle size for disks with static chemistry that experience radial drift of solids and gas accretion onto the central star. The minimum snow-

line distance for a disk is given by the curve corresponding to the maximum particle size it hosts. For grains that have grown to radii larger than ~ 7 m and are able to drift and desorb, the ~ 7 m snowline applies (see Section 3).

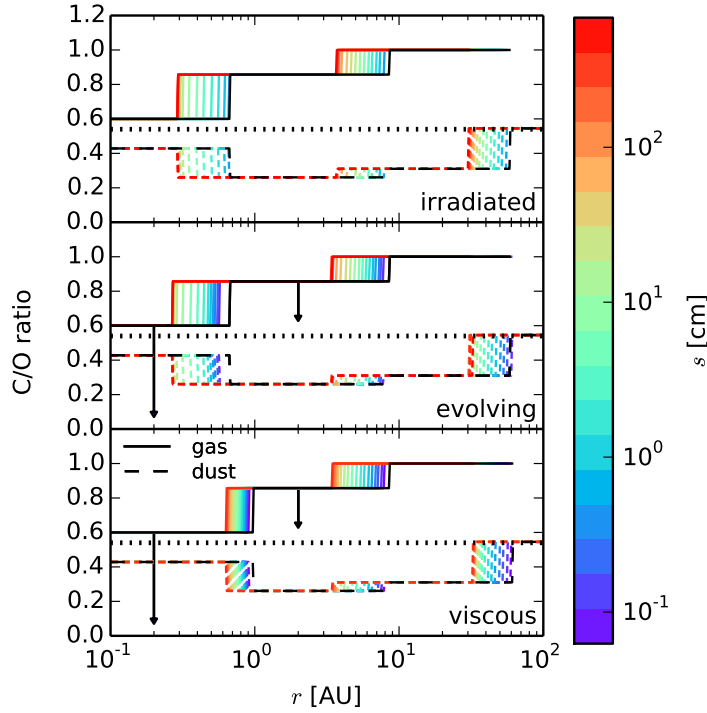


Figure 4.5: Estimated C/O ratio in gas (solid lines) and in dust (dashed lines) for an irradiated disk (top panel), an evolving disk (middle panel) and a viscous disk (bottom panel). The particle size increases from ~ 0.05 cm to ~ 700 cm as indicated by the color bar. The horizontal dotted line represents the stellar value of 0.54. The black lines represent the C/O ratio in gas (solid black line) and dust (dashed black line) for a static disk, with the temperature profile given by Equation (4.1b) for the top two panels and by Equation (4.8) for the bottom panel. For both the evolving and the viscous disk, the movement of desorbed CO_2 gas inside the CO_2 snowline, and of desorbed CO_2 and H_2O gas inside the H_2O snowline due to gas accretion will increase the amount of oxygen gas inside the respective snowlines and thus reduce the gas C/O ratio, as shown by the arrows.

Drift and gas accretion affect the C/O ratio in a disk both because they move the snowline locations of the main C and O carriers and because they cause solids and gas—which contain different proportions of C and O—to move inward at different rates. As shown in Section 3, the snowline

locations depend on disk age only indirectly, through changes in disk properties and grain size. The C/O ratio is a function of the locations of the snowlines and the abundances of H₂O, CO₂, and CO relative to the H₂ abundance in the disk midplane. These abundances evolve over time as solids and gas move inward at different rates.

Figure 4.5 shows the estimated C/O ratio in gas and dust as a function of semimajor axis for an irradiated disk, an evolving disk, and a viscous disk, under the simplifying assumption that the abundance relative to hydrogen for each volatile is fixed, so that drift and accretion affect only the locations of the snowlines. We use the relative number densities of C and O in their different molecular forms (H₂O, CO₂ and CO) from Table 1 of [Öberg et al. \(201b\)](#). Snowline locations correspond to r_{des} in Figure 4.2, representing the location at which particles desorb in the absence of readsorption. The C/O ratio for a static disk, where desorption and readsorption balance ([Hollenbach et al. 2009](#)), is shown as a guideline. We note that the true snowline for particles with r_{des} outside the static snowline is the static snowline itself—thus only particles with initial sizes larger than ~ 0.05 cm are plotted in the three panels, as particles that form snowlines at larger distances (cf. Figure 4.2) are not true snowlines.

Before discussing the quantitative aspects of this plot, it is essential to acknowledge that our estimates for the C/O ratios in the evolving and viscous disks ignore the movement of the desorbed ices with the accreting gas—the relative fluxes of the volatiles in gaseous and solid form will affect the relative abundance of C and O in gas and dust throughout the disk. As demonstrated in Figure 4.4, this will not affect the snowline locations for particles of a given size, but will change the shape of the C/O curves in between the various snowlines. For example, for the disk parameters and particle sizes displayed in Figure 4.5, water molecules in solid particles drift up to ~ 1000 times faster across the H₂O snowline than do molecules of CO and CO₂ vapor that are entrained in the accreting gas. This differential inward motion will result in an increased oxygen gas abundance inside the H₂O snowline, and thus a (in some cases much) lower gaseous C/O ratio in this region. Conversely, oxy-

gen gas inside the water snowline will be depleted compared to the static disk if H_2O particles grow to planetesimal size and stall their migration between the H_2O and CO_2 snowlines, leaving only gaseous CO and CO_2 to accrete inward. Growth of large planetesimals can therefore increase the C/O ratio in the inner disk.

Figure 4.5 plots snowline curves for particle sizes $\sim 0.5 \text{ cm} \lesssim s \lesssim 7 \text{ m}$. In the outermost disk, H_2O , CO_2 , and CO all solidify. Hence, relative drift across the CO snowline can alter only the abundances of volatiles between the CO_2 and CO snowlines, but not the C/O ratio in this region. Interior to the CO_2 snowline, however, relative drift is important. We have found that the largest drifting particles in our model ($\sim 7 \text{ m}$) drift faster than the gas at both the H_2O and CO_2 snowlines. We thus conclude that the C/O ratio interior to the H_2O and CO_2 snowlines in our evolving and viscous disks will be lower than in the static disk, due to the additional oxygen added to the gas by desorbing H_2O and CO_2 . For these particle sizes, our calculated C/O ratio is an upper limit, as indicated by the arrows in Figure 4.5.

Fundamentally, the elevated C/O ratios interior to the static H_2O and CO_2 snowlines are simply caused by the inward movement of the snowlines due to radial drift and gas accretion. Qualitatively, this scenario should be robust to changes in total abundances throughout the disk — for example, at the dynamic (non-static) CO_2 snowlines, the rapid return of CO_2 into gas-phase during CO_2 desorption will reduce the C/O ratio interior to the CO_2 dynamic snowline, while no major change in gas-phase composition, and therefore C/O ratio, is expected between the static and dynamic snowlines.

As noted earlier, we assume that the total (ice and gas) abundance of each volatile is the same at every radius after ices have migrated. This is a good approximation for the irradiated disk, given that this model, by definition, presents a constant influx of particles at any given radius while the gas is static, and thus the ice and gas surface density remain constant. For the evolving disk, the gas-phase C/O ratio may decrease everywhere interior to the H_2O and CO_2 snowlines due to the decline in

the surface density of solids with time at any given radius. For the viscous disk, the solid abundances at a fixed radius are constant, given that this model is not time-dependent, but the gas-to-solid ratio is not constant, which can result in a substantially lower C/O ratio interior to the H₂O and CO₂ snowlines compared to the static case (as indicated by the arrows in Figure 4.5). The main goal of Figure 4.5, however, is to show the different snowline radii in static and non-static disks, and therefore the locations in the disk where the gas-phase C/O ratio is reduced or increased, rather than provide a quantitative estimate of the magnitude of the C/O increase or decrease.

The snowline locations in these disks exhibit several interesting features. For the irradiated disk, only grains larger than ~ 0.5 cm drift, desorb and thus move the snowline compared to the static disk. In contrast, even \sim micron-sized grains drift and desorb for the evolving disk, since they flow towards the host star together with the accreting gas. For the same particle size, the snowline locations are slightly closer to the central star in the evolving disk, due to the fact that the accreting gas adds an additional component to the drift velocity of the solids (cf. Equation 4.12). The addition of accretional heating in the viscous disk moves the H₂O snowline outwards. This is due to the fact that accretional heating dominates in the inner disk, where high temperatures cause the grains to evaporate further away from the star. Once $r \gtrsim 1 - 2$ AU, stellar irradiation dominates the thermal evolution of the disk, and therefore the CO₂ and CO snowlines locations are the same as in the evolving and viscous disks.

Perhaps the most interesting feature is the fact that the snowlines are pushed inwards as the grain size increases. While the plot only shows the snowlines and C/O ratio for particle sizes up to ~ 7 m, we have found that bodies larger than ~ 7 m evaporate at the same location as the meter-sized planetesimals (see Section 4.3). However, the contribution of kilometer-sized bodies to the snowline location is modest, since they only drift if they are located very close to the snowline. Thus the innermost snowlines (depicted in red in Figure 4.5) set the limit on how close in the H₂O, CO₂ and CO snowlines can be pushed due to radial drift and gas accretion on to the host star. For a grain size dis-

tribution with a maximum particle size different than our model, one can pick out the appropriate minimum snowline locations from this plot.

For our choice of parameters, the minimum snowline radii are: $r_{\text{H}_2\text{O}} \approx 0.3$ AU for the irradiated disk, $r_{\text{H}_2\text{O}} \approx 0.26$ AU for the evolving disk and $r_{\text{H}_2\text{O}} \approx 0.63$ AU for the viscous disk; $r_{\text{CO}_2} \approx 3.7$ AU for the irradiated disk, $r_{\text{CO}_2} \approx 3.4$ AU for both the evolving and the viscous disks; $r_{\text{CO}} \approx 30$ AU for the irradiated and both the evolving and the viscous disks. For comparison, $r_{\text{H}_2\text{O}} \approx 0.67$ AU[†], $r_{\text{CO}_2} \approx 8.6$ AU and $r_{\text{CO}} \approx 59$ AU for the static disk. For the viscous disk model, which is the most realistic, radial drift and gas accretion push the snowline locations inwards by up to ~ 40 % for H_2O , by up to ~ 60 % for CO_2 , and by up to ~ 50 % for CO . We note that the H_2O snowline in all disks is significantly closer to the host star compared with Solar system models, which place the H_2O snowline between ~ 2.7 to ~ 3.1 AU (Hayashi 1981, Podolak & Zucker 2004, Martin & Livio 2012). This is partially because we choose a colder disk model, as well as the fact that gas accretion rates decrease over time, moving the snowline location inwards (see also Garaud & Lin 2007 and Section 4.5.2). Min et al. (2011) find that the location of the H_2O snowline is highly sensitive to the gas mass accretion rate \dot{M} (equal to $10^{-8} M_{\odot} \text{ yr}^{-1}$ in our model) and the dust opacity κ (Equation 4.6). Higher values of \dot{M} and κ would increase the accretional component of the disk temperature (cf. Equation 4.7), which would push the H_2O snowline in the viscous disk outwards to match the Solar system snowline. At the same time, the snowline location in Solar type stars may be as close as ~ 1 AU (Mulders et al. 2015), further in than the H_2O snowline in our Solar system.

Observations of the CO snowline in TW Hya (Qi et al. 2013) have found its location at a disk midplane temperature of 17 K (at 30 AU for the TW Hya specific temperature profile). The inferred desorption temperature corresponds to the CO desorption temperature in a static disk, or to desorption from very small grains in an evolving disk, i.e. from grains that are too small to drift

[†]For the viscous disk, we calculated the static snowline location using the same temperature profile as that of the viscous disk, for consistency purposes. Thus $r_{\text{H}_2\text{O}} \approx 0.98$ AU for the static disk in this scenario.

substantially. This suggests that the outer TW Hya disk is dominated by small grains, since larger particles would push the snowline location inwards, and therefore to higher desorption temperatures. This may seem contradictory to observations of grain growth in disks in general and in TW Hya in particular (Wilner et al. 2000). However, recent observations have revealed that grain growth is concentrated to the inner disk (Pérez et al. 2012) and outer disk snowlines may therefore be close to the ones expected in a static disk.

4.5 DISCUSSION

4.5.1 GENERALITY OF RESULTS: DEPENDENCE ON DISK PARAMETERS

In this section we investigate how variations in our fiducial parameters, the total disk mass, disk age, and disk structure, affect the calculated snowline locations and the C/O ratio. All previous results assumed a disk lifetime $t_d = 3$ Myr, the typical disk lifetime and the expected time scale for giant planets to accrete their gaseous atmospheres (e.g., Pollack et al. 1996, Piso & Youdin 2014). Some gas accretion may occur at earlier times, however, before the core is fully formed (e.g., Rafikov 2006). Recent models such as aerodynamic pebble accretion (Lambrechts & Johansen 2012) suggest that rapid core growth on timescales of 10^5 years is possible. The composition of giant planet atmospheres, and specifically their C/O ratio, can thus depend on the abundance of H_2O , CO_2 and CO in gas at earlier times than t_d in the disk evolution.

Figure 4.6 shows the particle desorption or final distance as a function of a particle’s initial location in the disk, for ice particles of initial sizes of 10 cm and 1 m, composed of either H_2O , CO_2 or CO . These sizes are important since radial drift timescales are shortest for particles within this size range (see Figure 4.1) — these are the particles whose drift and desorption evolution should be most strongly affected by variations in disk conditions. We choose the evolving disk as a disk model, and we stop the simulations after 10^4 yr, 10^5 yr, 1 Myr and $t_d = 3$ Myr, respectively. The most

important result of these plots is that particles of a given size always desorb at the same disk radii, the 3 Myr snowline, regardless of simulation stopping time. Particles that start at large stellocentric distances do not desorb within the shorter timeframes, e.g. 10^4 or 10^5 years, but they do evaporate at a fixed radius if their initial location is closer to the host star. While the amount of material that moves through the disk changes with time, the radius at which particles desorb and the snowline locations are thus independent of the time elapsed, and our results for the snowline locations are valid throughout the time evolution of the protoplanetary disk.

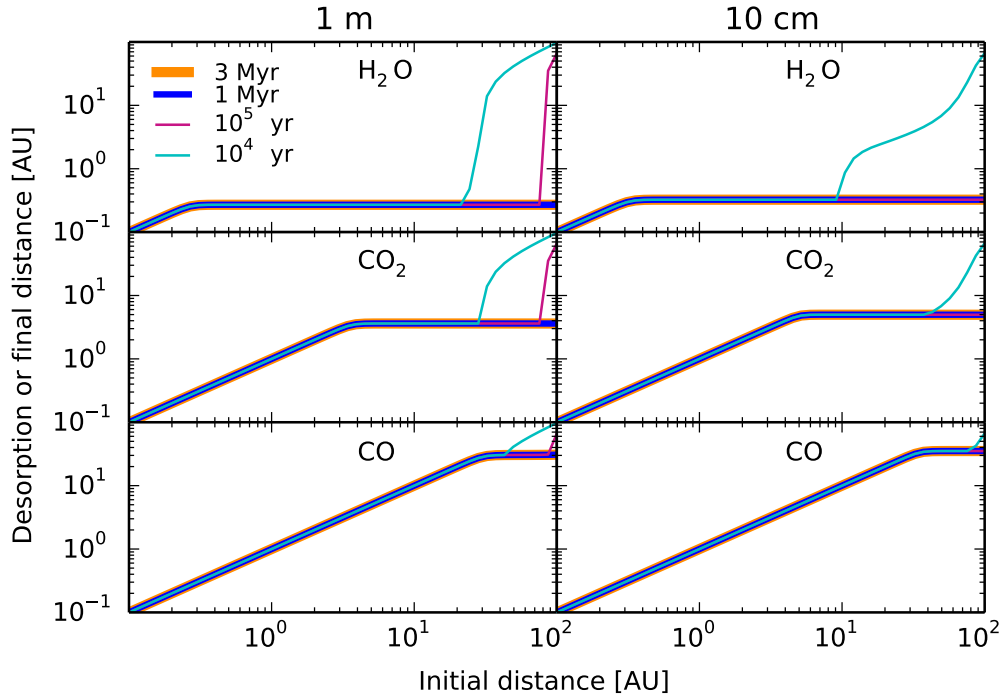


Figure 4.6: Desorption or final distance as a function of initial position in the disk for particles of initial size $s_0 = 1$ m (left panels) and $s_0 = 10$ cm (right panels), for grains composed of H_2O (top panels), CO_2 (middle panels) and CO (bottom panels). The evolution is shown at four representative timescales: 10^4 yr (cyan curve), 10^5 yr (purple curve), 1 Myr (blue curve), and 3 Myr, the disk lifetime (orange curve). For a given particle size, the desorption distance, and hence the H_2O , CO_2 and CO snowlines, have the same location regardless of the time at which the simulation is stopped.

We choose as a fiducial model a total disk mass $M = 0.1M_\odot$. Observationally, disk masses span

at least an order of magnitude around Solar type stars (Andrews et al. 2013). We thus explore the effect of disk mass on the location of snowlines. Figure 4.7 shows the desorption or final distance as a function on the initial location of a H_2O particle with initial size of 1 m, for two total disk masses: $M = 0.1M_\odot$, our fiducial model, and $M = 0.01M_\odot$. Similarly to Figure 4.6, we perform our calculations for an evolving disk. The simulations are stopped after the same timeframes as those in Figure 4.6. The location of the H_2O snowline is the same for both disks (the same holds true for the CO_2 and CO snowlines). The C/O ratio is thus insensitive to the choice of M . We note that our conclusions regarding the disk age and total mass are only valid if the snowline itself does not move with time or disk mass (see also Sections 4.2.1 and 4.5.2).

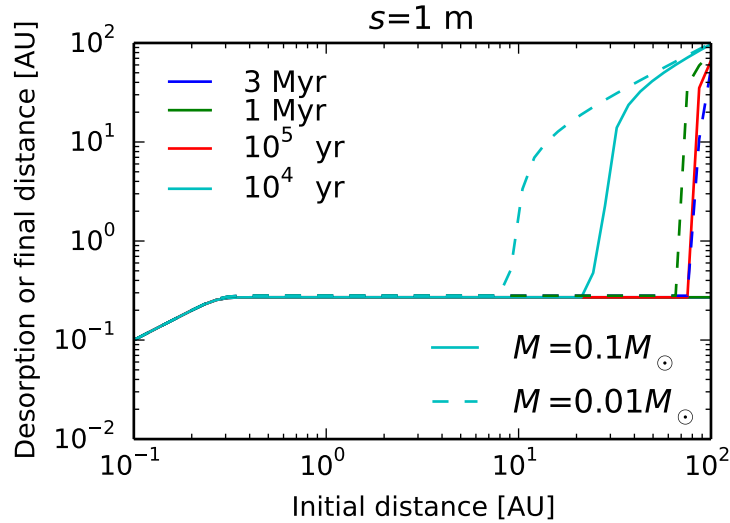


Figure 4.7: Desorption or final distance as a function of initial position in the disk for H_2O particles of initial size of 1 m, for total disk masses $M = 0.1M_\odot$ (solid lines) and $M = 0.01M_\odot$ (dashed lines). The timescales at which we stop the simulations are 10^4 yr (cyan curve), 10^5 yr (red curve), 1 Myr (green curve) and 3 Myr (blue curve). A lower disk mass does not change the snowline location.

We also apply our evolving disk model to a transition disk, i.e. a protoplanetary disk with an inner cavity significantly depleted of gas. We choose a disk with an inner gap of radius $r_0 = 4$ AU, consistent with observations of TW Hya (Zhang et al. 2013), and with the gas surface density in the

gap reduced by a factor of 1000. Figure 4.8 shows the desorption or final distance for a H_2O particle of initial size of 1 m, with the simulation stopped at the same timescales as in Figures 4.6 and 4.7. Particles that start at an initial distance interior to the gap drift towards the original snowline, while grains located exterior to the gap stop shortly after crossing the gap edge, due to the decrease in gas pressure inside the cavity, thus forming a snowline at ~ 3.8 AU. This is qualitatively consistent with the observations of [Zhang et al. \(2013\)](#), which show that the H_2O snowline is pushed outwards in a transition disk compared to a full disk. Our model framework is thus generally valid for more complicated disk structures as well.

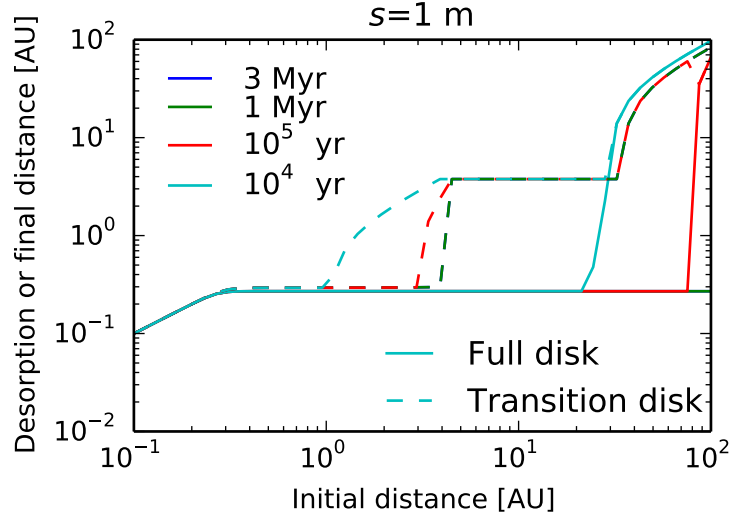


Figure 4.8: Desorption or final distance as a function of initial position in the disk for H_2O particles of initial size of 1 m, for our fiducial disk (solid lines) and for a transition disk with an inner cavity at $r_0 = 4$ AU (dashed lines). The timescales of the simulations and their color code are the same as in Figure 4.7. Particles that start inside the cavity drift towards the original snowline, while particles that start outside the gap stop shortly after crossing the gap edge, due to being trapped in a pressure maximum.

4.5.2 MODEL EXTENSIONS

Our goals in this paper were (1) to gain a qualitative and quantitative understanding of the effect of radial drift and gas accretion onto the central star on snowline locations and the C/O ratio in disks,

and (2) to obtain a limit on how close in the snowlines can be pushed due to drift and gas accretion. We have thus used a simplified model and out of necessity neglected potentially significant dynamical and chemical processes. In what follows, we discuss these limitations and their effects. We note that our future work will address some of these issues.

Table 4.1: The effects of dynamical and chemical processes on snowline shapes and locations

Process	Effect
Radial drift	$\leftarrow \ddagger$
Gas accretion	$\leftarrow \S$
Particle growth	$\leftarrow \P$
Turbulent diffusion	$\rightarrow \leftarrow$
Particle fragmentation	$\rightarrow \leftarrow$
Grain morphology	\rightarrow
Particle composition	$\rightarrow \leftarrow$
Disk gaps and holes	\rightarrow
Accretion rate evolution	$\rightarrow \leftarrow$
Stellar luminosity evolution	\leftarrow
Non-static chemistry	$\rightarrow \leftarrow$

We summarize in Table 1 the potential physical and chemical processes occurring in disks and their effect on snowline locations compared to a static disk. For the sake of completeness, Table 1 also includes the processes addressed in this paper, i.e. radial drift and gas accretion. The neglected effects are discussed in more detail below.

1. Particle growth. While our model assumes a range of particle sizes, each size is considered

initially fixed for a given grain before it drifts and desorbs, since we do not take into account particle coagulation. However, grain growth has been observed in protoplanetary disks (e.g., Ricci et al. 2010, Pérez et al. 2012), as well as theoretically constrained (e.g., Birnstiel et al. 2010, Birnstiel et al. 2012). In Section 4.4 we have shown that larger grains move the snowline locations closer in, but those locations remain fixed above a certain particle size. Particle growth will thus initially push the snowlines inwards. This is consistent with particle growth models, which predict a maximum particle size often around or below the particle sizes that drift the fastest (Birnstiel et al. 2012). As the largest grains contain most of the solid mass, grain growth models should produce snowlines corresponding to our snowline location estimates for the largest grains in the particle size distribution. However, once the solids grow larger than km-sized and form planetesimals, they are no longer affected by drift or desorption, and the snowline reduces to that of a static disk.

2. Turbulent diffusion. The radial drift model presented in Section 4.2.2 only considers a laminar flow and thus ignores turbulence. However, the disk gas also experiences turbulent diffusion (e.g., Birnstiel et al. 2012, Ali-Dib et al. 2014). Turbulence causes eddies and vertical mixing, which are likely to reduce the radial drift velocity of the solids (e.g., Youdin & Lithwick 2007). Additionally, the flow of H₂O, CO₂ and CO vapor will diffuse radially. Back-diffusion across the snowline will change the shape of the snowline, as well as the C/O ratio in gas and dust both inside and outside of the snowline, due to the reduction of gas-phase volatile abundance interior to the snowline.
3. Particle fragmentation. Frequent particle collisions in disks cause them to fragment (e.g., Birnstiel et al. 2012). The fragmentation of meter- to km-sized particles will move the snowlines outwards, as smaller particles desorb faster and further out from the host star (cf. Figures 4.2 and 4.5). Large boulders, which neither drift nor desorb, may become e.g. meter-

sized due to collisions and subsequent fragmentation, which will cause them to drift significantly before desorbing, pushing the snowlines inwards. Thus fragmentation can move the snowline locations in either radial direction — specifically, fragmentation leads to a certain grain size distribution, and the largest particles in this size distribution are the ones that determine the position of the snowline.

4. Grain morphology. Our model assumes that the ice particles are perfect, homogeneous spheres. However, this is not a very good approximation, since grain growth can be fractal rather than compact (Zsom et al. 2010, Okuzumi et al. 2012, Krijt et al. 2015). The inhomogeneity due to cracks in the grain structure will cause the particles to desorb faster. They will therefore drift less before evaporating and will move the snowlines less far inward.
5. Particle composition. The ice particles in our model are assumed to be fully made of either H₂O, CO₂ or CO. More realistically, grains may have a layered structure, such as an interior composed of non-volatile materials (e.g., silicates) covered by an icy layer. The ice thus only constitutes a fraction of the total particle mass, which accelerates its desorption and pushes the snowlines outwards. The grains may also be composed of a mixture of H₂O, CO₂ and CO ices, which will increase the binding energies of the more volatiles species, moving the snowlines inwards.
6. Disk gaps and holes. The snowline locations will be different for transition disks, which have inner cavities significantly depleted of gas (e.g., Espaillat et al. 2012, van der Marel et al. 2015), or pre-transitional disks, which have a gap between an inner and outer full disk (e.g., Kraus et al. 2011). The decrease in gas pressure in these gaps or holes will reduce the particles' drift velocity close to the gap edge, thus slowing them down and pushing the snowline outwards.
7. Accretion rate evolution. Our viscous disk model assumes a constant mass accretion rate \dot{M} .

However, \dot{M} decreases over time, which lowers the accretional component of the disk temperature (Equation 4.7), thus pushing the snowline location inwards if the disk is optically thick (Garaud & Lin 2007). Once \dot{M} reaches low enough values for the snowline to become optically thin, the snowline location moves outwards (Garaud & Lin 2007). During the giant planet formation stage of a few Myr, however, \dot{M} steadily decreases with time (Chambers 2009), which may result in the inward movement of the H₂O snowline by up to one order of magnitude, significantly larger than the inward movement caused by radial drift (cf. Section 4.4). We thus acknowledge that the location of the H₂O snowline may be set by the mass accretion rate evolution rather than the drift of solids.

8. Stellar luminosity evolution. As the host star contracts during its pre-main sequence phase, its luminosity decreases, which reduces the disk temperature and pushes the snowline locations inwards. Kennedy et al. (2006) found that the snowline is unlikely to move significantly during the pre-main sequence phase for Solar type stars, but it may move inward by a factor of $\sim 15 - 20$ for $M_* \sim 0.25 M_\odot$ due to the stellar contraction.
9. Time dependent chemistry. As the goal of this paper was to explore only the dynamical effects on snowline locations and the C/O ratio in disks, we have assumed a simple, static chemical model. In reality, the chemistry in most of the disk is expected to be time-dependent. In the inner disk, chemistry approaches equilibrium due to intense sources of ionizing radiation (e.g., Ilgner et al. 2004), while in the outer disk high energy radiation and cosmic rays are the key drivers of chemistry, which is no longer in equilibrium (e.g., van Dishoeck 2006). A multitude of chemical evolution models have been developed (see references in Henning & Semenov 2013), many of which contain tens or hundreds of chemical reactions. Due to the complexity of these chemical models, most of them are decoupled from disk dynamics. The effect of disk chemistry on snowline locations, shape, time evolution, or the C/O ratio is

therefore difficult to estimate.

4.6 SUMMARY

We study the effect of radial drift of solids and viscous gas accretion onto the central star on the H_2O , CO_2 and CO snowline locations and the C/O ratio in a protoplanetary disk, assuming static chemistry. We develop a simplified model to describe the coupled drift-desorption process and determine the time evolution of particles of different sizes throughout the disk. We assume that the solid particles are perfect, homogeneous spheres, fully composed of either H_2O , CO_2 or CO . We apply our model to an irradiated disk, an evolving disk, and a viscous disk that also takes into account stellar irradiation. We determine the desorption or final location of drifting particles after a time equal to the disk lifetime, and use this result to set an inner limit for the location of the H_2O , CO_2 and CO snowlines. Our results can be summarized as follows:

1. Radial drift and gas accretion affect desorption and move the snowline locations inward compared to a static disk for particles with sizes $\sim 0.5 \text{ cm} \lesssim s \lesssim 7 \text{ m}$ for an irradiated disk and $\sim 0.001 \text{ cm} \lesssim s \lesssim 7 \text{ m}$ for an evolving disk.
2. For our simplified model that does not account for the effects outlined in Section 4.5.2, particles with sizes in the above range desorb almost instantaneously once desorption has begun, and at a fixed location in the disk that only depends on the particle size and the gas accretion rate. Thus for each particle size there is a fixed and uniquely determined H_2O , CO_2 or CO snowline.
3. The results of our numerical simulation are in agreement with the analytic solution of the drift-desorption system of differential equations if the stopping time $\tau_s \ll 1$. We present an explicit analytic solution for the desorption distance in this regime.

4. Since realistic grain size distributions are dominated in mass by the largest particles, the H₂O, CO₂ and CO snowlines are those created by the largest drifting particles in our model. This corresponds to the innermost snowlines that we determine. Our model thus sets a limit on how close to the central star the snowlines can be pushed by radial drift and gas accretion.
5. The snowline locations move inwards as the particle size increases; the innermost snowline is set by particles with initial size $s \sim 7$ m in our model — bigger particles drift too slowly to make it further in before desorbing (see Section 4.3). Gas accretion causes even micron-sized particles to drift, desorb and move the snowline location compared to a static disk. A viscous disk that includes accretion heating moves the H₂O snowline outwards compared to an evolving disk, but has no effect on the CO₂ and CO snowline locations, for our particular choice of mass accretion rate \dot{M} and midplane opacity κ .
6. For our fiducial model, which considers particles with sizes between 10^{-3} and 10^8 cm, the innermost H₂O, CO₂ and CO snowlines are located at 0.3 AU, 3.7 AU and 30 AU for an irradiated disk, 0.26 AU, 3.4 AU and 30 AU for an evolving disk, and 0.63 AU, 3.4 AU and 30 AU for a viscous disk with accretion heating. Compared to a static disk, radial drift and gas accretion move the snowlines by up to 60 % for H₂O and CO₂, and by up to 50 % for CO. For the viscous disk, however, which is the most realistic of the three models since it takes into account accretion heating, the H₂O snowline location moves inwards by up to 40 %.
7. Our C/O estimates confirm the conclusions of [Öberg et al. \(2011b\)](#) that the C/O ratio in gas may be enhanced compared to the stellar value throughout most of the disk, with the C/O ratio reaching its maximum value between the CO₂ and CO snowlines. We note, however, that our results for the C/O ratio do not take into account the radial movement of the desorbed ices with the accreting gas in the evolving and viscous disks, which may significantly decrease the C/O ratio in gas inside the H₂O and CO₂ snowlines. We plan to address this

issue in a future paper.

8. For a constant gas mass accretion rate \dot{M} and stellar luminosity L_* , the snowline locations are independent of the time at which we stop our simulation and of the total disk mass, as long as the disk midplane remains optically thick.

Our model does not address additional effects, such as gas diffusion, grain composition and morphology, or complex time-dependent chemical processes. Future work will address some of these dynamical and chemical processes, with the goal of obtaining more realistic results for the snowline locations, shapes and time evolution, and the resulting effect on the C/O ratio.

5

The Role of Ice Compositions and Morphology for Snowlines and the C/N/O Ratios in Active Disks

ABSTRACT

The elemental compositions of planets define their chemistry, and could potentially be used as beacons for their formation location if the elemental gas and grain ratios of planet birth environments, i.e. protoplanetary disks, are well understood. In disks, the ratios of volatile elements, such as C/O and N/O, are regulated by the abundance of the main C, N, O carriers, their ice binding environ-

ment, and the presence of snowlines of major volatiles at different distances from the central star. We explore the effects of disk dynamical processes, molecular compositions and abundances, and ice morphology on the snowline locations of the main C, O and N carriers, and the C/N/O ratios in gas and dust throughout the disk. The gas-phase N/O ratio enhancement in the outer disk (exterior to the H₂O snowline) exceeds the C/O ratio enhancement for all reasonable volatile compositions. Ice morphology and disk dynamics individually change the snowline location of N₂, the main nitrogen carrier, by a factor of 2-3, and when considered together the range of possible N₂ snowline locations is $\sim 11\text{--}79$ AU in a standard disk model. Observations that anchor snowline locations at different stages of planet formation are therefore key to develop C/N/O ratios as a probe of planet formation zones.

The contents of this chapter have been submitted for publication in *Piso, A.-M. A., Pegues, J., & Öberg, K.I. 2016, ApJ, submitted*

5.1 INTRODUCTION

The chemical composition of protoplanetary disks is largely dictated by the freeze-out of volatile species. The snowline locations of volatile molecules are therefore crucial in determining disk chemical abundances in gas and dust, as well as planet compositions.

Carbon and oxygen bearing molecules, such as H₂O, CO₂ and CO, as well as the carbon-to-oxygen (C/O) ratio in protoplanetary disks and in giant planet atmospheres have been extensively studied from a theoretical standpoint (Öberg et al. 2011b, Ali-Dib et al. 2014, Madhusudhan et al. 2014, Mollière et al. 2015), and snowlines of volatiles such as H₂O and CO have been detected (Zhang et al. 2013, Qi et al. 2013). However, disk chemistry involves many other molecular compounds (Henning & Semenov 2013) including nitrogen bearing species and hydrocarbons (e.g., Mandell et al. 2012), which may affect the compositions of nascent planets.

Both in Solar system comets and in protoplanetary disks, volatile carbon and oxygen are primarily

contained in H_2O , CO_2 and CO (e.g., Lodders 2003, Mumma & Charnley 2011, Öberg et al. 2011b, Boogert et al. 2015). However, some fraction of carbon may also be carried by CH_4 (e.g., Öberg et al. 2008), which may change the C/O ratio in gas and in dust at some disk locations. In the case of nitrogen, chemical models of the protostellar nebula (e.g., Owen et al. 2001) and of protoplanetary disks (e.g., Rodgers & Charnley 2002) suggest that N_2 was the dominant form of nitrogen, and that giant planets have accreted their nitrogen content primarily as N_2 (Mousis et al. 2014). Observations of Solar system bodies such as Titan and Pluto show that N_2 is prevalent in their atmospheres (Cruikshank et al. 1993, Owen et al. 1993). Moreover, the Rosetta spacecraft has recently made the first direct measurement of the N_2 abundance in comet 67P/Churyumov-Gerasimenko (Rubin et al. 2015). Because of the high volatility of N_2 , the gas phase nitrogen-to-oxygen (N/O) ratio in the outer disk may be even more enhanced than the C/O ratio compared to its average value in the disk. Giant planets that form at wide separations should thus have an excess of nitrogen in their atmospheres, which could be used to trace their formation origin. In addition to N_2 , a fraction of the nitrogen abundance may also be carried by less volatile species such as NH_3 (Bottinelli et al. 2010, Mumma & Charnley 2011).

The snowline locations of the main carbon, oxygen and nitrogen carriers strongly depend on the ice grain morphology. Very volatile species, such as CO and N_2 , present binding energies, and therefore snowline locations, that are sensitive to the details of the morphology of the icy grain mantles. Laboratory experiments (Collings et al. 2003, Öberg et al. 2005, Bisschop et al. 2006, Fayolle et al. 2016) have shown that CO and N_2 have significantly different binding energies depending on whether they are pure or water dominated ices. This implies that ices in different environments will sublime at different radii, which will substantially change the disk regions where these volatiles are present in gaseous or solid form (see Section 5.3.2).

In this work, we expand the coupled drift-desorption model developed in (Piso et al. 2015; hereafter Paper I) by considering additional volatile molecules and abundances, ice morphology, as well

as nitrogen-to-oxygen (N/O) ratios. This paper is organized as follows. In Section 5.2, we review the drift-desorption model developed in Paper I. We discuss the effect of different abundances of the main carbon, oxygen and nitrogen carriers, grain morphology and disk dynamics on snowline locations and the C/N/O ratios in Section 5.3. We address the implications of our results in Section 5.4 and summarize our findings in Section 5.5.

5.2 COUPLED DRIFT-DESORPTION MODEL

We begin with a brief review of Paper I’s model for the effect of radial drift and viscous gas accretion on volatile snowline locations. We review our disk model in Section 5.2.1, and summarize our numerical method and results in Section 5.2.2.

5.2.1 DISK MODEL

In this work we consider both a static and a viscous disk. The static disk is irradiated by the central star and does not experience redistribution of solids or radial movement of the nebular gas. To quantify the effects of radial drift and gas accretion, we use a viscous disk with a spatially and temporally constant mass flux, \dot{M} . The viscous disk takes into account radial drift, gas accretion onto the central star, as well as accretion heating. We focus on this disk model which includes all the dynamical and thermal processes we are interested in for the scope of this paper, and do not further consider the other disk models presented in Paper I.

Following [Chiang & Youdin \(2010\)](#), the temperature profile for a static disk is

$$T = 120 (r/\text{AU})^{-3/7} \text{ K}, \quad (5.1)$$

where r is the semimajor axis. We use the [Shakura & Sunyaev \(1973\)](#) steady-state disk solution to

model the viscous disk. From Paper I, the viscous disk temperature profile is computed as

$$T^4 = \left[\frac{1}{4r} \left(\frac{3G\kappa_0 \dot{M}^2 M_* \mu m_p \Omega_k}{\pi^2 \alpha k_B \sigma} \right)^{1/3} \right]^4 + T_{\text{irr}}^4, \quad (5.2)$$

where $T_{\text{irr}} = T$ from Equation (5.1). Here G is the gravitational constant, $\kappa_0 = 2 \times 10^{-6}$ is a dimensionless opacity coefficient, $M_* = M_\odot$ is the mass of the central star, $\mu = 2.35$ is the mean molecular weight of the nebular gas, m_p is the proton mass, $\Omega_k = \sqrt{GM_\odot/r^3}$ is the Keplerian angular velocity, $\alpha = 0.01$ is a dimensionless coefficient (see below for details), k_B is the Boltzmann constant, and σ is the Stefan-Boltzmann constant.

The steady-state disk has an α -viscosity prescription, where the kinematic viscosity is $\nu = \alpha cH$. Here $c \equiv \sqrt{k_B T / (\mu m_p)}$ is the isothermal sound speed (with T from Equation 5.2), and $H \equiv c/\Omega_k$ is the disk scale height. We can then determine the gas surface density for a viscous disk as (Shakura & Sunyaev 1973; see also Paper I for a more detailed explanation of these calculations):

$$\Sigma = \frac{\dot{M}}{3\pi\nu}. \quad (5.3)$$

We choose $\dot{M} = 10^{-8} M_\odot \text{ yr}^{-1}$, consistent with mass flux observations in disks (e.g., Andrews et al. 2010). As described in Paper I, the mass flux rate \dot{M} and stellar luminosity L_* will vary throughout the disk lifetime (Kennedy et al. 2006, Chambers 2009), in contrast with our simplified model which assumes that both quantities are constant. This effect will be most pronounced in the inner disk (\lesssim few AU), where accretion heating dominates. We thus acknowledge that the location of the H₂O snowline may be determined by the decline in \dot{M} or L_* with time, rather than radial drift (see Paper I, Section 2.1 for a more detailed explanation).

5.2.2 DESORPTION-DRIFT EQUATIONS AND RESULTS

The model is described in full in Paper I, here we review and summarize key concepts and results. For a range of initial icy grain sizes composed of a single volatile, we showed in Paper I that the timescale on which these particles desorb is comparable to their radial drift time, as well as to the accretion timescale of the nebular gas onto the central star. We thus have to take into account both drift and gas accretion when we calculate the disk location at which a particle desorbs, since that location may be different from the snowline position in a static disk for a given volatile (see Figure 5.1 and [Öberg et al. 2011b](#)). We determine a particle's final location in the disk by solving the following coupled differential equations:

$$\frac{ds}{dt} = -\frac{3\mu_x m_p}{\rho_s} N_x R_{\text{des},x} \quad (5.4a)$$

$$\frac{dr}{dt} = \dot{r}, \quad (5.4b)$$

where s is the particle size, t is time, μ_x is the mean molecular weight of volatile x , $\rho_s = 2 \text{ g cm}^{-3}$ is the density of an icy particle, $N_x \approx 10^{15} \text{ sites cm}^{-2}$ is the number of adsorption sites of molecule x per cm^{-2} , $R_{\text{des},x}$ is the desorption rate of species x , and \dot{r} is the particle's radial drift velocity. We calculate R_{des} and \dot{r} as follows.

The desorption rate $R_{\text{des},x}$ (per molecule) is ([Hollenbach et al. 2009](#))

$$R_{\text{des},x} = \nu_x \exp(-E_x/T_{\text{grain}}), \quad (5.5)$$

where E_x is the adsorption binding energy in units of Kelvin, $T_{\text{grain}} = T$ is the grain temperature (assumed to be the same as the disk temperature, see Paper I), and $\nu_x = 1.6 \times 10^{11} \sqrt{(E_x/\mu_x)} \text{ s}^{-1}$ is the molecule's vibrational frequency in the surface potential well. We discuss our choices for E_x for the different volatile species in Section 5.3.1.

Following Chiang & Youdin (2010) and Birnstiel et al. (2012), a particle's radial drift velocity can be approximated as

$$\dot{r} \approx -2\eta\Omega_{\text{k}}r\left(\frac{\tau_{\text{s}}}{1+\tau_{\text{s}}^2}\right) + \frac{\dot{r}_{\text{gas}}}{1+\tau_{\text{s}}^2}, \quad (5.6)$$

where the first term is the drift velocity in a non-accreting disk and the second term accounts for the radial movement of the gas. Here $\eta \approx c^2/(2v_{\text{k}}^2)$, where v_{k} is the Keplerian velocity, and $\tau_{\text{s}} \equiv \Omega_{\text{k}}t_{\text{s}}$ is the dimensionless stopping time:

$$t_{\text{s}} = \begin{cases} \rho_{\text{s}}s/(\rho c), & s < 9\lambda/4 \text{ Epstein drag} \\ 4\rho_{\text{s}}s^2/(9\rho c\lambda), & s < 9\lambda/4, \text{Re} \lesssim 1 \text{ Stokes drag,} \end{cases} \quad (5.7)$$

where ρ is the disk mid-plane density, λ is the mean free path and Re is the Reynolds number. The gas accretion velocity \dot{r}_{gas} is determined from $\dot{M} = -2\pi r\dot{r}_{\text{gas}}\Sigma$, for a fixed \dot{M} and with Σ given by Equation (5.3).

For a particle of initial size s_0 , we solve the Equation set (5.4) with the initial conditions $s(t_0) = s_0$ and $r(t_0) = r_0$, where t_0 is the time at which we start the integration and r_0 is the particle's initial location. We stop our simulation after $t_{\text{d}} = 3 \text{ Myr}$, the disk lifetime, since this is roughly the timescale on which planets form, and determine the desorption timescale t_{des} from $s(t_{\text{des}}) = 0$, and thus a particle's desorption distance $r_{\text{des}} = r(t_{\text{des}})$. Our results are insensitive to our choice of t_0 as long as $t_0 \ll t_{\text{d}}$. We note that a particle's size is initially fixed and only changes due to desorption. We thus do not take into account processes such as grain coagulation or fragmentation, which nonetheless occur in disks (e.g., Birnstiel et al. 2012, Pérez et al. 2012). We discuss the effect of these processes on snowline locations in Paper I.

As we show in Paper I, a particle of initial size s_0 can experience three outcomes after $t_{\text{d}} = 3 \text{ Myr}$: (1) it can remain at its initial location, (2) it can drift towards the host star, then stop without evaporating significantly, and (3) it can completely desorb on a timescale shorter than 3 Myr. Parti-

cles in scenarios (1) and (2) are thus not affected by radial drift or gas accretion, and the snowline locations are those for a static disk. In contrast, the grains in case (3) desorb practically *instantaneously* and *at a fixed particle-size dependent location* in the disk, regardless of their initial position. The snowline locations for these particles will thus be fixed for a given initial particle size and disk model. We have found that grains with sizes $\sim 0.001 \text{ cm} \lesssim s \lesssim 7 \text{ m}$ satisfy this condition for our fiducial disk.

5.3 RESULTS

5.3.1 SNOWLINES IN A STATIC DISK: THE IMPORTANCE OF ICE MORPHOLOGY

As we note in Section 5.1, the disk volatile composition and the ice morphology determine the location of important snowlines. In this work we focus on the primary carbon, oxygen and nitrogen carriers, i.e. H_2O , CO_2 , CO , N_2 , and to a lesser extent, CH_4 and NH_3 . Our standard model is based on the median ice abundances observed toward Solar-type protostars (Öberg et al. 2011a), which are $n_{\text{CO}_2} = 0.29 \times n_{\text{H}_2\text{O}}$, $n_{\text{CO}} = 0.38 \times n_{\text{H}_2\text{O}}$, $n_{\text{CH}_4} = 0.0555 \times n_{\text{H}_2\text{O}}$ (hereafter $\text{CH}_4\text{-mid}$) and $n_{\text{NH}_3} = 0.055 \times n_{\text{H}_2\text{O}}$ (hereafter $\text{NH}_3\text{-mid}$). Here $n_{\text{H}_2\text{O}} \approx 10^{-4} \times n_{\text{H}}$ is the total water abundance (van Dishoeck 2006), with n_{H} the hydrogen abundance in the disk midplane. For CO , we also take into account that the observed CO ice only traces some of the CO reservoir due to its high volatility, and similarly to Öberg et al. (2011b) and Paper I we set the total CO abundance to $0.9 \times 10^{-4} n_{\text{H}}$. Finally, we assume that all nitrogen not found in NH_3 is in N_2 and assume a Solar nitrogen abundance, $n_{\text{N}} = 8 \times 10^{-5} n_{\text{H}}$ (Lodders 2003). In effect, this model assumes no chemical evolution between the protostellar and disk midplane stages. This is reasonable for material that accretes onto the disk at large radii (Visser et al. 2009), but may overestimate the contribution of the original volatiles to the total volatile budget in the innermost disk.

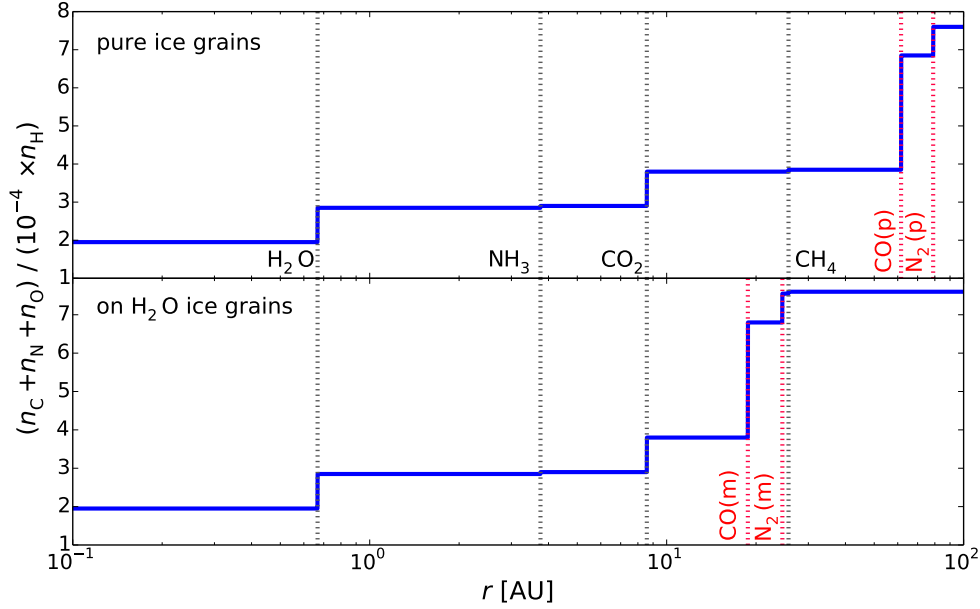


Figure 5.1: The total carbon, nitrogen and oxygen abundance in solids as a function of semimajor axis in a static disk, for CO and N₂ as pure ices (top panel) and water dominated ices (bottom panel). Relevant volatile snowlines are marked by the vertical dashed lines. The grain abundances are calculated as a function of the observed median CH₄ and NH₃ abundances in protostellar cores. The total grain abundance increases with semimajor axis as more and more species freeze out.

We determine the location of the H₂O, CO₂, CO, CH₄, N₂ and NH₃ snowlines in our static disk by balancing desorption with readsorption, following [Hollenbach et al. \(2009\)](#). The binding energies of H₂O, CO₂, CO, CH₄, N₂ and NH₃ as pure ices are 5800 K, 2000 K, 834 K, 1300 K, 767 K and 2965 K, respectively ([Fraser et al. 2001](#), [Collings et al. 2004](#), [Fayolle et al. 2016](#), [Garrod & Herbst 2006](#), [Martín-Doménech et al. 2014](#)). For CO and N₂ as water dominated ices, the binding energies are 1388 K and 1266 K, respectively ([Fayolle et al. 2016](#)). Figure 5.1 shows the resulting snow-line locations, assuming CO and N₂ pure ices (top panel), and CO and N₂ in water dominated ices (bottom panel). The ordinate displays the total carbon, oxygen and nitrogen abundance in solids as a function of the hydrogen total abundance. As expected, the total grain abundance increases with semimajor axis, as more and more species freeze out. Freeze-out at the CO₂ and CO snowlines pulls

more heavy elements into the grains than in the case of the H₂O snowline. The CO and N₂ snowlines move several tens of AU inward if the ices are water dominated rather than pure. This changes the chemical abundances both in gas and dust throughout the disk, directly affecting the compositions of nascent giant planets forming in situ.

5.3.2 C/N/O RATIOS IN STATIC DISKS

In this section we determine the C/O and N/O ratios in gas and dust throughout our static disk, and to what extent they are affected by the presence of CH₄ and NH₃ over the full range of observed CH₄ and NH₃ abundances toward low-mass protostars. In this section we only consider pure ices.

We explore the parameter space of possible CH₄ abundances by assuming three different scenarios: (1) no CH₄, (2) CH₄-mid, and (3) the maximum CH₄ observed abundance (hereafter CH₄-max), $n_{\text{CH}_4-\text{max}} = 0.13 \times n_{\text{H}_2\text{O}}$ (Öberg et al. 2008). Since the abundance of carbon grains is uncertain, we assume that all the carbon that is not in the form of CH₄, CO and CO₂ is in carbon grains, so that we reproduce the Solar C/O ratio (gas+dust) of 0.54.

Figure 5.2 shows the C/O ratio in gas and dust as a function of semimajor axis in a static disk: no CH₄ (top panel), CH₄-mid (middle panel) and CH₄-max (bottom panel). As in Öberg et al. (2011b) and Paper I, a gaseous C/O ratio of unity can be achieved between the CO₂ and CO snowlines, where oxygen gas is significantly depleted. The gas-phase C/O ratio may be further enhanced between the CO₂ and CH₄ snowlines due to the presence of additional carbon gas from CH₄. In this region, the C/O ratio increases by 3% for CH₄-mid and by 8% for CH₄-max, as displayed in the middle and bottom panels of Figure 5.2. Based on the range of observed CH₄ protostellar abundances, its presence in the disk only modestly affects the C/O ratio.

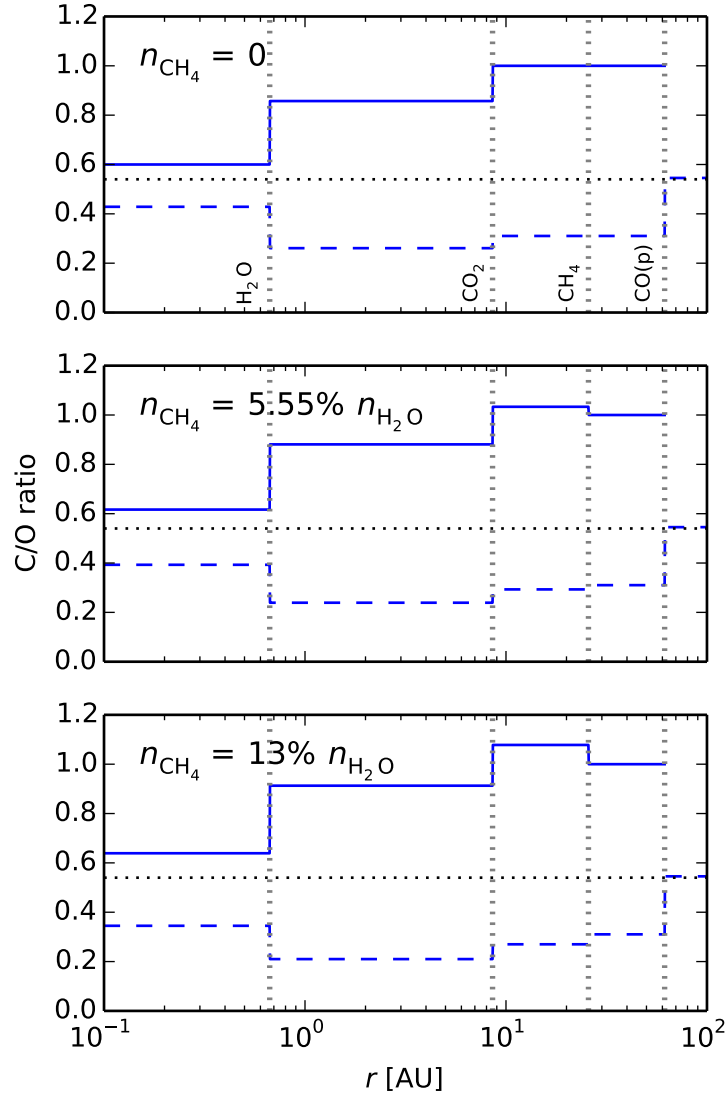


Figure 5.2: The C/O ratio in gas (solid lines) and dust (dashed lines) as a function of semimajor axis in a static disk, assuming no carbon is present in the form of CH_4 (top panel), the median observed CH_4 abundance is assumed (middle panel), and the maximum observed CH_4 abundance is assumed (bottom panel). The C/O estimates are performed assuming that the CO ices are in pure form. The vertical dotted lines mark the snowline locations of the main C and O carriers. The horizontal dotted lines represent the stellar C/O value. The presence of methane only modestly increases the C/O ratio in gas between the CO_2 and CH_4 snowlines.

We assume that the main nitrogen-bearing species are N_2 and NH_3 , since other volatiles that

contain nitrogen have significantly lower abundances in comparison (e.g., [Mumma & Charnley 2011](#)). Similarly to the case of CH_4 , we explore the parameter space of possible NH_3 abundances using observations toward low-mass protostars, as follows: (1) no NH_3 , (2) NH_3 -mid, and (3) the maximum observed NH_3 abundance $n_{\text{NH}_3-\text{max}} = 0.15 \times n_{\text{H}_2\text{O}}$ ([Bottinelli et al. 2010](#)). In each case, the N_2 abundance then simply follows as $n_{\text{N}_2} = (n_{\text{N}} - n_{\text{NH}_3})/2$.

Figure 5.3 shows the snowline locations of the main oxygen and nitrogen carriers and the N/O ratio in gas and dust as a function of semimajor axis in a static disk, for our three choices of the NH_3 abundance: no NH_3 (top panel), NH_3 -mid (middle panel) and NH_3 -max (bottom panel). For comparison, the horizontal dotted lines show the average N/O ratio in the disk. As expected, the gaseous N/O ratio generally exhibits an increasing trend towards the outer disk as more oxygen gas is depleted, with small decreases between the NH_3 and CO_2 snowlines (by 6% for NH_3 -mid and by 18% for NH_3 -max, respectively) due to NH_3 freeze-out. While the presence of NH_3 only moderately affects our results for the N/O ratio, NH_3 is important since otherwise the nitrogen content in solid bodies would be more depleted than is observed for comets and asteroids ([Wyckoff et al. 1991](#), [Mumma & Charnley 2011](#), [Bergin et al. 2015](#)).

The gas-phase N/O ratio is enhanced by a factor of two outside the H_2O snowline compared to its average value, by more than a factor of three between the CO_2 and CO snowlines, and by orders of magnitude between the CO and N_2 snowlines. This latter region can span tens of AU depending on disk parameters and the relative CO and N_2 ice binding environment. This N/O enhancement is more pronounced than the C/O gas phase enhancement of a factor of two in the outer disk (see Figure 5.2).

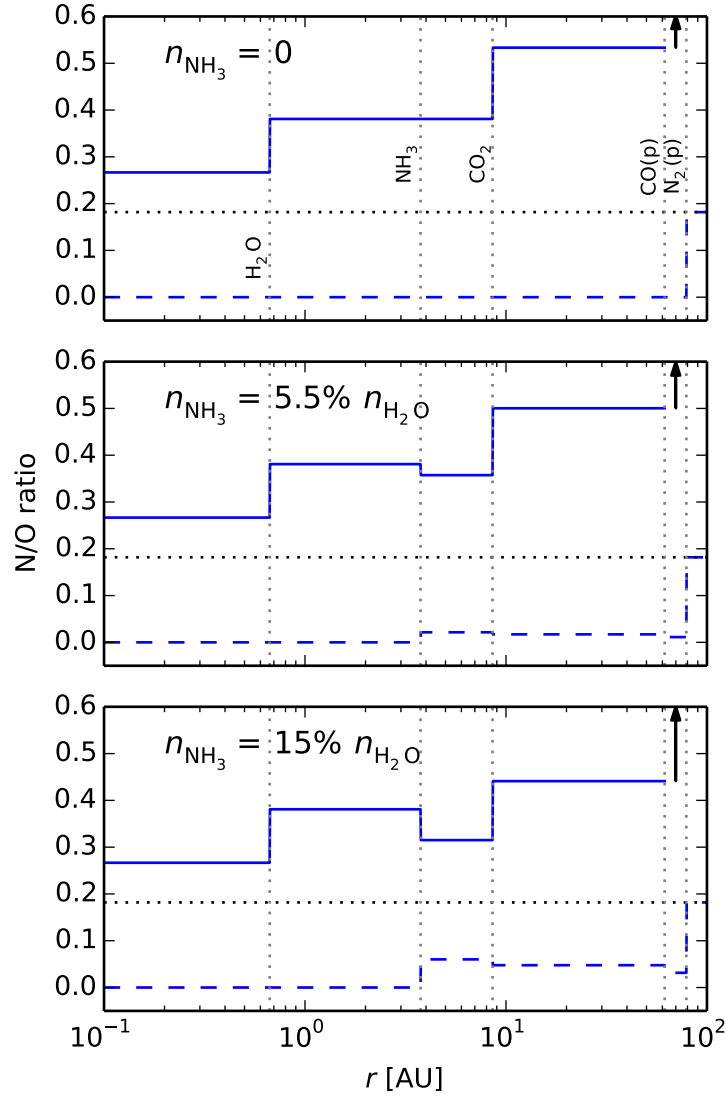


Figure 5.3: The N/O ratio in gas (solid lines) and dust (dashed lines) as a function of semimajor axis in a static disk, assuming no nitrogen is present in the form of NH_3 (top panel), the median observed NH_3 abundance is assumed (middle panel), and the maximum observed NH_3 abundance is assumed (bottom panel). The N/O estimates are performed assuming that the CO and N_2 ices are in pure form. The vertical dotted lines mark the snowline locations of the main C, O and N carriers. The horizontal dotted lines represent the average N/O value in the disk. The gas-phase N/O ratio is enhanced by a factor of two between the H_2O and CO_2 snowlines compared to its average value, and by a factor of three between the CO_2 and CO snowlines. The arrows mark a highly elevated N/O ratio in gas between the CO and N_2 snowlines due to the depletion of oxygen gas in this region. The presence of NH_3 moderately decreases the N/O ratio in gas between the NH_3 and CO_2 snowlines.

5.3.3 C/N/O RATIOS IN DYNAMIC DISKS

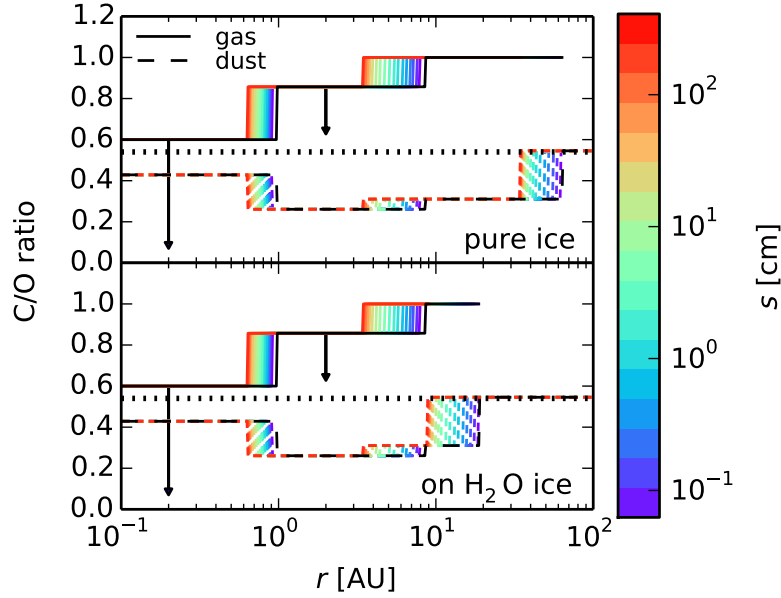


Figure 5.4: C/O ratio estimates in gas (solid lines) and dust (dashed lines) as function of semimajor axis in a viscous disk, for CO as pure ice (top panel) or as water dominated ices (bottom panel). The H₂O, CO₂ and CO snowlines are shown for particles with initial sizes $\sim 0.05 \text{ cm} \lesssim s \lesssim 7 \text{ m}$ as indicated by the color bar. The C/O ratio in a static disk (black lines) is shown for comparison. The arrows show that the C/O ratio in gas will decrease inside the H₂O and CO₂ snowlines in the viscous disk, as the relative fluxes of the desorbed icy particles and the overall nebular gas will cause an excess of oxygen gas inside these snowlines (see Paper I for details). The presence of CO in a water ice environment rather than as pure ice moves the CO snowline significantly inward by $\sim 70\%$. Taken together, disk dynamics and ice morphology move the CO snowline inward by a factor of ~ 7 .

Here we use the model of Section 5.2 to estimate the movement of the CO and N₂ snowlines for different grain morphologies in a viscous disk. Figure 5.4 shows the H₂O, CO₂ and CO snowline locations for particles with initial sizes $\sim 0.05 \text{ cm} \lesssim s \lesssim 7 \text{ m}$ as well as estimates for the C/O ratio in gas and dust in a viscous disk, with the CO snowline calculated under different grain morphologies as noted above. We assume there is no carbon in the form of CH₄. The true snowline for particles that desorb outside the static snowline is the static snowline itself, hence desorbing par-

ticles with $s < 0.05$ cm do not form true snowlines. If the CO binding environment is known, the CO snowline moves inward by up to ~ 50 % compared to a static disk for each case (pure and water dominated ices) due to disk dynamics. The full range of potential CO snowlines taking into account both ice morphology and disk dynamics span ~ 8.7 AU to ~ 61 AU, which is a factor of ~ 7 difference. This implies that gas phase C/O ratios of order unity may be reached in the giant planet forming zone, and the CO snowline may be inside 10 AU for certain disk parameters.

Figure 5.5 shows the H_2O , CO_2 , CO and N_2 snowline locations in a viscous disk for the same range of initial particle sizes as in Figure 5.4, and with the CO and N_2 snowlines calculated assuming different grain morphologies as explained above, as well as estimates for the N/O ratio throughout the disk. For simplicity, we assume that all nitrogen is the form of N_2 . This choice is justified since the presence of some NH_3 only moderately changes the N/O ratio (see Figure 5.3), and since we are primarily interested in the N_2 snowline locations rather than exact values for the N/O ratio. The innermost N_2 snowlines in the viscous disk, created by particles with $s \sim 7$ m for our fiducial model, are located at $r_{\text{N}_2, \text{pure}} \approx 42$ AU for N_2 as pure ice and at $r_{\text{N}_2, \text{water}} \approx 11$ AU for N_2 in water dominated ices. Thus for each case (pure versus water dominated ices), the N_2 snowline moves inward by up to 50% due to disk dynamics. By taking into account both ice morphology and disk dynamics, the full range of potential N_2 snowlines span ~ 11 to ~ 79 AU, which is a factor of ~ 7 difference. Similarly to the case for CO, the N_2 snowline may be close to 10 AU for certain disk models.

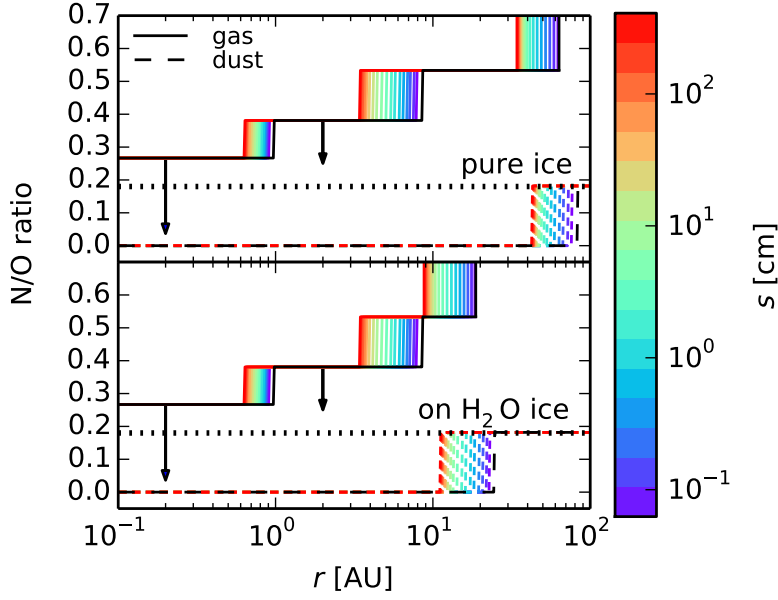


Figure 5.5: N/O ratio estimates in gas (solid lines) and dust (dashed lines) as function of semimajor axis in a viscous disk, for CO and N₂ as pure ices (top panel) or as water dominated ices (bottom panel). The H₂O, CO₂, CO and N₂ snowlines are shown for particles with initial sizes $\sim 0.05 \text{ cm} \lesssim s \lesssim 7 \text{ m}$ as indicated by the color bar. The N/O ratio in a static disk (black lines) is shown for comparison. The arrows show that the N/O ratio in gas will decrease inside the H₂O and CO₂ snowlines in the viscous disk, as the relative fluxes of the desorbed icy particles and the overall nebular gas will cause an excess of oxygen gas inside these snowlines (see Paper I for details). Radial drift and gas accretion move the N₂ snowline inward by up to $\sim 50\%$ compared to a static disk. The presence of N₂ in a water ice environment rather than as pure ice moves the N₂ snowline significantly inward by $\sim 70\%$. Taken together, disk dynamics and ice morphology move the N₂ snowline inward by a factor of ~ 7 . The results of an enhanced gas-phase N/O ratio between the H₂O and CO snowlines compared to its average value, and of highly elevated N/O ratios in gas between the CO and N₂ snowlines (see Figure 5.3), are preserved.

5.4 DISCUSSION

This study shows that the gas-phase N/O ratio in protoplanetary disks is considerably enhanced throughout most of the disk midplane compared to its average value. As demonstrated in Figure 5.6, the gaseous N/O ratio is enhanced by a factor of two beyond the H₂O snowline, by more than a factor of three between the CO₂ and CO snowlines, and by several orders of magnitude between the CO and N₂ snowlines. Thus constraining the N/O ratio in a giant planet atmosphere could be used

to trace its formation origins.

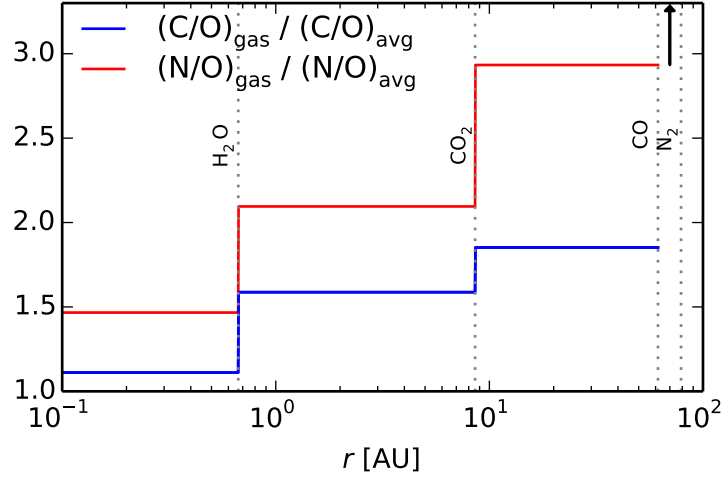


Figure 5.6: Gas phase C/O (blue curve) and N/O (red curve) ratios divided by the average C/O and N/O ratio in a static disk, assuming CO and N₂ are pure ices, and there is no CH₄ or NH₃. The dashed vertical lines mark the H₂O, CO₂, CO and N₂ snowlines. The arrow indicates that the N/O ratio is enhanced by orders of magnitude compared to its average value between the CO and N₂ snowlines. The gaseous N/O ratio is enhanced throughout most of the disk, and more enhanced than the C/O ratio.

Theoretical models of the magnitude and role of N/O (and N/C) ratios in exoplanet atmospheres are needed in order to use these ratios as probes for a planet’s formation location. Models that explore the effect of varying the C/O ratio in exoplanet atmospheres exist in literature, and they display a large and observable effect on gas giant envelope chemistry (Lodders 2009, Mollière et al. 2015). However, no similar model explorations exist for the effect of N/O and C/N/O ratios, and both are needed to exploit this potential constraint. Given the existence of such theoretical models, measurements of the N/O ratio in planetary envelopes may be possible to infer from atmospheric compositions of nitrogen versus carbon and oxygen bearing species. Nitrogen carriers have not been targeted so far due to lack of instrument sensitivity, but such observations and detections are likely in the near future with the advent of JWST (e.g., NH₃, Greene et al. 2016). The N/O ratio enhancement is larger than that of the gas phase C/O ratio throughout most of the disk. Thus mea-

measurements of an enhanced C/O ratio in an exoplanet atmosphere could be corroborated (disproved) by measurements of enhanced (non-enhanced) N/O ratios. Moreover, Figure 5.6 shows that giant planets that have formed in situ between the H₂O and CO snowlines are expected to present elevated both C/O and N/O ratios in their atmospheres, whereas planets between the CO and N₂ snowlines will have a highly enhanced N/O ratio in their atmospheres, but not C/O.

Due to disk dynamics and ice morphology, the locations of the CO and N₂ snowlines, and thus the disk regions with highly elevated gas phase N/O and C/O ratios, are uncertain and may span tens of AU. Both ice morphologies discussed in this study, pure and water dominated ices, are plausible in protoplanetary disks and depend on whether H₂O and CO ices formed on similar timescales or successively (e.g., [Garrod & Pauly 2011](#)). Observations of protostellar cores show that a large fraction of CO is bound in a pure ice multilayer ([Pontoppidan et al. 2003](#)), but theoretical models also suggest an icy mantle structure where CO resides on a H₂O ice layer (e.g., [Collings et al. 2003](#)). One can also imagine a scenario where CO is in a water binding environment and N₂ is not. This could be attributed to the fact that H₂O may bind preferentially to CO than N₂, since both H₂O and CO are polar molecules while N₂ is not. It is also possible for N₂ ices to form later than CO (e.g., [Pagani et al. 2012](#)), and thus be deposited on the outer layers of the icy mantles which are typically water poor (e.g., [Garrod & Pauly 2011](#)). The impact of the ice environment on the snowline location is much smaller in the case of CO₂ and NH₃, as their binding energies and behavior are closer to that of H₂O. No detailed measurements for the CH₄ binding energy in a water environment exist so far, but due to its low desorption temperature a similar behavior to that of CO and N₂ would be expected. While the presence of some carbon in the form of CH₄ only modestly affects our results, CH₄ may become important in disks where a large fraction of the CO abundance has been converted into hydrocarbons (e.g., [Du et al. 2015](#)).

Changes in stellar luminosity (e.g., [Kennedy et al. 2006](#)) and gas mass accretion rate (e.g., [Chambers 2009](#)), as well as the evolution of icy dust particles due to grain growth and fragmentation (e.g.,

Birnstiel et al. 2012), may introduce additional uncertainties in the snowline locations, and thus the C/N/O ratios. Given the number of uncertainties in snowline locations, detections of snowlines in a sample of disks at different evolutionary stages are needed to provide observational constraints on the relative importance of ice morphology and disk dynamics in setting snowline locations. The uncertainties in snowline locations caused by disk dynamics, ice morphology, and other effects outlined above can be resolved in extreme cases, such as a detection of a CO snowline at a temperature corresponding to pure CO ice desorption in a static disk (e.g., Qi et al. 2013 at ~ 17 K) or CO desorption from a water dominated ice in a dynamic disk. In intermediate cases it is more difficult to resolve the relative importance of ice morphology and disk dynamics. For example, the CO snowline in HD 163296 is at a higher temperature of ~ 25 K (Qi et al. 2015), which could be caused either by CO being in a water dominated environment or by dynamical effects that push the CO snowline inward. Detections of multiple snowlines in the same disk could potentially break this degeneracy.

Uncertainties in snowline locations of this magnitude also affect interpretations of Solar system observations. Recent measurements of nitrogen abundance in comet 67P/Churyumov-Gerasimenko found a N_2/CO ratio $\sim 10^{-3}$ (Rubin et al. 2015). A low N_2/CO ratio is consistent with comets having formed inside the N_2 snowline where N_2 is still in the gas phase. Theoretical models suggest that Jupiter-family comets, such as 67P, originate from the Kuiper belt (Duncan & Levison 1997; but see Rubin et al. 2015 for alternative formation scenarios for 67P). It is thus possible, in principle, to use measurements of the N_2 abundance in Jupiter-family comets to determine where the N_2 snowline was located in our Solar system. However due to the uncertainty in the calculated location of the N_2 snowline (see Section 5.3.3), more detailed modeling is needed.

5.5 SUMMARY

In this paper we explore the role of icy grain morphology and disk dynamics on the snowline locations of major volatile carrier molecules and the C/N/O ratios in protoplanetary disks. We en-

hance the coupled drift-desorption model developed in [Piso et al. \(2015\)](#) by adding more carbon- and nitrogen-bearing species into our framework, and by considering different binding ice environments. Our results can be summarized as follows:

1. Due to the high volatility of N_2 , the gaseous N/O ratio outside the H_2O snowline is enhanced by a factor of two compared to its average value, by more than a factor of three between the CO_2 and CO snowlines, and by many orders of magnitude between the CO and N_2 snowlines due to the complete depletion of oxygen gas in this region. This enhancement is more pronounced than in the case of the gas-phase C/O ratio, which is increased by at most a factor of two compared to the stellar value.
2. The effect of CH_4 and NH_3 on the C/O and N/O ratios is small, even when we consider the maximum observed CH_4 and NH_3 abundances in protostellar cores. In this scenario, the gas phase C/O ratio increases by 8% between the CO_2 and CH_4 snowlines, and the gaseous N/O ratio decreases by 18% between the NH_3 and CO_2 snowlines. In both cases, large gas phase C/O and N/O ratios in the outer disk are preserved.
3. Grain composition sensitively affects the CO and N_2 snowline locations. If CO and N_2 reside in water dominated rather than pure ices, their snowlines move inward by up to $\sim 70\%$. This effect is separate from that of radial drift and viscous gas accretion, which also cause an inward movement of the CO and N_2 snowlines by up to $\sim 50\%$.
4. The locations of the CO and N_2 snowlines are uncertain when we consider both viscous versus static disks, and pure versus water dominated ices. The snowlines in a viscous disk with CO or N_2 in a water environment are by up to a factor of ~ 7 closer to the host star than in a static disk with CO or N_2 as pure ices.

Our results have direct consequences for the composition of nascent giant planets. The considerable inward movement of the CO and N₂ snowlines due to the ice grains being water dominated rather than pure ices implies that giant planets with high C/O and/or N/O ratios in their atmospheres may form closer in than previously predicted by theoretical models. Moreover, our model shows that wide separation gas giants may have an excess of nitrogen in their envelopes, which may be used to trace their origins.

6

Summary and Future Directions

In this thesis, I have calculated the minimum core mass required to form wide-separation gas giants at different disk locations, and for different equations of state of the nebular gas and dust opacities. I have also determined how disk dynamics and volatile abundance and morphology affect volatile snowline locations, the C/N/O ratios across the disk, and therefore the compositions of nascent giant planets. My results are summarized in Sections 6.1 and 6.2, and I present directions for future work in Section 6.3.

6.1 MINIMUM CORE MASSES FOR GIANT PLANET FORMATION

In Chapters 2 and 3, I determined the minimum core mass M_{crit} required to form a gas giant at distances between 5 and 100 AU from the host star, motivated by the fact that standard core accretion models cannot explain the formation of giant planets in the outer disk. This minimum applies when the solid cores are no longer accreting solids, since any additional heating due to planetesimal accretion would heat up the core's atmosphere, inhibit its ability to cool and contract, and therefore increase the critical core mass. I thus considered atmospheres accreting around fully formed cores and undergoing Kelvin-Helmholtz contraction. In Chapter 2, I developed a quasi-static atmospheric evolution model by generating a series of static atmospheric profiles that are then connected temporally through a cooling equation. I considered an envelope structure consisting of an inner convective region and an outer radiative layer, and assumed a constant luminosity in the outer radiative region. I demonstrated that this is a valid approximation for my parameter space of interest. For an ideal gas polytrope and standard interstellar (ISM) opacities, I have found that M_{crit} decreases with semimajor axis from $\sim 8.5M_{\oplus}$ at 5 AU to $\sim 3.5M_{\oplus}$ at 100 AU. My results are lower than the typically quoted value of $M_{\text{crit}} \sim 10M_{\oplus}$ (e.g., [Rafikov 2006](#)), even in the more inner parts of the disk.

To obtain more robust quantitative results, in Chapter 3 I expanded the model developed in Chapter 2 by considering a realistic equation of state (EOS) for the nebular gas and realistic dust opacities that take into account grain growth. I parametrized the EOS through the adiabatic gradient ∇_{ad} (defined in Chapter 2), as ∇_{ad} relates the gas pressure, temperature and density. While for an ideal gas EOS ∇_{ad} is constant, non-ideal EOS effects cause features in the adiabatic gradient that change the atmospheric structure. At high temperatures, molecular hydrogen dissociates, while at low-temperatures the rotational states of the hydrogen molecule are only partially excited so it no longer behaves like an ideal gas, due to the existence of H_2 in two spin isomeric forms, ortho- and

parahydrogen. Both of these effects increase M_{crit} by a factor of ~ 2 compared to the ideal gas. In contrast, grain growth opacities decrease M_{crit} dramatically. By taking these two competing effects together, I calculate $M_{\text{crit}} \sim 8M_{\oplus}$ at 5 AU, decreasing to $\sim 5M_{\oplus}$ at 100 AU. While my atmospheric model is not equipped to calculate the critical core mass when grain coagulation is taken into account, I have demonstrated that grain growth with coagulation may decrease M_{crit} by up to one order of magnitude; M_{crit} may be as low as $1M_{\oplus}$. My study thus clearly challenges previous claims that core accretion cannot operate in the outer disk, reopening the case for in situ formation of wide separation gas giants.

6.2 THE ROLE OF DISK DYNAMICS AND ICE MORPHOLOGY ON SNOWLINE LOCATIONS AND THE C/N/O RATIOS

In Chapters 4 and 5, I determined the effect of disk dynamics and ice morphology on the C/N/O ratio in active disks, which has direct implications on gas giant compositions. This study was motivated by the fact that the locations of volatile snowlines in protoplanetary disks are a defining feature of both gas giant and disk chemistry, as they provide vital information about the abundance of these molecules in gas and dust throughout the disk. In Chapter 4, I expanded the model of [Öberg et al. \(2011b\)](#) by considering the effect of disk dynamics on the snowline locations of the main carbon and oxygen carriers, i.e. H_2O , CO_2 and CO , and thus on the C/O ratio in dust and gas throughout the disk. I studied the effect of radial drift of solids and viscous gas accretion onto the central star on snowline locations by developing a semi-analytical model, which I applied to three different disks in increasing order of complexity. I applied my model for a range of initial particle sizes and calculated how drift and gas accretion affect their desorption location. I have found that there is a range of particle sizes, $0.05 \text{ cm} \lesssim s \lesssim 7 \text{ m}$ for my particular parameters, that desorb almost instantaneously and at a fixed particle-size dependent location from the central star, regardless of their initial position. Based on this information, I calculated the H_2O , CO_2 and CO snowline locations for different par-

ticle sizes in this range, and made estimates for the C/O ratio throughout the disk. I have found that the snowlines move inward as the particle size increases, and may differ by up to a factor of ~ 2 due to drift and gas accretion compared to a static disk, which does not experience any dynamical processes. This variation in snowline locations is significant, and has important consequences for the compositions of gas giants forming in situ.

In Chapter 5, I expanded the model developed in Chapter 4 by considering additional volatiles, chemical abundances, and ice morphologies. As nitrogen is highly abundant in the Solar System and primarily found as N_2 , I added nitrogen bearing species such as N_2 and NH_3 to my model, as well as hydrocarbons (specifically, CH_4). Motivated by laboratory experiments (e.g., [Fayolle et al. 2016](#)) that find significantly different binding energies for CO and N_2 depending on the ice environment in which they reside (pure versus water dominated ices), I calculated the CO and N_2 snowlines for both scenarios. I calculated the N/O ratio in static disks and found that it is highly enhanced compared to the stellar value: by a factor of ~ 2 between the H_2O and CO_2 snowlines, by more than a factor of 3 between the CO_2 and CO snowlines, and by many orders of magnitude between the CO and N_2 snowlines, where oxygen gas is depleted. Thus I expect wide-separation giants to have an excess of nitrogen in their atmospheres, which may be used to trace their formation origins. I have also found that the binding environment has a large effect on the CO and N_2 snowline locations and may change them by factors of 3-4, both for static and dynamic disks. Thus by considering the combined effect of disk dynamics and ice morphology, the CO and N_2 snowline locations may change by up to a factor of ~ 7 , and may span 11-79 AU for N_2 in my disk model. This large uncertainty in snowline locations means that observations that anchor snowline locations at different stages of planet formation are key to develop C/N/O ratios as a probe of planet formation zones.

6.3 FUTURE DIRECTIONS

My work has made important strides in our understudying of disk and planet compositions and the tight link between the two, as well as the effect of disk dynamics and chemistry on disk and planet compositions. As a first step, I plan to expand my work by considering the effect of diffusion on the C/N/O ratios in viscous steady-state disks. Similarly to the model of [Owen \(2014\)](#), I will develop a simplified method to estimate the abundance of different volatiles at various disk locations, and thus their effect on the C/N/O ratio both in static and dynamic disks.

Through analytical and numerical calculations, I will explore a range of dynamical processes that may affect snowline locations and the distribution of volatiles in disks, expanding and generalizing the framework developed in Chapter 4 and 5. Such effects include particle growth and fragmentation, as well as variations in the gas mass accretion rate and stellar luminosity.

The complexity of disk chemistry means that coupling it with dynamical processes, while necessary, is non-trivial. As a next step I will thus couple the dynamical framework outlined above with time-dependent chemical models of increasing complexity, informed by results from state-of-the-art disk chemistry models (that can only be run on static disks). By having a better understudying on how disk chemistry and dynamics affect the composition of nascent, and eventually mature planets, my work may provide essential context for characterizing the gas giants that instruments such as JWST and the TESS will one day discover.



Derivation of the Global Energy Equation

To derive the global energy equation (2.16) for an embedded protoplanet, we generalize the analogous calculations in stellar structure theory, e.g. in §4.3 of [Kippenhahn & Weigert \(1990\)](#). For our problem, we add the effects of finite core radius, surface pressure and mass accretion. We start with the local energy equation (2.10d), whose more natural form in Lagrangian (mass) coordinates is $\partial L / \partial m = \epsilon - T \partial S / \partial t$. Integrating from the core to a higher shell with enclosed mass M gives:

$$L - L_c = \int_{M_c}^M \frac{\partial L}{\partial m} dm \tag{A.1a}$$

$$= \int_{M_c}^M \left(\epsilon - T \frac{\partial S}{\partial t} \right) dm \tag{A.1b}$$

$$= \Gamma - \int_{M_c}^M \frac{\partial u}{\partial t} dm + \int_{M_c}^M \frac{P}{\rho^2} \frac{\partial \rho}{\partial t} dm, \tag{A.1c}$$

with $\Gamma = \int \epsilon dm$ the integral of the direct heating rate, and applying the first law of thermodynamics in the final step.

The global energy equation is derived by eliminating the partial time derivatives in Equation (A.1c), which are performed at a fixed mass, in favor of total time derivatives, denoted with overdots. For instance, the surface radius R of the shell with enclosed mass M evolves as

$$\dot{R} = \frac{\partial R}{\partial t} + \frac{\dot{M}}{4\pi R^2 \rho_M}, \quad (\text{A.2})$$

where $\partial R/\partial t$ gives the Lagrangian contraction of the “original” shell, and mass accretion through the upper boundary at rate \dot{M} also changes the shell location. Similarly, the volume $V = (4\pi/3)R^3$ and pressure at the outer shell evolve as

$$\dot{V}_M = \frac{\partial V_M}{\partial t} + \frac{\dot{M}}{\rho_M} \quad (\text{A.3a})$$

$$\dot{P}_M = \frac{\partial P_M}{\partial t} + \frac{\partial P_M}{\partial m} \dot{M} = \frac{\partial P_M}{\partial t} - \frac{GM}{4\pi R^4} \dot{M}. \quad (\text{A.3b})$$

This derivation holds the core mass and radius fixed, $\dot{M}_c = \dot{R}_c = 0$. Therefore, the core pressure satisfies

$$\dot{P}_c = \partial P_c / \partial t. \quad (\text{A.4})$$

The internal energy integral follows simply from Leibniz’s rule as

$$\int_{M_c}^{M(t)} \frac{\partial u}{\partial t} dm = \dot{U} - \dot{M} u_M. \quad (\text{A.5})$$

To make further progress, we use the virial theorem:

$$E_G = -3 \int_{M_c}^M \frac{P}{\rho} dm + 4\pi(R^3 P_M - R_c^3 P_c), \quad (\text{A.6})$$

which follows from Equations (2.10a), (2.10b) and (2.14) by integrating hydrostatic balance in Lagrangian coordinates. As an aside, the integral in equation (A.6) can be evaluated for a polytropic EOS to give simple expressions for the total energy:

$$E = (1 - \zeta)U + 4\pi(R^3 P_M - R_c^3 P_c) \quad (\text{A.7a})$$

$$= \frac{\zeta - 1}{\zeta} E_G + \frac{4\pi}{\zeta} (R^3 P_M - R_c^3 P_c), \quad (\text{A.7b})$$

where $\zeta \equiv 3(\gamma - 1)$. We will not make this assumption and will keep the EOS general.

To express the work integral, i.e. the final term in Equation (A.1c), in terms of changes to gravitational energy, we first take the time derivative of Equation (A.6):

$$\dot{E}_G = 3 \int_{M_c}^M \frac{P}{\rho^2} \frac{\partial \rho}{\partial t} dm - 3 \int_{M_c}^M \frac{\partial P}{\partial t} \frac{dm}{\rho} - 3 \frac{P_M}{\rho_M} \dot{M} + 3 \dot{P}_M V_M - 3 \dot{P}_c V_c + 3 P_M \dot{V}_M. \quad (\text{A.8})$$

The first integral in Equation (A.8) is the one we want, but the second one must be eliminated. The time derivative of Equation (2.14) (times four) gives

$$4\dot{E}_G = -4 \frac{GM\dot{M}}{R} + 4 \int_{M_c}^M \frac{Gm}{r^2} \frac{\partial r}{\partial t} dm \quad (\text{A.9a})$$

$$= -4 \frac{GM\dot{M}}{R} + 4\pi \int_{M_c}^M r^3 \frac{\partial}{\partial m} \frac{\partial P}{\partial t} dm \quad (\text{A.9b})$$

$$= -4 \frac{GM\dot{M}}{R} - 3 \int_{M_c}^M \frac{\partial P}{\partial t} \frac{dm}{\rho} + 3V_M \frac{\partial P_M}{\partial t} - 3V_c \frac{\partial P_c}{\partial t}, \quad (\text{A.9c})$$

where Equations (A.9b) and (A.9c) use hydrostatic balance and integration by parts.

Subtracting Equations (A.5) and (A.9c) and rearranging terms with the help of Equations (A.2), (A.3) and (A.4) gives

$$\int_{M_c}^M \frac{P}{\rho^2} \frac{\partial \rho}{\partial t} dm = -\dot{E}_G - \frac{GM\dot{M}}{R} - P_M \frac{\partial V_M}{\partial t}. \quad (\text{A.10})$$

Combining Equations (A.1c), (A.5) and (A.10), we reproduce Equation (2.16) with the accreted specific energy $e_M \equiv u_M - GM/R$.

B

Analytic Cooling Model Details

B.O.1 ISOTHERMAL ATMOSPHERE

We consider the structure of a non-self-gravitating, isothermal atmosphere that extends outward from the radiative-convective boundary (RCB) and matches onto the disk density, ρ_d , at a distance $r_{\text{fit}} = n_{\text{fit}} R_B$, where R_B is the Bondi radius defined in equation (2.7). From equation (2.10b) the resulting density profile is

$$\rho = \rho_d \exp\left(\frac{R_B}{r} - \frac{1}{n_{\text{fit}}}\right) \approx \rho_d \exp\left(\frac{R_B}{r}\right), \quad (\text{B.1})$$

where the approximate inequality is valid deep inside the atmosphere ($r \ll R_B$) for any $n_{\text{fit}} \gtrsim 1$. However, the choice of boundary condition does have an order unity effect on the density near the

Bondi radius.

The mass of the atmosphere is determined by integrating equation (2.10a) from the RCB to the Bondi radius using the density profile (B.1) and can be approximated as

$$M_{\text{iso}} \approx 4\pi\rho_{\text{d}} \frac{R_{\text{RCB}}^4}{R_{\text{B}}} e^{R_{\text{B}}/R_{\text{RCB}}} = 4\pi\rho_{\text{RCB}} \frac{R_{\text{RCB}}^4}{R_{\text{B}}}, \quad (\text{B.2})$$

with ρ_{RCB} the density at the RCB. This result is the leading order term in a series expansion. By comparing the expression above and Equation (2.26) under the assumption that $R_{\text{RCB}} \ll R_{\text{B}}$, we see that the mass of the outer radiative region (which is nearly isothermal) is negligible when compared with the atmosphere mass in the convective layer, as stated in Section 2.3.

B.O.2 TEMPERATURE AND PRESSURE CORRECTIONS AT THE RADIATIVE-CONVECTIVE BOUNDARY

We estimate the temperature and pressure corrections at the RCB due to the fact that the radiative region is not purely isothermal. From equation (2.11), we express the radiative lapse rate

$$\nabla_{\text{rad}} = \frac{3\kappa P}{64\pi GM\sigma T^4} L = \nabla_{\text{d}} \frac{P/P_{\text{d}}}{(T/T_{\text{d}})^{4-\beta}}, \quad (\text{B.3})$$

where the second equality follows from the opacity law (2.5) and ∇_{d} is the radiative temperature gradient at the disk:

$$\nabla_{\text{d}} \equiv \frac{3\kappa(T_{\text{d}})P_{\text{d}}}{64\pi GM\sigma T_{\text{d}}^4} L. \quad (\text{B.4})$$

Here M is the total planet mass. Since our analytic model neglects self-gravity, $M = M_{\text{c}}$ and therefore ∇_{d} is constant. From equation (B.3) and $\nabla_{\text{rad}} = d \ln T / d \ln P$, the temperature profile in the

radiative region integrates to

$$\left(\frac{T}{T_d}\right)^{4-\beta} - 1 = \frac{\nabla_d}{\nabla_\infty} \left(\frac{P}{P_d} - 1\right), \quad (\text{B.5})$$

where $\nabla_\infty = 1/(4 - \beta)$ is the radiative temperature gradient for $T, P \rightarrow \infty$. Applying Equations (B.3) and (B.5) at the RCB (where $\nabla_{\text{rad}} = \nabla_{\text{ad}}$) under the assumption that $P_{\text{RCB}} \gg P_d$ results in $T_{\text{RCB}} = \chi T_d$ as in Equation (2.19a), with χ defined in Equation (2.20).

The pressure at the RCB follows from Equations (B.5) and (2.19a) as

$$\frac{P_{\text{RCB}}}{P_d} \simeq \frac{\nabla_{\text{ad}}/\nabla_d}{1 - \nabla_{\text{ad}}/\nabla_\infty}. \quad (\text{B.6})$$

We can eliminate ∇_d from equation (B.6) to obtain a relation between temperature and pressure in the radiative zone as a function of the RCB pressure P_{RCB} . From Equation (B.5), it follows that

$$\frac{T}{T_d} = \left[1 + \frac{1}{\frac{\nabla_\infty}{\nabla_{\text{ad}}} - 1} \left(\frac{P}{P_{\text{RCB}}} - \frac{P_d}{P_{\text{RCB}}}\right)\right]^{\frac{1}{4-\beta}}. \quad (\text{B.7})$$

We can then determine the RCB radius R_{RCB} from Equation (2.10b) as

$$\frac{R_B}{R_{\text{RCB}}} = \int_{P_d}^{P_{\text{RCB}}} \frac{T}{T_d} \frac{dP}{P}. \quad (\text{B.8})$$

Evaluating the integral leads to

$$\frac{R_B}{r_{\text{RCB}}} = \ln \left(\frac{P_{\text{RCB}}}{P_d}\right) - \ln \theta, \quad (\text{B.9})$$

with an extra correction term $\theta < 1$, when compared to an isothermal atmosphere (see Equation B.1). From this we arrive at the relation between P_{RCB} and P_d given by Equation (2.19b). As op-

posed from the temperature correction factor χ , an analytic expression for θ cannot be obtained. Estimates for χ and θ for different values of the exponent β in the opacity law (2.5) are presented in Table 1.

B.o.3 THE OPACITY EFFECT

A lower opacity decreases the critical core mass. Reducing the opacity by a factor of one hundred results in a critical core mass one order of magnitude lower than in the standard ISM case, for our analytic model. The reduction is not as strong as the nominal scaling would imply, $0.01^{3/5} \approx 0.06$, because ξ increases.

Even with significantly lower opacities, radiative diffusion remains a good approximation at the RCB. For $\beta = 2$, we estimate the optical depth as

$$\tau_{\text{RCB}} \sim \frac{\kappa_{\text{RCB}} P_{\text{RCB}}}{g} \sim 7 \times 10^4 \frac{F_T^4 F_\kappa}{\left(\frac{m_{\text{c}\oplus}}{10}\right) \left(\frac{a_\oplus}{10}\right)^{\frac{12}{7}}}, \quad (\text{B.10})$$

where $P_{\text{RCB}} \sim P_M$ for a self-gravitating atmosphere and $g \sim GM_c/R_B^2$, with both approximations good to within the order unity factor ξ . We see that $\tau_{\text{RCB}} \gg 1$ even for $F_\kappa \lesssim 0.01$ out to very wide separations, hence the atmosphere remains optically thick at the RCB.

B.o.4 SURFACE TERMS

In this section we check the relevance of the neglected surface terms in Equation (2.16). We first show that accretion energy is only a small correction at the RCB, which is where we apply our cooling model. A rough comparison (ignoring terms of order ξ) of accretion luminosity vs. \dot{E} gives

$$\frac{GM\dot{M}}{R\dot{E}} = \frac{GM}{R} \frac{dM}{dE} \sim \frac{GM_c^2}{R_B E} \frac{P_{\text{RCB}}}{P_M} \sim \sqrt{\frac{R_c}{R_B}} \ll 1, \quad (\text{B.11})$$

Table B.1. Parameters Describing Structure of Radiative Zone.

$\gamma = 7/5$ ($\nabla_{\text{ad}} = 2/7$)					
β	1/2	3/4	1	3/2	2
∇_{∞}	2/7 ^a	4/13	1/3	2/5	1/2
χ	...	2.25245	1.91293	1.65054	1.52753
θ	...	0.145032	0.285824	0.456333	0.556069

^aSince $\nabla_{\text{ad}} = \nabla_{\infty}$ there is no convective transition at depth for this case.

where we assume $P_{\text{RCB}} \sim P_M$ for a massive atmosphere. Accretion energy at the protoplanetary surface is thus very weak for marginally self-gravitating atmospheres, and even weaker for lower mass atmospheres. A similar scaling analysis shows that the work term $P_M \partial V_M / \partial t$ is similarly weak. Nevertheless, our numerical calculations include these surface terms in a more realistic and complete model of self-gravitating atmospheres.



Equation of State Table Extension

In this study we consider atmosphere growth in the outer parts of protoplanetary disks ($5 < a < 100$ AU), where temperature and pressure drop to as little as $T \sim 20$ K and $P \sim 4 \times 10^{-6}$ dyn cm $^{-2}$ for our fiducial disk model (see equations 3.1b and 3.1c). We model the nebular gas using the EOS tables of [Saumon et al. \(1995\)](#). However, these tables only cover the relatively high temperature and pressure ranges $2.1 < \log_{10} T(\text{K}) < 7.06$ and $4.0 < \log_{10} P(\text{dyn cm}^{-2}) < 19.0$. We thus need to extend the tables to lower T and P . We calculate ∇_{ad} for

$$1.0 < \log_{10} T < 2.1 \tag{C.1}$$

$$-5.4 < \log_{10} P < 4.0 \tag{C.2}$$

using the following method.

C.o.5 HYDROGEN

Following Kittel et al. (1981), we calculate ∇_{ad} from the partition function for the internal energy of a system of hydrogen gas molecules (see also D’Angelo & Bodenheimer 2013 for EOS calculations that take into account hydrogen isomers). We begin by writing the partition function Z of a gas molecule of mass m as the product of the partition functions associated with each type of internal energy:

$$Z = Z_t Z_r Z_v, \quad (\text{C.3})$$

where Z_t , Z_r , Z_v are associated with translation, rotation, and vibration, respectively.*

In the classical limit, the molecule’s center of mass motion generates

$$Z_t = (mk_B T / 2\pi\hbar^2)^{3/2} V, \quad (\text{C.4})$$

where T and V are the gas temperature and volume, respectively, and \hbar is the reduced Planck constant. The rotational partition function is

$$Z_r = \sum_{j=0}^{\infty} (2j+1) \exp \left[\frac{-j(j+1)\Theta_r}{T} \right], \quad (\text{C.5})$$

where the characteristic temperature for rotational motion $\Theta_r \approx 85$ K for hydrogen. However, molecular hydrogen occurs in two isomeric forms: parahydrogen with a symmetric (even) rotational wavefunction, and orthohydrogen with an antisymmetric (odd) wavefunction (see Section 3.3). The

*We ignore electronic and nuclear excitation as they are only important at temperatures much higher than our regime of interest.

rotational partition functions for ortho- and parahydrogen are thus

$$Z_{r,\text{para}} = \sum_{j=0}^{\infty} \frac{1 + (-1)^j}{2} (2j + 1) \exp \left[-\frac{j(j+1)\Theta_r}{T} \right] \quad (\text{C.6})$$

and

$$Z_{r,\text{ortho}} = 3 \sum_{j=0}^{\infty} \frac{1 - (-1)^j}{2} (2j + 1) \exp \left[-\frac{j(j+1)\Theta_r}{T} \right] . \quad (\text{C.7})$$

The factor of 3 in Equation (C.7) accounts for the three-fold degeneracy of the ortho state.

In thermal equilibrium, the spin isomers have a combined partition function $Z_r = Z_{r,\text{ortho}} + Z_{r,\text{para}}$, which can be written

$$Z_r = \sum_{j=0}^{\infty} (2 - (-1)^j) (2j + 1) \exp \left[\frac{-j(j+1)\Theta_r}{T} \right] . \quad (\text{C.8})$$

For a fixed 3:1 ortho-to-para ratio, the combined partition function is $Z_r = Z_{r,\text{para}}^{1/4} Z_{r,\text{ortho}}^{3/4}$. In our range of temperatures of interest, we find that Z_r converges after about 25 terms in the series, for both the equilibrium and 3:1 cases.

Note that $Z_{r,\text{ortho}} \rightarrow 0$ and $Z_{r,\text{para}} \rightarrow 1$ as $T \rightarrow 0$. This is inconsistent with a fixed 3:1 ortho-to-para ratio, since $Z_{r,\text{ortho}} \rightarrow 0$ implies that there is no orthohydrogen in the system. [Boley et al. \(2007\)](#) and [D'Angelo & Bodenheimer \(2013\)](#) ensure that this requirement is not violated by using a normalized orthohydrogen partition function, $Z'_{r,\text{ortho}} = Z_{r,\text{ortho}} \exp(2\theta_r/T)$, which reduces the energy of the lowest rotational state for orthohydrogen from $2k_B\theta_r$ per molecule to zero. This decreases the total internal energy of the system by a constant factor, but does not change c_v , ∇_{ad} , or the relative internal energies of static atmospheric profiles, and therefore does not affect atmospheric evolution.

Finally, the partition function for vibrational motion is given by:

$$Z_v = [1 - \exp(\theta_v/T)]^{-1}, \quad (\text{C.9})$$

where the characteristic temperature for vibrational motion is $\theta_v \approx 6140$ K for hydrogen.

For a system of N particles of mass m , the partition function of the ensemble is $Z_N = (1/N!)Z^N$. Given Z_N as a function of (V, T) , the internal energy per mass, entropy per mass and specific heat capacity can be written as

$$u = \mathcal{R}T^2 \left(\frac{\partial \ln Z}{\partial T} \right)_V \quad (\text{C.10})$$

$$S = \mathcal{R} \ln Z + \frac{u}{T} - \frac{\mathcal{R}}{N} \ln N! \quad (\text{C.11})$$

$$c_V = \left(\frac{\partial u}{\partial T} \right)_V. \quad (\text{C.12})$$

Note that, following the convention of [Saumon et al. \(1995\)](#), we use S to denote entropy per mass ($[S] = \text{erg K}^{-1} \text{g}^{-1}$). Since $Z = Z_t Z_r Z_v$, we may write $u = u_t + u_r + u_v$ and $S = S_t + S_r + S_v$, where variables subscripted t , r , and v are the quantities corresponding to the individual translation, rotation and vibration partition functions, respectively. We include the term $\mathcal{R}/N \ln N!$ from Equation (C.11) in S_t .

In the temperature regime for which the rotational states of H_2 are selectively occupied, the total number of particles in the system is constant and we may use the ideal gas law, $P = \rho \mathcal{R}T$. With Equations (C.10), (C.11), and Stirling's approximation, $\ln N! \approx N \ln N - N$, the resulting entropy per mass due to translational motion is

$$S_t = \mathcal{R} \left[\frac{5}{2} \ln T - \ln P + \ln \left(\frac{(2\pi)^{3/2} \mathcal{R}^{5/2} m^4}{h^3} \right) + \frac{5}{2} \right] \quad (\text{C.13})$$

Equation (C.13) is known as the Sackur-Tetrode formula.

The internal energy per mass due to translational motion is given by:

$$u_t = \frac{3}{2}\mathcal{R}T \quad (\text{C.14})$$

Putting all of the above together, we can now evaluate the thermodynamic quantities needed to extend the [Saumon et al. \(1995\)](#) EOS tables to low temperatures and pressures.

1. Density. In the low temperature, low pressure regime, ρ is related to T and P by the ideal gas law.
2. Internal energy per mass. $u = u_t + u_r + u_v$, where u_t is given by Equation (C.14), and u_r and u_v are determined using Equations (C.8), (C.9) and (C.10) above.
3. Entropy per unit mass. Similarly, $S = S_t + S_r + S_v$, where S_t is given by Equation (C.13), and S_r and S_v can be determined from Equation (C.11) and the calculated expressions for u_r and u_v , respectively.
4. Entropy logarithmic derivatives. The logarithmic derivatives S_T and S_P are given by:

$$S_T = \left. \frac{\partial \ln S}{\partial \ln T} \right|_P \quad (\text{C.15})$$

and

$$S_P = \left. \frac{\partial \ln S}{\partial \ln P} \right|_T \quad (\text{C.16})$$

We calculate S_T and S_P through finite differencing.

5. Adiabatic gradient ∇_{ad} . The adiabatic gradient is defined as:

$$\nabla_{\text{ad}} = \left. \frac{\partial \ln T}{\partial \ln P} \right|_S = -\frac{S_P}{S_T} \quad (\text{C.17})$$

We evaluate ∇_{ad} from the tabulated values for S_T and S_P determined above. Figure C.1 shows a contour plot of ∇_{ad} as a function of temperature and pressure for the extended EOS table for hydrogen, assuming thermal equilibrium between the spin isomers. For the 3:1 ortho-to-para ratio, ∇_{ad} decreases continuously with T for $T \lesssim 200$ K, in contrast with the equilibrium case, in which ∇_{ad} sharply decreases, then increases as T goes down. Our extension is only valid for $T \lesssim 2000$ K, since it does not take into account hydrogen dissociation. We choose $T = 1500$ K as a conservative temperature cutoff. While we account for vibrational motion for completeness, its contribution is negligible in the temperature regime of interest. [Saumon et al. \(1995\)](#) do not compute the EOS at very high pressures, since hydrogen is solid or may form a Coulomb lattice in this regime, and thus their EOS treatment is no longer valid. While the boundaries of the region in which the free-energy EOS treatment fails can be determined from fundamental thermodynamic constraints, such calculations are not the object of this work. Instead, we choose as boundary a constant entropy curve ($\log(S) = 8.4$) above the region in which the [Saumon et al. \(1995\)](#) model fails. The expressions derived above are sufficient to give good results for the colored regions of the extended map, which fully cover the temperature and pressures ranges required by our models.

C.o.6 HELIUM

We extend the helium EOS tables based on a similar procedure. Since helium is primarily neutral and atomic at low temperatures and pressures, we treat it as an ideal monoatomic gas and only take into account the translational component of the partition function (C.4). Figure C.2 shows ∇_{ad} as a function of temperature and pressure for the extended EOS table.

Lastly, we combine Figures C.1 and C.2 to obtain EOS tables for a hydrogen-helium mixture using the procedure described in [Saumon et al. \(1995\)](#). Figure 3.1 displays results for helium mass frac-

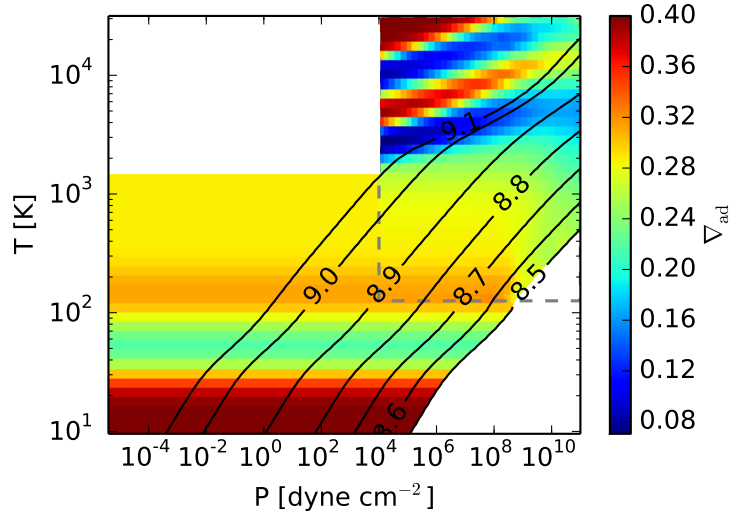


Figure C.1: Contour plot of the hydrogen adiabatic gradient ∇_{ad} as a function of gas temperature and pressure. The upper right rectangle encloses the region described by the original [Saumon et al. \(1995\)](#) EOS tables, while the rest of the plot is our extension to lower temperatures and pressures for an equilibrium mixture of ortho- and parahydrogen. The black curves represent constant entropy adiabats with labels $\log_{10}(S)$, where $S [\text{erg K}^{-1} \text{g}^{-1}]$ is the absolute entropy per unit mass. At high temperatures, hydrogen dissociates and ionizes, while at low temperatures the rotational states of the hydrogen molecule are only partially excited and it no longer behaves like an ideal diatomic gas. Regions in which the EOS is invalid or has not been computed are masked in white (see text).

tion $Y = 0.3$.

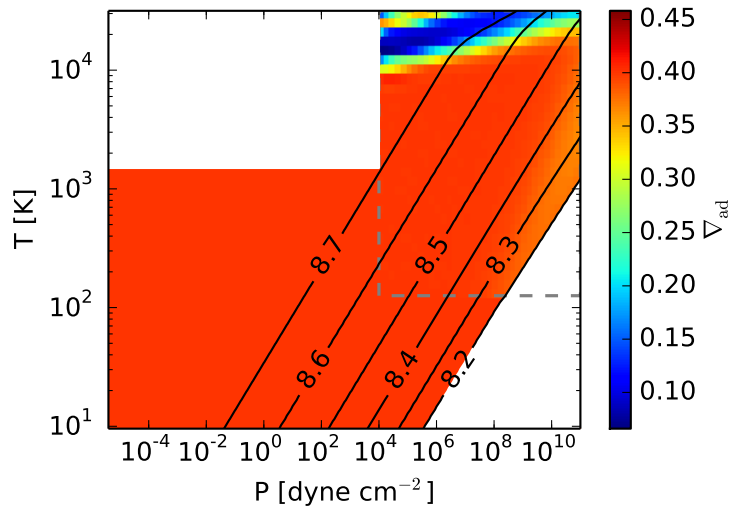


Figure C.2: Same as Figure C.1 but for pure helium. Helium ionizes at $T \gtrsim 10,000$ K, but behaves as an ideal monatomic gas otherwise. We choose $T = 7,000$ K as a conservative temperature cutoff above which our extension is no longer valid (masked in white). The EOS has not been computed in the lower-right region of the plot (see text).

D

Adiabatic Gradient Variations

D.0.7 ADIABATIC GRADIENT DURING PARTIAL DISSOCIATION

The total internal energy of a partially dissociated gas includes contributions from the individual internal energies of the molecules and atoms, as well as from the dissociation energy. The dissociation energy depends on the dissociation fraction x (i.e., the fraction of molecules that have dissociated), which can be found from the Saha equation (see e.g., [Kippenhahn & Weigert 1990](#), Chapter 14) as a function of temperature and density,

$$\frac{x^2}{1-x} \propto \frac{T^{3/2}}{\rho} e^{-\chi/k_B T}, \quad (\text{D.1})$$

where $\chi=4.48$ eV is the dissociation energy for molecular hydrogen ([Blanksby & Ellison 2003](#)).

The above also holds true for ionization, with the dissociation energy replaced by ionization energy $\chi = 13.6 \text{ eV}$ for atomic hydrogen (Mandl 1989). From the Saha equation one can find an expression for ρ as a function of T and x , then derive the adiabatic gradient directly from its definition (Equation 3.4), taking into account the fact that the mean molecular weight in the ideal gas law varies with x , hence the pressure will not only be a function of T and ρ but also of x (see Kippenhahn & Weigert 1990, Chapter 14.3 for a detailed derivation). The final expression for the adiabatic gradient during ionization is

$$\nabla_{\text{ad}} = \frac{2 + x(1-x)\Phi_H}{5 + x(1-x)\Phi_H^2}, \quad (\text{D.2})$$

with $\Phi_H \equiv \frac{5}{2} + \frac{\chi}{k_B T}$. The derivation of ∇_{ad} during dissociation is more involved mathematically (see, e.g., Vardya 1960) and leads to a slightly more complicated final expression,

$$\nabla_{\text{ad}} = \frac{1 + x + \frac{x(1-x^2)}{2} \frac{\chi}{k_B T}}{5x + \frac{7(1-x)}{2} + \frac{x(1-x^2)}{2} \left(\frac{\chi}{k_B T} \right)^2}. \quad (\text{D.3})$$

Using Equation (D.3), we recover $\nabla_{\text{ad}} = 2/7$ for $x = 0$ (no ongoing dissociation hence hydrogen is purely molecular and diatomic) and $\nabla_{\text{ad}} = 2/5$ for $x = 1$ (hydrogen is fully dissociated into atoms and hence monatomic). Figure D.1 shows the dependence of ∇_{ad} on the dissociation fraction, for $T = 3000 \text{ K}$, the temperature at which dissociation typically occurs (Langmuir 1912). The adiabatic gradient drops substantially during partial dissociation, since part of the internal energy is used in dissociation rather than in increasing the temperature of the system.

D.0.8 ADIABATIC GRADIENT DURING CONVERSION OF SPIN ISOMERS

The adiabatic gradient scales as $\nabla_{\text{ad}} \sim 1/c_V$. The translational component of the heat capacity, $c_{V,t} = 3\mathcal{R}/2$, is independent of temperature. As $c_{V,r}$ increases, ∇_{ad} declines. We can therefore understand how conversion between spin isomers affects ∇_{ad} by studying the dependence on tem-

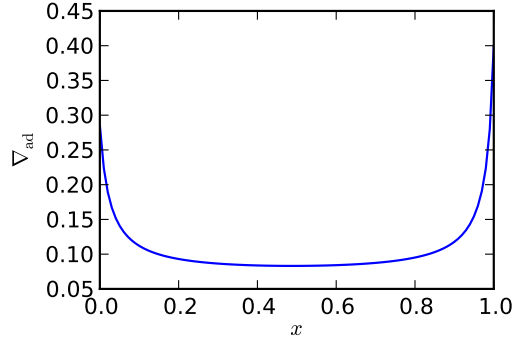


Figure D.1: Adiabatic gradient as a function of the hydrogen dissociation fraction x . The adiabatic gradient is $\nabla_{\text{ad}} = 2/7$ for pure molecular hydrogen ($x = 0$) and $\nabla_{\text{ad}} = 2/5$ for fully atomic hydrogen ($x = 1$), and drops to low values during partial dissociation.

perature of $c_{V,r}$ of the ortho-para mixture.

The internal energy per unit mass and specific heat capacity associated with rotation for the individual isomers, for the equilibrium mixture, and for a fixed ortho-para ratio of 3:1 can be derived from their partition functions (see Appendix C for details), and are plotted in Figure D.2 (after [Farkas 1935](#), Figure 1). At low temperatures, parahydrogen is in the $j = 0$ state and has no rotational energy, while orthohydrogen is in the $j = 1$ state and has the energy of its first rotational level. Both para- and orthohydrogen, as well as their equilibrium mixture, behave like monatomic gases at low temperatures and thus have zero rotational heat capacity. This is consistent with $\nabla_{\text{ad}} = 2/5$ at low temperatures as seen in Figure 3.1. As the temperature increases, the energetically higher-lying rotational states of para- and orthohydrogen are populated and the heat capacity of both spin isomers increases as a result. We note that the heat capacity of the equilibrium mixture is not a weighted average of the heat capacities of the individual components because it takes into account both the rotational energy uptake of para- and orthohydrogen, and also the shift in their equilibrium concentrations with temperature. This results in a peak in the heat capacity of the mixture around ~ 50 K, as seen in the bottom plot of Figure D.2. It follows that the adiabatic gradient has to reduce, reach a

minimum, then increase as the temperature rises, as shown in Figure 3.1. In contrast, the heat capacity for the 3:1 ortho-para ratio mixture will be a weighted average between the individual ortho- and para- components, and will hence have intermediate values between the two, as displayed in Figure D.2.

Figure D.3, bottom panel, shows that the atmospheric growth time may increase by a factor of ~ 3 if a fixed 3:1 ortho-para ratio is assumed instead of thermal equilibrium between the hydrogen spin isomers. This enhanced growth time increases M_{crit} .

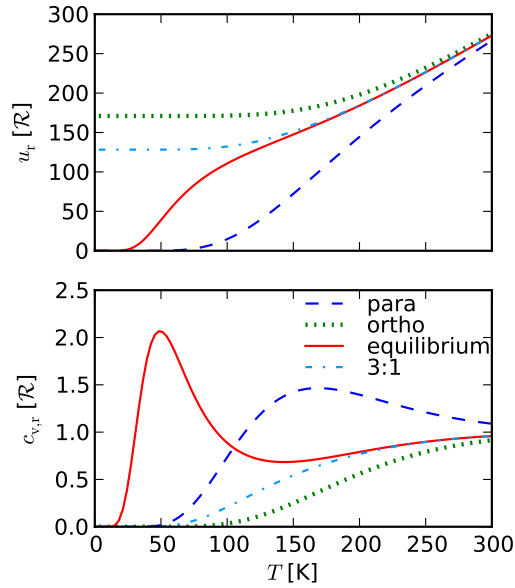


Figure D.2: Internal energy per unit mass and specific heat capacity associated with rotation for parahydrogen (dashed blue), orthohydrogen (dotted green), the equilibrium mixture (solid red) and a fixed 3:1 ortho-to-para ratio (dash-dotted light blue) as a function of temperature. After [Farkas \(1935\)](#), Figure 1.

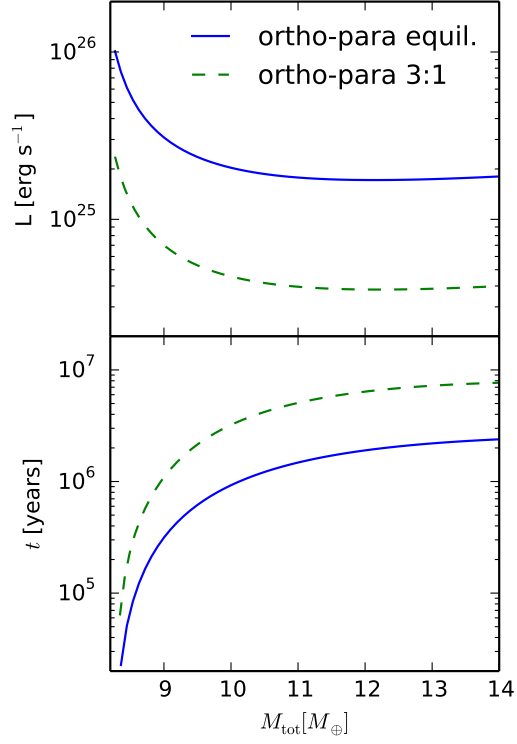


Figure D.3: Evolution of the luminosity and elapsed time during atmospheric growth around a $8M_{\oplus}$ core at 100 AU, for a realistic EOS with hydrogen spin isomers in thermal equilibrium (solid line), and with a fixed ortho-to-para ratio 3:1 (dashed line). The assumption of a fixed ortho-to-para ratio increases the runaway accretion time t_{run} by a factor of ~ 3 compared to the equilibrium mixture.

O

E

Grain growth opacity and radiative windows

The opacity of the interstellar medium is reasonably well constrained and approximate analytic expressions for the Rosseland mean opacity as a function of temperature and density are derived in [Bell & Lin \(1994\)](#). For low temperatures ($T \lesssim 100$ K) at which ice grains are present, opacity scales with temperature as $\kappa \sim T^2$. Sublimation of ice grains at ~ 150 K and of metal grains at ~ 1000 K results in sharp opacity drops. This is shown in Figure E.1 for a gas density $\rho = 10^{-8} \text{ g cm}^{-3}$, which is typical for the outer regions of protoplanetary disks. [Semenov et al. \(2003\)](#) calculate Rosseland mean opacities in protoplanetary disks for grains of different sizes and structure. As shown

in Figure E.1, their results are in good agreement with [Bell & Lin \(1994\)](#). However, [Semenov et al. \(2003\)](#) do not take grain growth into account, which is likely to occur in protoplanetary disks, particularly at the late times when cores form. [D'Alessio et al. \(2001\)](#) compute wavelength dependent opacities for a range of maximum particle sizes and different size distributions. Figure E.1 shows the integrated Rosseland mean opacity for a maximum particle size of 1 cm and a power law differential size distribution $dN/ds \propto s^{-p}$, with s the grain size and $p = 3.5$ for a standard collisional cascade and $p = 2.5$ when coagulation is taken into account. We see in Figure E.1 that this yields a mean opacity that is both lower and less sensitive to temperature, when compared to [Bell & Lin \(1994\)](#) or [Semenov et al. \(2003\)](#). However, [D'Alessio et al. \(2001\)](#) only computes opacities for temperatures less than the dust sublimation temperature, appropriate for current observations of dust in protoplanetary disks. As we see in Figure E.1, the opacity dramatically decreases during dust sublimation. We thus use the [Bell & Lin \(1994\)](#) opacities for $T \gtrsim 1000$ K, ensuring that they smoothly match the [D'Alessio et al. \(2001\)](#) opacities for lower temperatures.

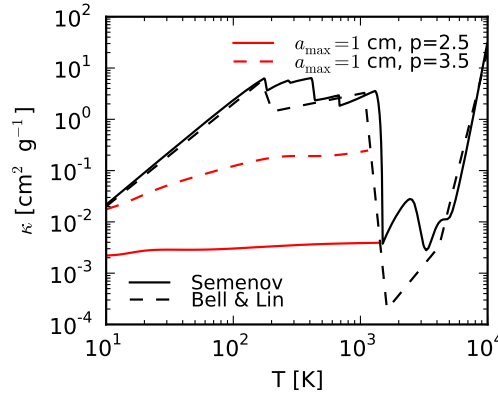


Figure E.1: Rosseland mean opacity of dust grains as a function of temperature for different opacity assumptions. The dashed black curve shows the [Bell & Lin \(1994\)](#) analytic ISM opacity for $\rho = 10^{-8} \text{ g cm}^{-3}$. The solid black curve shows the tabulated opacity of [Semenov et al. \(2003\)](#) for a dust composition of 'normal' silicates. The dashed red curve shows the [D'Alessio et al. \(2001\)](#) opacity, which takes grain growth into account, for a maximum particle size of 1 cm and a standard collisional cascade grain size distribution ($p = 3.5$). The solid red curve is the same as the dashed red curve, but it accounts for coagulation ($p = 2.5$).

The significant opacity drop due to the sublimation of ice and metal grains lowers the radiative temperature gradient ∇_{rad} , which may result in one or more inner radiative layers inside the atmosphere of a protoplanet. This is displayed in Figure E.2: depending on the semimajor axis and core mass, the opacity drop will generate no radiative window (top panel), one radiative window (middle panel), or two radiative windows (bottom panel).

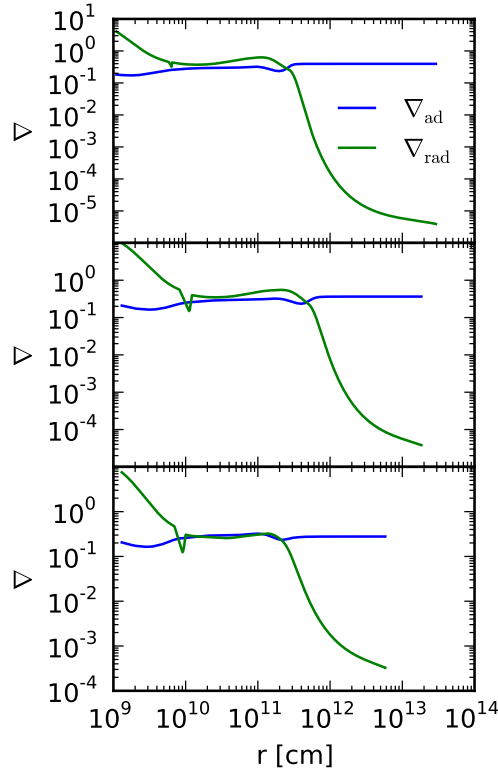


Figure E.2: Snapshots of the radiative and adiabatic gradient as a function of the radial coordinate, for planets with different core masses forming at various locations in the disk. The nebular gas is described by a realistic EOS, with a standard collisional cascade size distribution ($p = 3.5$). The sharp drop in opacity due to dust sublimation may generate one or more radiative windows. Top panel: no radiative window for $a = 100$ AU and $M_c = 3M_\oplus$. Middle panel: the sharp opacity decrease produces one radiative window for $a = 50$ AU and $M_c = 5M_\oplus$. Bottom panel: the decrease in opacity results in two radiative windows for $a = 20$ AU and $M_c = 3M_\oplus$.

Our idealization of a constant L with radius may be challenged by the presence of radiative win-

dows. While the structure of convective regions is unaffected by L , the structure of radiative winds depends on L . Fortunately, the assumption of constant luminosity remains reasonable if most of the luminosity is generated in the innermost convective region of the envelope. We can check whether this is true *a posteriori* by using the local energy equation,

$$\frac{\partial L}{\partial m} = -T \frac{\partial S}{\partial t}, \quad (\text{E.1})$$

and integrating it between M_c and M_{RCB_1} , where RCB_1 is the innermost RCB. This luminosity can be as little as half of the assumed fixed atmospheric luminosity L .

Self-consistently calculating $L(r)$ is not feasible for our code. Instead, we note that since $\partial S/\partial t$ is fixed in convective regions (Arras & Bildsten 2006), the luminosity profile is more centrally concentrated than $L \propto m$, which can be implemented simply. We calculated example profiles using $L \propto m$ and found that though this luminosity scaling may move the location of the outermost RCB, it does not substantially change the luminosity emerging at the top of the atmosphere or the time evolution.



Steady-state active disk solution

Following [Shakura & Sunyaev \(1973\)](#) and [Armitage \(2010\)](#), the steady-state solution for a geometrically thin, optically thick actively accreting disk with an α -prescription for viscosity is governed by the following set of equations:

$$\nu = \alpha c H \quad (\text{F.1a})$$

$$c^2 = \frac{k_B T_{\text{act}}}{\mu m_p} \quad (\text{F.1b})$$

$$\rho = \frac{1}{\sqrt{2\pi}} \frac{\Sigma}{H} \quad (\text{F.1c})$$

$$H = \frac{c}{\Omega_k} \quad (\text{F.1d})$$

$$T_{\text{act}}^4 = \frac{3}{4} \tau T_{\text{surf}}^4 \quad (\text{F.1e})$$

$$\tau = \frac{1}{2} \Sigma \kappa \quad (\text{F.1f})$$

$$\nu \Sigma = \frac{\dot{M}}{3\pi} \quad (\text{F.1g})$$

$$\sigma T_{\text{surf}}^4 = \frac{9}{8} \nu \Sigma \Omega_k^2 \quad (\text{F.1h})$$

$$\kappa = \kappa_0 T_{\text{act}}^2, \quad (\text{F.1i})$$

where T_{surf} is the surface temperature of the disk and the other quantities are defined in the main text. This is a system of nine equations with nine unknowns ($\nu, c, H, T_{\text{act}}, \rho, \Sigma, \tau, T_{\text{surf}}, \kappa$) that can be solved numerically once α and κ_0 are specified.



Desorption distance analytic solution

For a particle of size s that desorbs and satisfies $\tau_s \ll 1$ (τ_s is the dimensionless stopping time, defined in Section 4.2.2), we can derive an explicit analytic solution for the particle's desorption distance in an irradiated disk. For $\tau_s \ll 1$, a particle is in the Epstein drag regime (see Equation 4.9) and its drift velocity \dot{r} (Equation 4.10) can be approximated as

$$\dot{r} \approx -2\eta\Omega_k r \tau_s. \quad (\text{G.1})$$

By using Equations (4.15) and (4.16) and setting $t_{\text{drift}} = t_{\text{des}}$, we can express a particle's desorption distance as

$$r_{\text{des}} = \left(\frac{d}{qC} \mathcal{W} \left[\frac{(B/A)^{-q/d} q C}{d} \right] \right)^{\frac{1}{q}}, \quad (\text{G.2})$$

where \mathcal{W} is the Lambert-W function, $q = 3/7$ is the power-law coefficient in Equation (4.1b),

$d = -\frac{1}{2} + p - q$ with $p = 1$ the power-law coefficient in Equation (4.1a), and

$$A = \frac{\rho_0}{\rho_s} \frac{r_0^2}{sc_0} r_0^d \quad (\text{G.3a})$$

$$B = \frac{\rho_s s}{3\mu_x N_x \nu_x} \quad (\text{G.3b})$$

$$C = \frac{E_x}{T_0} r_0^{-q}, \quad (\text{G.3c})$$

$$(\text{G.3d})$$

where $r_0 = 1 \text{ AU}$, $\rho_0 = \rho(r_0)$ and $c_0 = c(r_0)$.

References

- Aikawa, Y., Miyama, S. M., Nakano, T., & Umebayashi, T. 1996, *ApJ*, 467, 684
- Ali-Dib, M., Mousis, O., Petit, J.-M., & Lunine, J. I. 2014, *ApJ*, 785, 125
- Alibert, Y., Mordasini, C., Benz, W., & Winisdoerffer, C. 2005, *A&A*, 434, 343
- Andrews, S. M., Rosenfeld, K. A., Kraus, A. L., & Wilner, D. J. 2013, *ApJ*, 771, 129
- Andrews, S. M., Wilner, D. J., Hughes, A. M., Qi, C., & Dullemond, C. P. 2010, *ApJ*, 723, 1241
- Armitage, P. J. 2010, *Astrophysics of Planet Formation* (Cambridge, UK: Cambridge University Press)
- Arras, P., & Bildsten, L. 2006, *ApJ*, 650, 394
- Ayliffe, B. A., & Bate, M. R. 2012, *MNRAS*, 427, 2597
- Bai, X.-N., & Goodman, J. 2009, *ApJ*, 701, 737
- Batalha, N. M. 2014, *Proceedings of the National Academy of Science*, 111, 12647
- Beckwith, S. V. W., & Sargent, A. I. 1991, *ApJ*, 381, 250
- Beckwith, S. V. W., Sargent, A. I., Chini, R. S., & Guesten, R. 1990, *AJ*, 99, 924
- Bell, C. P. M., Naylor, T., Mayne, N. J., Jeffries, R. D., & Littlefair, S. P. 2013, *MNRAS*, 434, 806
- Bell, K. R., & Lin, D. N. C. 1994, *ApJ*, 427, 987
- Bergin, E. A., Blake, G. A., Ciesla, F., Hirschmann, M. M., & Li, J. 2015, *Proceedings of the National Academy of Science*, 112, 8965
- Birnstiel, T., Dullemond, C. P., & Brauer, F. 2010, *A&A*, 513, A79
- Birnstiel, T., Klahr, H., & Ercolano, B. 2012, *A&A*, 539, A148

- Bisschop, S. E., Fraser, H. J., Öberg, K. I., van Dishoeck, E. F., & Schlemmer, S. 2006, *A&A*, 449, 1297
- Blanksby, S. J., & Ellison, G. B. 2003, *Acc. Chem. Res.*, 36, 255
- Bodenheimer, P., Grossman, A. S., Decamp, W. M., Marcy, G., & Pollack, J. B. 1980, *Icarus*, 41, 293
- Bodenheimer, P., & Pollack, J. B. 1986, *Icarus*, 67, 391
- Boley, A. C., Hartquist, T. W., Durisen, R. H., & Michael, S. 2007, *ApJl*, 656, L89
- Boogert, A. C. A., Gerakines, P. A., & Whittet, D. C. B. 2015, *ARA&A*, 53, 541
- Boss, A. P. 1997, *Science*, 276, 1836
- Bottinelli, S., Boogert, A. C. A., Bouwman, J., et al. 2010, *ApJ*, 718, 1100
- Bromley, B. C., & Kenyon, S. J. 2011, *ApJ*, 731, 101
- Burrows, A., Marley, M., Hubbard, W. B., et al. 1997, *ApJ*, 491, 856
- Cameron, A. G. W. 1978, *Moon and Planets*, 18, 5
- Chambers, J. E. 2009, *ApJ*, 705, 1206
- Chiang, E., & Youdin, A. N. 2010, *Annual Review of Earth and Planetary Sciences*, 38, 493
- Ciesla, F. J., & Cuzzi, J. N. 2006, *Icarus*, 181, 178
- Close, L. M., Follette, K. B., Males, J. R., et al. 2014, *ApJL*, 781, L30
- Collings, M. P., Anderson, M. A., Chen, R., et al. 2004, *MNRAS*, 354, 1133
- Collings, M. P., Dever, J. W., Fraser, H. J., & McCoustra, M. R. S. 2003, *ApJS*, 285, 633
- Conrath, B. J., & Gierasch, P. J. 1984, *Icarus*, 57, 184
- Cruikshank, D. P., Roush, T. L., Owen, T. C., et al. 1993, *Science*, 261, 742
- Cuzzi, J. N., & Zahnle, K. J. 2004, *ApJ*, 614, 490
- D'Alessio, P., Calvet, N., & Hartmann, L. 2001, *ApJ*, 553, 321

- D'Angelo, G., & Bodenheimer, P. 2013, *ApJ*, 778, 77
- D'Angelo, G., Durisen, R. H., & Lissauer, J. J. 2011, *Giant Planet Formation*, ed. S. Piper, 319–346
- Debes, J. H., Jang-Condell, H., Weinberger, A. J., Roberge, A., & Schneider, G. 2013, *ApJ*, 771, 45
- Dohnanyi, J. S. 1969, *J. Geophys. Res.*, 74, 2531
- Dones, L., & Tremaine, S. 1993, *Icarus*, 103, 67
- Du, F., Bergin, E. A., & Hogerheijde, M. R. 2015, *ArXiv e-prints*, arXiv:1506.03510
- Duncan, M. J., & Levison, H. F. 1997, *Science*, 276, 1670
- Espaillet, C., Ingleby, L., Hernández, J., et al. 2012, *ApJ*, 747, 103
- Farkas, A. 1935, *Orthohydrogen, Parahydrogen and Heavy Hydrogen*
- Fayolle, E. C., Balfe, J., Loomis, R., et al. 2016, *ApJl*, 816, L28
- Ferguson, J. W., Alexander, D. R., Allard, F., et al. 2005, *ApJ*, 623, 585
- Fortney, J. J., Marley, M. S., & Barnes, J. W. 2007, *ApJ*, 659, 1661
- Fouchet, T., Lellouch, E., & Feuchtgruber, H. 2003, *Icarus*, 161, 127
- Frank, J., King, A., & Raine, D. J. 2002, *Accretion Power in Astrophysics: Third Edition*
- Fraser, H. J., Collings, M. P., McCoustra, M. R. S., & Williams, D. A. 2001, *MNRAS*, 327, 1165
- Fukutani, K., & Sugimoto, T. 2013, *Progress In Surface Science*, 88, 279
- Garaud, P., & Lin, D. N. C. 2007, *ApJ*, 654, 606
- Garrod, R. T., & Herbst, E. 2006, *A&A*, 457, 927
- Garrod, R. T., & Pauly, T. 2011, *ApJ*, 735, 15
- Glassgold, A. E., Najita, J., & Igea, J. 1997, *ApJ*, 480, 344
- Goldreich, P., Lithwick, Y., & Sari, R. 2004, *ARA&A*, 42, 549
- Graboske, H. C., Harwood, D. J., & Rogers, F. J. 1969, *Physical Review*, 186, 210

- Greene, T. P., Line, M. R., Montero, C., et al. 2016, *ApJ*, 817, 17
- Hartmann, L., Calvet, N., Gullbring, E., & D'Alessio, P. 1998, *ApJ*, 495, 385
- Hayashi, C. 1981, *Progress of Theoretical Physics Supplement*, 70, 35
- Henning, T., & Semenov, D. 2013, *Chemical Reviews*, 113, 9016
- Hinz, P., Arbo, P., Bailey, V., et al. 2012, in *SPIE*, Vol. 8445, *Optical and Infrared Interferometry III*, 84450U
- Hollenbach, D., Kaufman, M. J., Bergin, E. A., & Melnick, G. J. 2009, *ApJ*, 690, 1497
- Hori, Y., & Ikoma, M. 2010, *ApJ*, 714, 1343
- . 2011, *MNRAS*, 416, 1419
- Hubickyj, O., Bodenheimer, P., & Lissauer, J. J. 2005, *Icarus*, 179, 415
- Huestis, D. L. 2008, *Planet. Space Sci.*, 56, 1733
- Hughes, A. L. H., & Armitage, P. J. 2010, *ApJ*, 719, 1633
- Ida, S., Lin, D. N. C., & Nagasawa, M. 2013, *ApJ*, 775, 42
- Ikoma, M., Nakazawa, K., & Emori, H. 2000, *ApJ*, 537, 1013
- Ilgner, M., Henning, T., Markwick, A. J., & Millar, T. J. 2004, *A&A*, 415, 643
- Inutsuka, S.-i. 2012, *Progress of Theoretical and Experimental Physics*, 2012, 010000
- Jayawardhana, R., Hartmann, L., Fazio, G., et al. 1999, *ApJL*, 521, L129
- Kennedy, G. M., Kenyon, S. J., & Bromley, B. C. 2006, *ApJL*, 650, L139
- Kenyon, S. J., & Bromley, B. C. 2009, *ApJL*, 690, L140
- Kippenhahn, R., & Weigert, A. 1990, *Stellar Structure and Evolution*
- Kittel, C., Kroemer, H., & Landsberg, P. T. 1981, *Nature*, 289, 729
- Kratter, K. M., Murray-Clay, R. A., & Youdin, A. N. 2010, *ApJ*, 710, 1375
- Kraus, A. L., Ireland, M. J., Martinache, F., & Hillenbrand, L. A. 2011, *ApJ*, 731, 8

- Kreidberg, L., Line, M. R., Bean, J. L., et al. 2015, ArXiv e-prints, arXiv:1504.05586
- Krijt, S., Ormel, C. W., Dominik, C., & Tielens, A. G. G. M. 2015, *A&A*, 574, A83
- Lagrange, A.-M., Bonnefoy, M., Chauvin, G., et al. 2010, *Science*, 329, 57
- Lambrechts, M., & Johansen, A. 2012, *A&A*, 544, A32
- Langmuir, I. 1912, *J. Am. Chem. Soc.*, 34, 860
- Larson, R. B. 1969, *MNRAS*, 145, 271
- Lique, F., Honvault, P., & Faure, A. 2012, *J. Chem. Phys.*, 137, 154303
- . 2014, ArXiv e-prints, arXiv:1402.5292
- Lissauer, J. J., Dawson, R. I., & Tremaine, S. 2014, *Nature*, 513, 336
- Lissauer, J. J., Hubickyj, O., D’Angelo, G., & Bodenheimer, P. 2009, *Icarus*, 199, 338
- Lodders, K. 2003, *ApJ*, 591, 1220
- . 2009, ArXiv e-prints, arXiv:0910.0811
- Macintosh, B. A., Anthony, A., Atwood, J., et al. 2012, in *SPIE*, Vol. 8446, Ground-based and Airborne Instrumentation for Astronomy IV, 84461U
- Madhusudhan, N., Amin, M. A., & Kennedy, G. M. 2014, *ApJl*, 794, L12
- Madhusudhan, N., Harrington, J., Stevenson, K. B., et al. 2011, *Nature*, 469, 64
- Mandell, A. M., Bast, J., van Dishoeck, E. F., et al. 2012, *ApJ*, 747, 92
- Mandl, F. 1989, *Statistical Physics*, 2nd Edition
- Marleau, G.-D., & Cumming, A. 2014, *MNRAS*, 437, 1378
- Marois, C., Macintosh, B., Barman, T., et al. 2008, *Science*, 322, 1348
- Martin, R. G., & Livio, M. 2012, *MNRAS*, 425, L6
- Martín-Doménech, R., Muñoz Caro, G. M., Bueno, J., & Goesmann, F. 2014, *A&A*, 564, A8
- Mathews, G. S., Klaassen, P. D., Juhász, A., et al. 2013, *A&A*, 557, A132

- Matzner, C. D., & Levin, Y. 2005, *ApJ*, 628, 817
- Menou, K., & Goodman, J. 2004, *ApJ*, 606, 520
- Milenko, Y. Y., Sibileva, R. M., & Strzhemechny, M. A. 1997, *Journal of Low Temperature Physics*, 107, 77
- Militzer, B., & Hubbard, W. B. 2013, *ApJ*, 774, 148
- Min, M., Dullemond, C. P., Kama, M., & Dominik, C. 2011, *Icarus*, 212, 416
- Mizuno, H., Nakazawa, K., & Hayashi, C. 1978, *Progress of Theoretical Physics*, 60, 699
- Mollière, P., van Boekel, R., Dullemond, C., Henning, T., & Mordasini, C. 2015, *ApJ*, 813, 47
- Mordasini, C. 2014, *A&A*, 572, A118
- Mordasini, C., Alibert, Y., Klahr, H., & Henning, T. 2012, *A&A*, 547, A111
- Mordasini, C., Klahr, H., Alibert, Y., Miller, N., & Henning, T. 2014, *A&A*, 566, A141
- Mousis, O., Fletcher, L. N., Lebreton, J.-P., et al. 2014, *P&SS*, 104, 29
- Movshovitz, N., Bodenheimer, P., Podolak, M., & Lissauer, J. J. 2010, *Icarus*, 209, 616
- Mulders, G. D., Ciesla, F. J., Min, M., & Pascucci, I. 2015, *ApJ*, 807, 9
- Mumma, M. J., & Charnley, S. B. 2011, *ARA&A*, 49, 471
- Nettelmann, N., Becker, A., Holst, B., & Redmer, R. 2012, *ApJ*, 750, 52
- Nettelmann, N., Holst, B., Kietzmann, A., et al. 2008, *ApJ*, 683, 1217
- Öberg, K. I., Boogert, A. C. A., Pontoppidan, K. M., et al. 2008, *ApJ*, 678, 1032
- . 2011a, *ApJ*, 740, 109
- Öberg, K. I., Murray-Clay, R., & Bergin, E. A. 2011b, *ApJL*, 743, L16
- Öberg, K. I., van Broekhuizen, F., Fraser, H. J., et al. 2005, *ApJL*, 621, L33
- Okuzumi, S., Tanaka, H., Kobayashi, H., & Wada, K. 2012, *ApJ*, 752, 106
- Ormel, C. W. 2013, *MNRAS*, 428, 3526

- . 2014, *ApJl*, 789, L18
- Ormel, C. W., & Klahr, H. H. 2010, *A&A*, 520, A43
- Owen, J. E. 2014, *ApJl*, 790, L7
- Owen, T., Mahaffy, P. R., Niemann, H. B., Atreya, S., & Wong, M. 2001, *ApJl*, 553, L77
- Owen, T. C., Roush, T. L., Cruikshank, D. P., et al. 1993, *Science*, 261, 745
- Pachucki, K., & Komasa, J. 2008, *Phys. Rev. A*, 77, 030501
- Pagani, L., Bourgoïn, A., & Lique, F. 2012, *A&A*, 548, L4
- Papaloizou, J. C. B., & Nelson, R. P. 2005, *A&A*, 433, 247
- Papaloizou, J. C. B., & Terquem, C. 1999, *ApJ*, 521, 823
- Paxton, B., Bildsten, L., Dotter, A., et al. 2011, *ApJS*, 192, 3
- Paxton, B., Cantiello, M., Arras, P., et al. 2013, *ApJS*, 208, 4
- Pérez, L. M., Carpenter, J. M., Chandler, C. J., et al. 2012, *ApJl*, 760, L17
- Perez-Becker, D., & Chiang, E. 2011, *ApJ*, 727, 2
- Perri, F., & Cameron, A. G. W. 1974, *Icarus*, 22, 416
- Piso, A.-M. A., Öberg, K. I., Birnstiel, T., & Murray-Clay, R. A. 2015, *ApJ*, 815, 109
- Piso, A.-M. A., & Youdin, A. N. 2014, *ApJ*, 786, 21
- Podolak, M. 2003, *Icarus*, 165, 428
- Podolak, M., & Zucker, S. 2004, *Meteoritics and Planetary Science*, 39, 1859
- Pollack, J. B., Hubickyj, O., Bodenheimer, P., et al. 1996, *Icarus*, 124, 62
- Pollack, J. B., McKay, C. P., & Christofferson, B. M. 1985, *Icarus*, 64, 471
- Pontoppidan, K. M., Salyk, C., Bergin, E. A., et al. 2014, *Protostars and Planets VI*, 363
- Pontoppidan, K. M., Fraser, H. J., Dartois, E., et al. 2003, *A&A*, 408, 981

- Qi, C., Öberg, K. I., Andrews, S. M., et al. 2015, *ApJ*, 813, 128
- Qi, C., Öberg, K. I., Wilner, D. J., et al. 2013, *Science*, 341, 630
- Rafikov, R. R. 2005, *ApJl*, 621, L69
- . 2006, *ApJ*, 648, 666
- . 2011, *ApJ*, 727, 86
- Ricci, L., Testi, L., Natta, A., & Brooks, K. J. 2010, *A&A*, 521, A66
- Rodgers, S. D., & Charnley, S. B. 2002, *MNRAS*, 330, 660
- Rubin, M., Altwegg, K., Balsiger, H., et al. 2015, *Science*, 348, 232
- Saumon, D., Chabrier, G., & van Horn, H. M. 1995, *ApJS*, 99, 713
- Semenov, D., Henning, T., Helling, C., Ilgner, M., & Sedlmayr, E. 2003, *A&A*, 410, 611
- Semenov, D., & Wiebe, D. 2011, *ApJS*, 196, 25
- Shakura, N. I., & Sunyaev, R. A. 1973, *A&A*, 24, 337
- Sicilia-Aguilar, A., Henning, T., & Hartmann, L. W. 2010, *ApJ*, 710, 597
- Stevenson, D. J. 1982, *P&SS*, 30, 755
- Stevenson, K. B., Bean, J. L., Seifahrt, A., et al. 2014, *AJ*, 147, 161
- Takahashi, J. 2001, *ApJ*, 561, 254
- Thiabaud, A., Marboeuf, U., Alibert, Y., Leya, I., & Mezger, K. 2015, *A&A*, 574, A138
- Thompson, M. J. 2006, *An introduction to astrophysical fluid dynamics*
- Turner, N. J., Carballido, A., & Sano, T. 2010, *ApJ*, 708, 188
- van der Marel, N., van Dishoeck, E. F., Bruderer, S., Pérez, L., & Isella, A. 2015, *A&A*, 579, A106
- van Dishoeck, E. F. 2006, *Proceedings of the National Academy of Science*, 103, 12249
- Vardya, M. S. 1960, *ApJS*, 4, 281

- Visser, R., van Dishoeck, E. F., Doty, S. D., & Dullemond, C. P. 2009, *A&A*, 495, 881
- Walmsley, C. M., Flower, D. R., & Pineau des Forêts, G. 2004, *A&A*, 418, 1035
- Weidenschilling, S. J. 1977, *MNRAS*, 180, 57
- Williams, J. P., & Cieza, L. A. 2011, *ARA&A*, 49, 67
- Wilner, D. J., Ho, P. T. P., Kastner, J. H., & Rodríguez, L. F. 2000, *ApJl*, 534, L101
- Wuchterl, G. 1993, *Icarus*, 106, 323
- Wyckoff, S., Tegler, S. C., & Engel, L. 1991, *ApJ*, 367, 641
- Youdin, A. N., & Kenyon, S. J. 2013, *From Disks to Planets*, ed. T. D. Oswalt, L. M. French, & P. Kalas, 1
- Youdin, A. N., & Lithwick, Y. 2007, *Icarus*, 192, 588
- Youdin, A. N., & Mitchell, J. L. 2010, *ApJ*, 721, 1113
- Zhang, K., Pontoppidan, K. M., Salyk, C., & Blake, G. A. 2013, *ApJ*, 766, 82
- Zhu, Z., Stone, J. M., & Rafikov, R. R. 2013, *ApJ*, 768, 143
- Zsom, A., Ormel, C. W., Güttler, C., Blum, J., & Dullemond, C. P. 2010, *A&A*, 513, A57



THIS THESIS WAS TYPESET using \LaTeX , originally developed by Leslie Lamport and based on Donald Knuth's \TeX . The body text is set in 11 point Egenolff-Berner Garamond, a revival of Claude Garamont's humanist typeface. The above illustration, *Science Experiment 02*, was created by Ben Schlitter and released under [CC BY-NC-ND 3.0](#). A template that can be used to format a PhD dissertation with this look & feel has been released under the permissive AGPL license, and can be found online at github.com/asm-products/Dissertate or from its lead author, Jordan Suchow, at suchow@post.harvard.edu.